

# Technical Report

## TR-14-21

### **Long-term safety of a planned geological repository for spent nuclear fuel in Forsmark – estimate of maximum ice sheet thicknesses**

Florence Colleoni, Claudia Wekerle, Centro Euro-Mediterraneo sui i Cambiamenti Climatici (cmcc), Bologna

Simona Masina, Centro Euro-Mediterraneo sui i Cambiamenti Climatici and Istituto Nazionale di Geofisica e Vulcanologia, Sezione di Bologna

September 2014

**Svensk Kärnbränslehantering AB**

Swedish Nuclear Fuel  
and Waste Management Co

Box 250, SE-101 24 Stockholm  
Phone +46 8 459 84 00



ISSN 1404-0344

SKB TR-14-21

ID 1439743

Updated 2016-09

# **Long-term safety of a planned geological repository for spent nuclear fuel in Forsmark – estimate of maximum ice sheet thicknesses**

Florence Colleoni, Claudia Wekerle, Centro Euro-Mediterraneo sui i Cambiamenti Climatici (cmcc), Bologna

Simona Masina, Centro Euro-Mediterraneo sui i Cambiamenti Climatici and Istituto Nazionale di Geofisica e Vulcanologia, Sezione di Bologna

September 2014

This report concerns a study which was conducted for SKB. The conclusions and viewpoints presented in the report are those of the authors. SKB may draw modified conclusions, based on additional literature sources and/or expert opinions.

A pdf version of this document can be downloaded from [www.skb.se](http://www.skb.se).

**Update notice**

The original report, dated September 2014, was found to contain factual errors which have been corrected in this updated version. The corrected factual errors are presented below.

**Updated 2016-09**

<b>Location</b>	<b>Original text</b>	<b>Corrected text</b>
Page 3	Short summary of activities	New Preface inserted
Page 4	Short summary of activities	Short summary of activities

**Updated 2016-04**

<b>Location</b>	<b>Original text</b>	<b>Corrected text</b>
Page 11, Table 1-2	Wrong data in table and error in table header	Table updated with correct data and text in table header

# Preface

The following report constitute a first phase of a study reconstructing the Eurasian ice sheet during the peak Saalian glaciation, 140 000 years ago, by climate- and ice sheet model simulations. The study was initiated and managed by Prof. Jens-Ove Näslund (SKB) and Dr. Florence Colleoni (Centro Euro-Mediterraneo sui Cambiamenti Climatici, CMCC). The project steering group consisted of Dr. Florence Colleoni (CMCC), Dr. Claudia Wekerle (CMCC), Prof. Jens-Ove Näslund (SKB), Assoc. Prof. Jenny Brandefelt (SKB), Dr. Anne Kontula (Posiva), Dr. Lasse Koskinen (Posiva), and Dr. Simona Masina (CMCC).

The results will be used, together with the results of a second phase of the study and with other published scientific information, for constructing future scenarios with large ice sheet configurations for assessing the long-term safety of the planned repository for spent nuclear fuel in Forsmark, Sweden.

The report manuscript was reviewed by Assoc. prof. Nina Kirchner (Stockholm univ.), Dr. Mike Thorne (Mike Thorne and Associates Ltd.), Dr. Patrick Applegate (Pennsylvania State University), and Dr. Allan Hedin (SKB).

Stockholm, September 2014

*Jens-Ove Näslund*

Research coordinator Climate Programme SKB

## Short summary of activities

This report presents results of a study devoted to extend the current knowledge of ice-sheet thicknesses in Fennoscandia during a period of extensive glaciation. Specifically, a range of ice-sheet thicknesses in the Forsmark region in Sweden, where a geological repository for spent nuclear fuel is planned, was determined. To this end, the Late Saalian glaciation (~192–135 thousand years before present, kyrs BP), which is known to be the most extensive glaciation that occurred during the last 400 kyrs over Eurasia based on dated marginal positions, was analysed. During the peak of this glaciation, the area of the Eurasian ice sheet was at least twice as large as during the Last Glacial Maximum (~21 kyrs BP, LGM). The extent and thickness of the Eurasian ice sheet was determined in two steps. First, a coupled Atmosphere-Ocean-Sea-Ice-Land model was set up and integrated with constant-in-time forcing conditions (orbital parameters and greenhouse gas concentrations) and boundary conditions (topography and land surface conditions) representing the Late Saalian glacial maximum, ~140 kyrs BP. Secondly, the simulated climate was used as boundary condition for simulations with an ice-sheet model. In the coupled climate model simulations, assumptions on the extent and thickness of ice-sheets were made. The extent and thickness of the North American ice sheet during the Late Saalian glacial maximum is uncertain. In order to investigate the sensitivity of the simulated Eurasian climate to the extent and thickness of the North American ice-sheet, a set of two simulations were performed. In both simulations, the Eurasian ice-sheet was prescribed based on a previous ice-sheet model simulation for the Late Saalian glacial maximum. The North American (Laurentide) ice-sheet was prescribed with a large extent and thickness in the first experiment (Topo1, ~4,000 m high) and a smaller extent and thickness in the second experiment (B140\_Topo2, ~1,500 to 2,000 meters high).

The results show that the climate model performance compared to marine proxies is good in general except in the tropics, where the simulated climate is warmer than what the proxies suggest. The presence of the elevated ice sheets over North America and Eurasia induces a large cooling of about 30°C over the Northern high latitudes. Topo2, the simulation with the smaller Laurentide ice sheet, yields about 4°C higher temperatures over the Eurasian ice sheet compared to B140\_Topo1. The major contributor to this difference in climate is differences in synoptic circulation. Changes in stationary waves due to the orographic effect of the smaller Laurentide ice sheet in B140\_Topo2 induce a stronger cyclogenesis over North America, which intensifies the mean flow over the mid-latitudes, resulting in increased storm track activity over the North Atlantic. This affects the precipitation pattern at high latitudes causing higher precipitation rates over North America and over the Eurasian ice sheet when using B140\_Topo2. Furthermore, due to the impact of the smaller Laurentide ice sheet on stationary waves, a well-developed perennial snow cover accumulates over Eastern Siberia and Alaska. Interestingly, a recent data campaign suggested that an ice cap of ~1,000 m thick developed in this area during the Late Saalian.

The ice-sheet model simulations were performed with constant-in-time forcing and boundary conditions and the model was integrated until a steady state was reached. For each of the two simulated Late Saalian climates (Topo1 and Topo2), a set of univariate sensitivity tests were performed on two different horizontal grids, i.e. Northern Hemisphere (37°N–90°N) at 40 km and Eurasia at 20 km. For each of the grids, one reference simulation and 34 univariate sensitivity tests were carried out. In total, 140 univariate simulations were performed on each grid, including the reference experiments. Physical parameters in the ice-sheet model formulation related to the following five categories were investigated: i) climate downscaling, ii) surface mass balance, iii) basal drag, iv) ice shelves and v) the solid Earth. In general, the results show that the ice-sheet model is able to simulate a Late Saalian Eurasian ice sheet within the geographical limits indicated by the Svendsen et al. (2004) reconstruction. The difference in Eurasian ice-sheet volume resulting from the use of Topo1 and Topo2 simulated climate is modest (about 2 meters Sea Level Equivalents, m SLE), mostly due to geographical compensation between surface air temperature and precipitation differences. The largest ice-sheet sensitivity is simulated for the surface mass balance parameter and basal drag parameter categories. The basal drag parameters provide the upper and lower bound in simulated ice-sheet thickness over Forsmark of the complete set of experiments, with up to 7% increase with large basal drag and 7% decrease with larger fast flow areas relative to the reference simulations. In the complete set of sensitivity experiments, ice-sheet thickness in the Forsmark region ranges from 2,991 (2,650) meters to 3,472 (3,195) meters when using Topo1 (Topo2) climate forcing. The corresponding bedrock depression increases from 707 (632) meters to 822 (760) meters using Topo1 (Topo2) climate forcing.

Finally, an investigation of the sensitivity of the simulated ice-sheet thickness to simultaneous changes in more than one parameter was performed. Six multi-variate experiments, selected on basis of typical settings used in ice-sheet modelling, were performed for each grid. The resulting ice-sheet thicknesses over Forsmark in these six experiments fall within the range of the complete set of univariate sensitivity tests.

# Contents

<b>1</b>	<b>Introduction</b>	7
<b>2</b>	<b>Overall methods</b>	13
<b>3</b>	<b>Climate simulations</b>	15
3.1	Climate model and settings of the simulations	15
3.2	Comparison between simulated and marine SST records	18
3.3	Climate analysis	18
<b>4</b>	<b>Ice sheet simulations</b>	27
4.1	The GRISLI ice-sheet model	27
4.1.1	Definition of ice flow in GRISLI	27
4.1.2	Fundamental equations	27
4.1.3	Equation of motion: grounded ice	29
4.1.4	Equation of motion: fast flowing areas	30
4.1.5	Basal hydrology	31
4.1.6	Ice temperature	32
4.1.7	Surface mass balance	33
4.1.8	Isostasy	34
4.2	Model setup	35
4.2.1	Horizontal Grid	35
4.2.2	Initial conditions and climate forcing	35
4.3	Reference simulations	37
4.4	Sensitivity experiments: impact of model parameters	43
4.4.1	Results: overview	45
4.4.2	Climate correction	45
4.4.3	Positive Degree Day semi-empirical model	50
4.4.4	Ice streams	52
4.4.5	Ice shelves	54
4.4.6	Solid Earth	55
4.5	Sensitivity experiments: preliminary multi-parameters simulations	57
4.6	Sensitivity experiments: impact of horizontal grid resolution	62
<b>5</b>	<b>Discussion</b>	65
5.1	Laurentide and Eurasian ice sheet extents	65
5.2	Vegetation distribution	66
5.3	Initialization of ice-sheet simulations and assumption of steady-state simulations	67
5.4	Atmospheric lapse rates	69
5.5	Surface mass balance	69
5.6	Isostasy	71
<b>6</b>	<b>Conclusions</b>	73
<b>7</b>	<b>Outlook from the project</b>	75
	<b>References</b>	77
<b>Appendix 1</b>	Compilation of SST proxies	85
<b>Appendix 2</b>	Notation	87
<b>Appendix 3</b>	Sensitivity experiments using B140_Topo2 climate forcing	89

# 1 Introduction

The Swedish Nuclear Fuel and Waste Management Co., SKB, is planning to build a geological repository for spent nuclear fuel in Forsmark in south-central Sweden. The repository performance is dependent on numerous factors such as for instance isostatic pressure, the risk of ground freezing at repository depth, and intrusion of glacial meltwater – factors that are controlled by the presence of large ice sheets and permafrost. The aim of the present project is to provide data for an analysis of the impact on a repository at the Forsmark site of a theoretical future glaciation that would correspond to the most extensive known glaciation that has occurred over Eurasia, namely the Late Saalian glaciation ~140 kyrs BP (Marine Isotope Stage 6, MIS 6), by means of climate and ice-sheet numerical simulations. Performing parameter-perturbed ensemble ice sheet simulations will allow us to estimate the upper and lower bound of possible ice thicknesses over the Forsmark site associated with the Late Saalian glaciation.

Between ~3.3 million years ago (Myrs) and ~2.7 Myrs (which marks the Plio-Pleistocene transition), Ice-Rafted Debris records (IRD) show that large ice sheets started to grow over the Northern Hemisphere high latitudes (Haug et al. 2005). The analysis of the benthic  $\delta^{18}\text{O}$  marine records reveals that the frequency of the glacial/interglacial cycles changes from 41 kyrs to 100 kyrs during the Mid-Pleistocene Transition (MPT, ~1.1–0.8 Myrs, Lisiecki and Raymo 2007). In addition, the amplitude of the cycles after this transition is much larger than for the previous cycles. The reasons for both the Plio-Pleistocene transition and the MPT are still largely debated by the paleoclimate community. Various types of proxies indicate that the first transition is characterized by major global climate change, whereas for the MPT this seems not to be the case.

After the MPT, the benthic  $\delta^{18}\text{O}$  marine records show more extreme glacial cycles, implying that sea-level drop during glaciations could have been increased over the last million years (Figure 1-1). Recently, a more detailed analysis of  $\text{CO}_2$ , Antarctic air temperature and benthic  $\delta^{18}\text{O}$  marine records shows that the intensity of interglacials increased abruptly after ~430 kyrs BP, the so-called “Mid-Bruhnes Event” (Figure 1-1, Jansen et al. 1986, Tzedakis et al. 2009; MBE hereafter). Pre-MBE interglacials are characterized by low sea level (below that of the present-day), probably large Northern Hemisphere ice sheets (Helmke et al. 2003), particularly low  $\text{CO}_2$  concentrations (Lüthi et al. 2008) and no high peak of  $\text{CO}_2$  concentration at the interglacial maximum (Tzedakis et al. 2009). In particular, whereas the pre-MBE atmospheric  $\text{CO}_2$  concentration drops below 240 ppmv for the entire duration of pre-MBE interglacials, the  $\text{CO}_2$  concentration does not drop below 260 ppmv for post-MBE interglacials (Figure 1-1). Although this transition seems to affect interglacials exclusively, the impact of those two distinct types of interglacials on the subsequent glaciations might not be negligible.

Fluctuations of global ice volume can be estimated through the reconstructions of past global sea-level variations, i.e. glacio-eustatic sea-level variations. Those reconstructions are derived from different types of proxies such as corals and marine foraminifera. As a consequence, the estimated amplitude of past eustatic sea-level variations may vary from one source to another. Another non-negligible problem is the dating and tuning of the reconstructions. Most sea-level reconstructions are associated with different timescales, resulting from the method used to date the samples. To compare them, the time scales need to be synchronized. A good example of the variety of sea-level reconstructions is summarized in Rabineau et al. (2006) in relation to the last three glacial cycles (Figure 1-2). The amplitude of each glacial and interglacial oscillation is very different. Note that a change in sea-level drop of about 7 meters represents the equivalent of the total current Greenland ice volume and a drop of about 15 to 20 meters represents the whole Last Glacial Maximum Eurasian ice volume (LGM, ~21 kyrs BP, Peltier, 2004). The uncertainty associated with eustatic reconstructions is therefore non negligible, even at glaciation scale. For example, the sea-level drop corresponding to the LGM ranges from ~110 to ~140 meters below present-day sea level. The effects on ice volume that this difference implies are considerable.

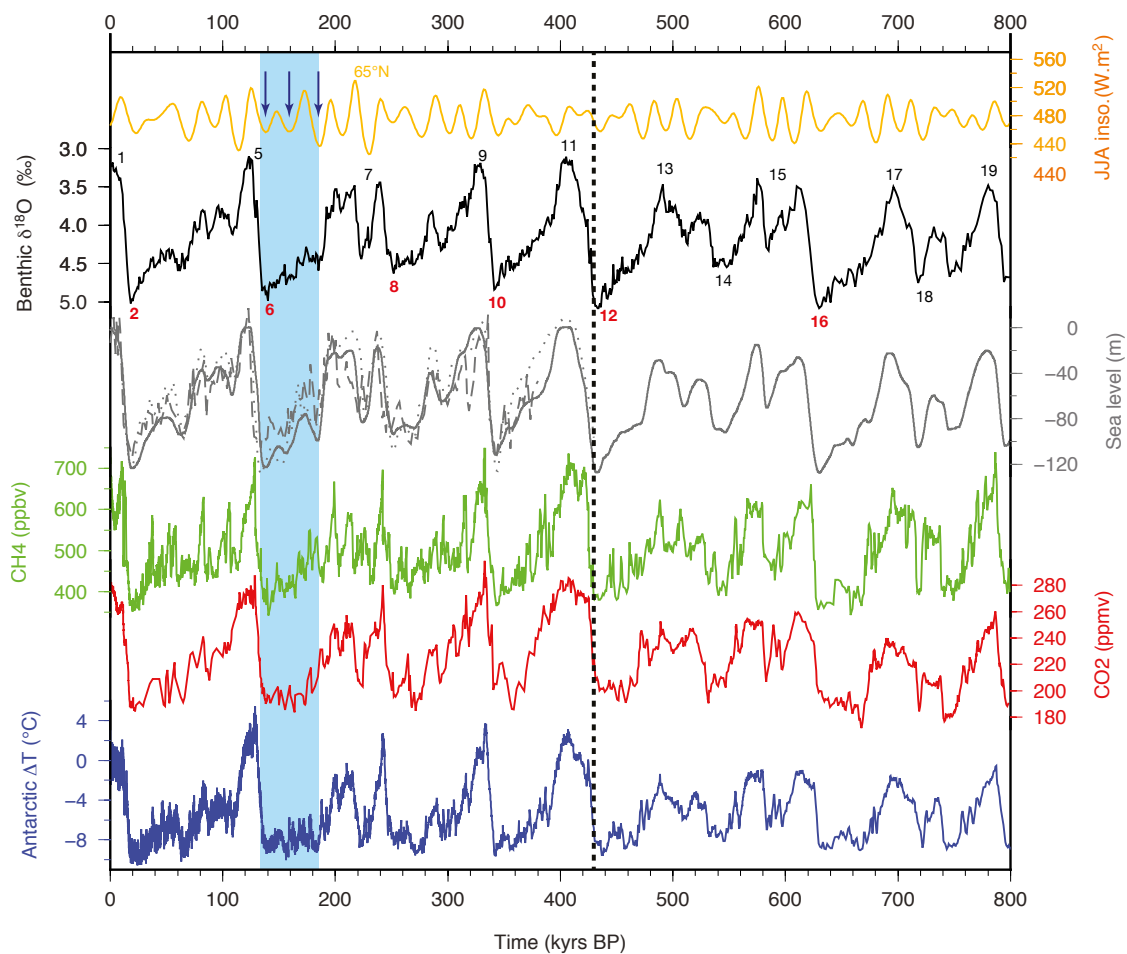


**Figure 1-1.** Global climate context of the last eight glacial cycles. From top to bottom: summer insolation at 65°N (Berger 1978) ( $W\cdot m^{-2}$ ). The three blue arrows indicate the three major advances of the Late Saalian Eurasian ice sheet identified by Svendsen et al. (2004); benthic  $\delta^{18}O$  stack from Lisiecki and Raymo (2005). Numbers indicate the Marine Isotope Stages (MIS) after Martinson et al. (1987). The MIS highlighted in red correspond to the glaciations during which the western extent of the Eurasian ice sheet was particularly large (Toucanne et al. 2010); sea-level reconstructions (m) from Waelbroeck et al. (2002) (dotted), Siddall et al. (2006) (dashed), Bintanja et al. (2005) (plain); atmospheric  $CH_4$  (ppbv) (Loulergue et al. 2008); atmospheric  $CO_2$  (ppmv) concentration from EPICA Dome C, East Antarctica (Lüthi et al. 2008); EPICA Dome C, East Antarctica, temperature anomaly ( $^{\circ}C$ ) relatively to present-day (Jouzel et al. 2007). The vertical dashed black line corresponds to the Mid-Bruhnes Event (Jansen et al. 1986). Vertical blue box highlights the Late Saalian glacial period.

Because of the lack of direct proxies, global sea-level reconstructions rarely trace back before the last four glacial cycles (Figure 1-1). The problem becomes even more complicated when the ice volume for individual ice sheets, i.e. the Laurentide, Eurasian and Antarctica ice sheets has to be reconstructed. The oldest reconstruction of the Northern Hemisphere ice-sheet extent for the LGM is the one from Hughes et al. (1977). Their reconstruction is by far more extensive over Eurasia than the more recent one by Svendsen et al. (2004). Their reconstruction corresponds in reality to the maximum extent of the Late Pleistocene glaciations that have been attributed to the LGM over North America and to the Late Saalian over Eurasia. Based on the available extent of reconstructions, the distribution of ice volume over the various ice sheets is estimated from a combination of modeling, using Earth models for glacio-isostasy, ice-sheet models and climate models, and paleo-data such as isotope ratios and paleo-beach elevations. One of the most well known reconstructions of ice distribution over North America, Eurasia and Antarctica for the last glacial cycle is the ICE-XG series (Table 1-1, see references therein). Other ice distributions have been developed over the last decades such as ANU05 (Fleming and Lambeck 2004) and IJ05 for Antarctica (Ivins and James 2005). Recently, a new pre-LGM Northern Hemisphere ice-sheet distribution has been proposed by Kleman et al. (2013).

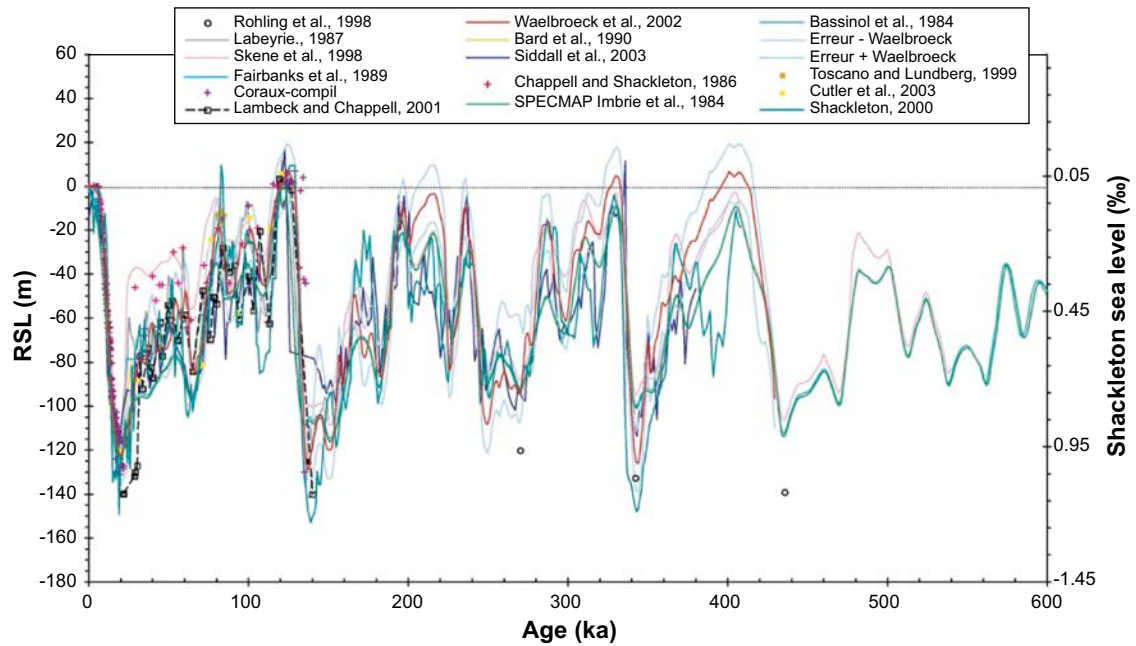


**Figure 1-2.** Compilation of various sea-level reconstructions from Rabineau et al. (2006). For references mentioned in the figure, see Rabineau et al. (2006).

**Table 1-1.** Ice volume in meters Sea-Level Equivalent (m SLE) departing from present-day ice volume for each of the existing ice distribution for the LGM according to: ICE-1 (Peltier and Andrews 1976), ICE-3G (Tushingham and Peltier 1991), ICE-4G (Peltier 1994), ICE-5G (Peltier 2004), ANU05 (Fleming and Lambeck 2004), IJ05 (Ivins and James 2005) and Kleman et al. (2013). “AIS” stands for Antarctic ice sheet, “GIS” for Greenland ice sheet and “Other” corresponds to the remaining small ice caps over Patagonia, New-Zealand and Iceland.

Reconstruction	Total (m SLE)	Laurentide	Eurasia	AIS	GIS	Other
ICE-1	77	58	16	–	3	–
ICE-3G	115	55	24	26	6	4
ICE-4G	104	59	21	17	6	1
ICE-5G	126	74	17	17	2	2
ANU05	134	86	16	28	3	1
IJ05	–	–	–	8	–	–
Kleman et al. 2013	–	80	20	–	–	–

Those reconstructions from the last decades present total ice volumes starting with a global LGM ice volume of about 77 m SLE in ICE-1 and ending with a global ice volume ranging from 126 m SLE to 134 m SLE in ICE-5G and in ANU05, respectively (Table 1-1). The evolution of the global ice volume in those reconstructions mainly results from adjustments over the Laurentide ice sheets, which gained almost 20 m SLE in the ICE-5G reconstruction compared to ICE-3G. The Eurasian ice volume fluctuated much less, between 24 m SLE in ICE-3G and 16 m SLE in ANU05. The contribution of Antarctica to the LGM global sea-level drop has always been poorly constrained, and reconstructions propose values ranging from 8 m SLE to 28 m SLE. The debate about the Antarctic LGM ice volume is still open but recent research, mainly based on the misfit between past sea-level proxies and glacio-isostatic adjustment modeling (Ivins and James 2005), tends to support the model from Ivins and James (2005), i.e. a small gain in ice volume during the LGM compared to present-day.

The most recent reconstruction, namely ICE-5G uses the Laurentide LGM extent from Dyke et al. (2002) and the Eurasian LGM extent from Svendsen et al. (2004). For the Laurentide ice sheet, the moraines found over North America are dated to the LGM. No geological evidence for a larger glaciation over this area has been found so far. This implies that previous glaciations over North America have been smaller than or no larger than the LGM Laurentide ice sheet. This is supported by marine sediment records that contain low detrital carbonate content at several North Atlantic sites (e.g., de Abreu et al.

2003, Channell et al. 2012), which suggest that iceberg discharges through Hudson Strait in Canada were reduced during the last glaciation compared with other glacials. This further indicates that ice dynamics was less effective than during large-scale continental glaciations such as the LGM.

In contrast, many different moraines dated from different periods back to about 180 kyrs BP have been found associated with Eurasian ice sheets. Over the last decade, the Quaternary Environment of the Eurasian North Project (QUEEN, Svendsen et al. 2004) has been the last big project to focus on the reconstruction of the Eurasian ice-sheet extent over the last ~140 kyrs BP. The reconstruction mainly focused on the last glacial cycle (~130–10 kyrs BP). However, some moraines were dated between ~140 and ~180 kyrs BP, therefore attributed without any doubt to the glaciation of MIS 6 (~192–135 kyrs BP), i.e. the European Saalian period (Illinoian glaciation in North America). The extent provided by the QUEEN project for the Saalian glaciation is much larger than its Last Glacial Maximum (~21 kyrs BP, LGM) counterpart. In particular, the reconstruction extends further eastward and southward in Siberia and in Russia than during the LGM (Figure 1-3). However, the dating of this eastern part, in reality, could be older than the Saalian glacial maximum at ~140 kyrs BP and could have been attributed to previous advances of the Eurasian ice sheet during MIS 6 (Svendsen et al. 2004).

Three advances of the Eurasian ice sheet have been identified so far during the MIS 6 glacial cycle:

- around 180 kyrs BP,
- around 160 kyrs BP,
- around 140 kyrs BP.

Those three advances are linked mainly with summer insolation fluctuations during the whole MIS 6. For those reasons, the various parts of the Eurasian ice sheet that developed during MIS 6 might not have reached their maximum extent at the same moment of the cycle.

For the Western part of the Eurasian ice sheet, the study of sediment records from the Iberian margins suggests that older glaciations could have been extensive over Western Eurasia, i.e. merging the British ice cap with the Fennoscandian main ice body. The eastern Siberian part remains poorly constrained due to a lack of data and it seems that in some areas, the maximum extent might be attributed to MIS 8, whereas in other areas, it might be attributed to MIS 6 (Astakhov 2008). Similarly, attributing the southern extent of the Eurasian ice sheet to MIS 6 remains controversial. According to Ehlers and Gibbard (2007), the MIS 16 and MIS 8 Eurasian ice sheets could have extended as much as during the Late Saalian glaciation (Figure 1-1). However, almost no terrestrial evidence of those glaciations has survived through time and have probably been destroyed by the MIS 6 glaciation.

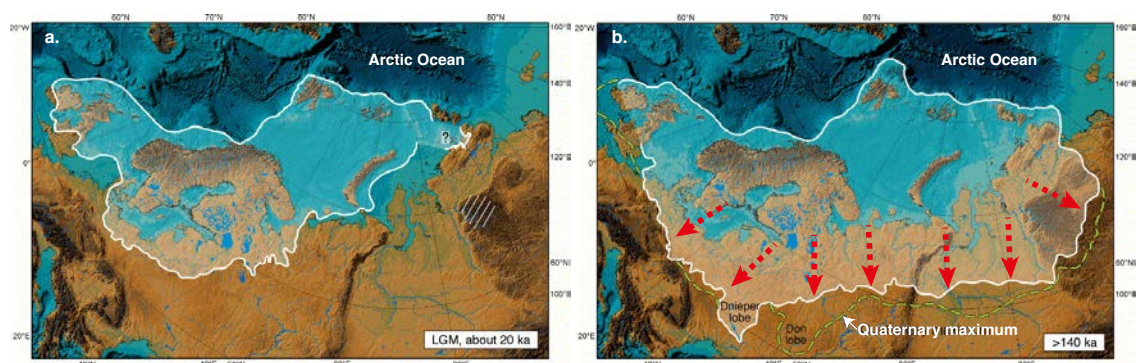


**Figure 1-3.** Comparison of the Eurasian ice sheet dimensions between a. the Last Glacial Maximum ( $\approx 21$  kyrs BP) and b. the Late Saalian glacial maximum ( $\approx 140$  kyrs BP) after Svendsen et al. (2004). Compared to the LGM Eurasian ice sheet extent, the Late Saalian ice sheet expands further south and east (b, red arrows). The largest LGM Eurasian ice-sheet reconstruction (ICE-5G, Peltier 2004) corresponds to an ice volume of  $\approx 22$  m SLE, which is about three times smaller than the Late Saalian Eurasian ice volume ( $\approx 70$  m SLE) simulated by Peyaud (2006).

So far, the penultimate glaciation has not been studied in detail, since most of its climate characteristics differ from the classical glaciation, as characterized by the LGM for example. The Late Saalian glaciation was, according to Masson-Delmotte et al. (2010), the second warmest glacial period during the last 800 kyrs and it preceded MIS 5.5, which likely was one of the warmest interglacials during the Quaternary period. In terms of ice volume, Masson-Delmotte et al. (2010) estimate that the Late Saalian only had the sixth largest global ice volume (LGM is 7th). Marine records from the ACEX campaign reveal that the Arctic sea-ice cover becomes mostly perennial from MIS 7 onward (Polyak et al. 2013). In the Alpine region, the glaciers show advances more extensive during MIS 6 than during MIS 2 (Dehnert et al. 2010). An interesting feature is that the South America tropics are found to be considerably drier during the MIS 6 glaciation than during MIS 2 (Fritz et al. 2004), suggesting that the Inter-Tropical Convergence Zone (ITCZ) could have been located much southward during MIS 6 relatively to MIS 2 (Tisserand et al. 2009). In Antarctica, temperature anomalies relative to pre-industrial climate, derived from deuterium excess (Jouzel et al. 2007), show that the MIS 6 glacial maximum temperature was about 1°C to 1.5°C higher than during the LGM (Figure 1-1).

Only a few coupled climate-ice-sheets models, EMICS, are able to reproduce the large extent of the MIS 6 Eurasian ice sheet and the reasons for success or failure are not understood (Ganopolski, Abe-Ouchi, personal communication). There is no direct evidence for the MIS 6 Laurentide ice sheet extent and volume and no direct evidence for Eurasian ice volume. However, Bintanja and van de Wal (2008) used an ice-sheet model combined with an isotopic model and an atmospheric general circulation model to simulate the evolution of the global ice volume over the last 3 million years. Their simulations show that the average Eurasian ice volume was larger than the average Laurentide one until about 150 kyrs BP.

If we assume that the maximum extent at 140 kyrs BP provided by the QUEEN project and the ice thickness reconstructed by Peyaud (2006) are correct, the ice volume of Eurasia at this period was about 70 m SLE. During the LGM, according to the ICE-5G reconstruction (Peltier 2004), the Eurasian ice sheet represented ~22 m SLE and North America ~74 m SLE. Since sea-level reconstructions for the last two glacial maxima are similar ~126 m SLE, this implies that if we wish to keep the global mass balance in agreement with global sea-level observations and use the MIS 6 extent from the QUEEN project, the MIS6 North American ice sheet should be smaller (Table 1-2). The comparison between various reconstructions, as well as the ones deriving from our study, supports this conclusion. However, the present study is at odds with the modeled ice volume from Peyaud (2006) (~70 m SLE) and is more in agreement with the simulated ice volume from Lambeck et al. (2006) (~60 m SLE).

**Table 1-2. Ice volume comparison of the various MIS 6 reconstructions following Colleoni (2009) departing from present-day ice sheet volume. For MIS 6 glacial maximum, the Eurasian ice sheet is taken from Peyaud (2006). In this table, we compare the total ice volume of four MIS 6 ice sheets distributions: MIS6 Peyaud, in which all the ice sheets are kept as for ICE-5G, except for the Eurasian ice sheet; MIS6 Peyaud+IJ05, which is similar to MIS6 Peyaud, except for Antarctica for which we considered the model from Ivins and James (2005); B140\_Topo1 corresponds to our climate simulations in which we prescribed the Late Saalian ice topography from MIS6 Peyaud and in the case of B140\_Topo2 a smaller Laurentide ice sheet; MIS6 Topo1 (Ref), which corresponds to the modeled reference Eurasian ice sheet obtained using B140\_Topo1 climate forcing from the present study; MIS6 Topo2 (Ref), for which Eurasian ice sheet was obtained using B140\_Topo2 climate forcing and accounts for a smaller Laurentide ice sheet following Colleoni (2009). Red numbers highlight the reconstructions in which the total ice volume exceeds paleo-sea-level reconstructions displayed in Figure 2. Note that MIS6 Topo1 ice volume reaches the lower bound of sea-level observations while MIS6 Topo2 ice volume corresponds to the upper bound of sea-level observations. For comparison, ICE-5G ice sheets volume is also shown.**

Reconstruction	Total (m SLE)	Laurentide	Eurasia	AIS	GIS	Other
ICE-5G	126	74	17	17	2	2
MIS6 Peyaud	165	74	70	17	2	2
MIS6 Peyaud + IJ05	156	74	70	8	2	2
B140_Topo1	165	74	70	17	2	2
B140_Topo2	121	30	70	17	2	2
MIS6 Topo1 (Ref)	146	70	55	17	2	2
MIS6 Topo2 (Ref)	104	30	53	17	2	2

The Late Saalian glaciation is certainly not the only extensive glaciation that occurred over Eurasia during the Late Pleistocene period. However, geological traces of the extent of those previous glaciations were not preserved through time. Studying the Late Saalian glaciation, for which more geological evidence is available, is therefore a good way to understand what could happen in the case of more a future extensive glaciation than that at the LGM over Eurasia, including Fennoscandia and the Forsmark area.



## 3 Climate simulations

### 3.1 Climate model and settings of the simulations

To perform the climate simulations, we use the Community Earth System Model (CESM) developed at NCAR (Gent et al. 2011). CESM is a fully coupled atmosphere-ocean-sea-ice-land model. The atmospheric component CAM has 26 vertical levels and a horizontal grid shared with the land component (CLM). The ocean component (POP, displaced pole located over Greenland) has 60 vertical levels and a horizontal grid in common with the sea-ice component (CICE). The simulation is run using a horizontal resolution of  $0.9^\circ \times 1.25^\circ$  and a finite volume grid. In our simulations, we used CAM4, which does not account for sophisticated atmospheric chemistry such as in the newer CAM5 version, therefore, our model configuration corresponds to the Community Climate System Model 4 (CCSM4, earlier version of CESM). Vegetation and aerosols are as for pre-industrial. Vegetated areas that are covered by ice sheets are specified as “glacier Plant Functional Type” and are attributed a corresponding albedo value. In terms of performance, the CCSM4 shows noticeable improvements compared with CCSM3. However, CCSM4 still has significant biases, regarding the mean precipitation distribution in the tropical Pacific Ocean, too much low clouds in the Arctic, and the latitudinal distributions of shortwave and longwave cloud forcings (Gent et al. 2011).

In total, two climate simulations, namely B140\_Topo1 and B140\_Topo2, were carried out both using Late Saalian glacial maximum orbital parameters and atmospheric greenhouse gas concentrations (GHGs) appropriate to 140 kyrs BP, but using two different topographies (Topo1 and Topo2) from Colleoni et al. (2009b). Topo1 is constituted by the North American, Antarctica and Greenland Last Glacial Maximum ice sheets from ICE-5G (Peltier 2004) and the MIS 6 Eurasian ice sheet from Peyaud (2006) (Figure 3-1a). The elevation reaches about 3,500 meters over Eurasia and 4,500 meters over North America. The total initial ice volume introduced in the climate simulation is about ~169 m SLE distributed over the Laurentide ice sheet (~74 m SLE), over the Eurasian ice sheet (~70 m SLE) and over Antarctica (~17 m SLE) (see Table 1-2). Note that the Eurasian ice sheet volume equals that of the Laurentide. In practice, the topography corresponds to that of Peltier (2004) for the LGM, except over Eurasia where we implemented the Late Saalian Eurasian ice sheet. Given the uncertainties upon the eustatic sea-level reconstructions for MIS 6, we adopted the LGM land-sea mask, except along the Eurasian Arctic continental margins, i.e. corresponding to a global sea-level drop of about 120 m. This assumption is reasonable since 120 m SLE roughly corresponds to a mean value between the upper and lower bound of MIS 6 sea-level reconstructions. Moreover, most of the changes in the land-sea mask during a glaciation occur in the northern and southern high latitudes. Therefore, using the LGM land-sea mask in the mid and low latitudes seems reasonable. As a consequence of LGM sea-level drop, in the Northern Hemisphere, aside from the continental areas that are ice covered, the Bering Strait is closed, the Canadian archipelago is ice-covered and the Siberian continental shelf emerges (Figure 3-1a).

**Table 3-1. Orbital forcing (Berger and Loutre 1991) and GHGs concentrations values (Petit et al. 2001, Spahni et al. 2005) for Late Saalian B140\_Topo1 climate simulation. The values correspond to the glacial maximum of this time period, i.e. ≈140 kyrs BP. For comparison, we also show LGM (≈21 kyrs BP) and present-day external forcing values.**

	140 kyrs BP	21 kyrs BP	Present-day
Eccentricity	0.033	0.019	0.017
Precession (°)	0.031	0.017	0.016
Obliquity (°)	23.42	22.95	23.45
Perihelion date	December 6	January 17	January 7
CO <sub>2</sub> (ppmv)	192	194	367
CH <sub>4</sub> (ppmb)	401	354	1,760

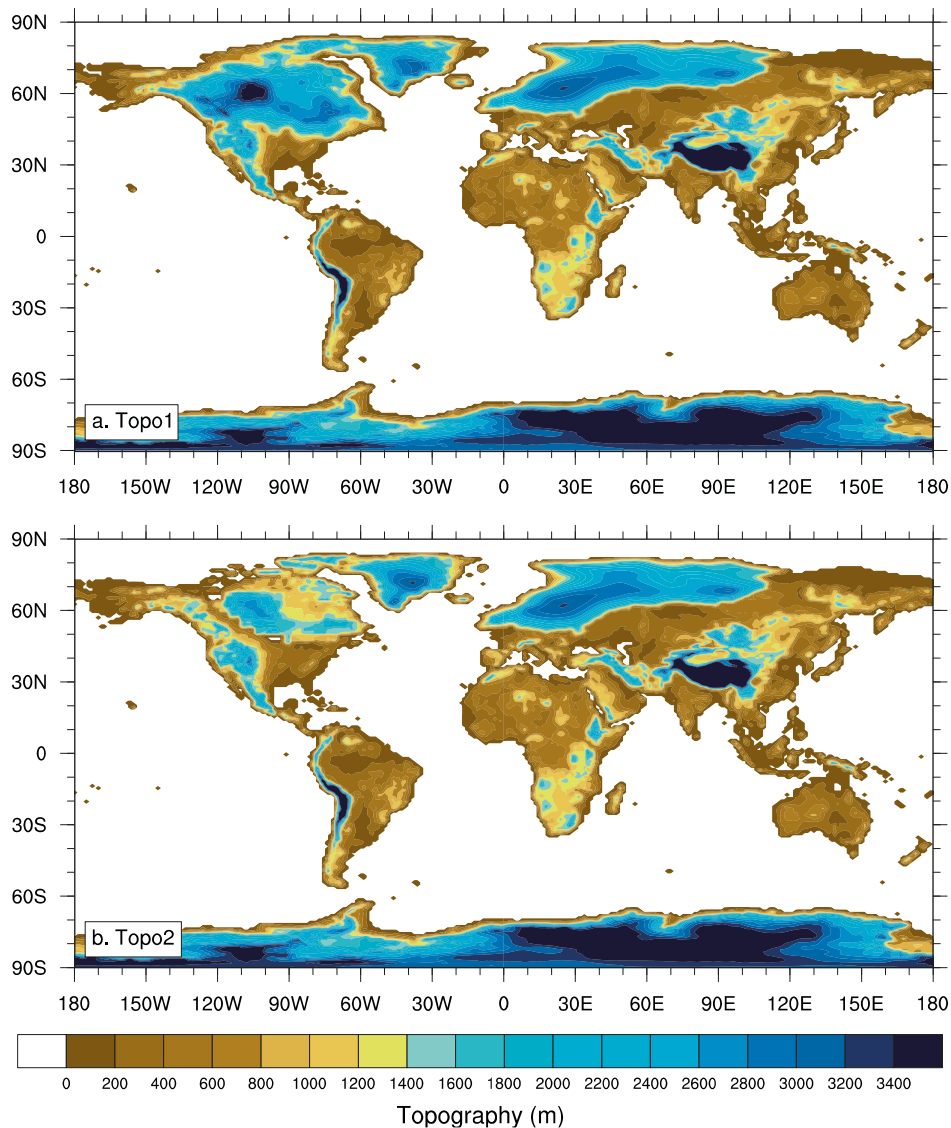


**Figure 3-1.** Late Saalian global topography (~140 kyrs BP) as reconstructed in Colleoni (2009). Laurentide ice sheet corresponds to ICE-5G (Peltier 2004) Last Glacial Maximum reconstruction (~21 kyrs BP, LGM). Eurasian ice sheet corresponds to the Late Saalian reconstruction from Peyaud (2006). Since there is no precise evidence about Antarctic ice-sheet topography during the Late Saalian period, we used ICE-5G LGM reconstruction. Horizontal resolution of the figure corresponds to the resolution of the B140\_Topo1 CESM simulation, i.e.  $0.9^{\circ} \times 1.25^{\circ}$ .

This reconstruction is somewhat idealized since it exceeds the upper bound of observed past sea level. However, we do not have any geological evidence about the size of the Laurentide ice sheet for the Late Saalian period (the traces of this glaciation were destroyed during the Last Glacial Maximum). Therefore, in addition to this simulation, we tested another configuration, Topo2, this time accounting for a smaller Laurentide ice sheet of about 30 m SLE following Colleoni (2009). The ice is distributed as follows: Laurentide (~30 m SLE), Eurasia (~70 m SLE), Antarctica (~17 m SLE). This leads to a total ice volume of about 121 m SLE, which is more in agreement with past sea level observations (Figure 1-2). The Topo2 topography is displayed in Figure 3-1b.

We also set up orbital parameters (Berger and Loutre 1991),  $\text{CO}_2$  (Petit et al. 2001) and  $\text{CH}_4$  (Spahni et al. 2005) as for the Late Saalian glacial maximum ~140 kyrs ago (Table 3-1). During the Late Saalian glacial maximum, Earth is at perihelion, i.e. the shortest distance to the Sun, in early December and has a large eccentricity and obliquity compared with the LGM. Consequently, the Northern Hemisphere summer occurs at aphelion (the farthest distance to the Sun), which is a pre-requisite to preserve the perennial snow cover accumulating during the winter. This orbital configuration

is particularly favorable to glaciation even more so than the LGM since the large eccentricity and obliquity enhance the seasonal contrast. Therefore, Late Saalian winters were particularly mild, advecting lots of moisture over the high latitudes, whereas summers were particularly cold, allowing the snow cover to become perennial. Moreover, the low CO<sub>2</sub> and CH<sub>4</sub> concentrations, i.e. comparable to those of the LGM, further helped for the maintenance of glacial conditions in high latitudes.

Both climate simulations, B140\_Topo1 and B140\_Topo2, were set up according to the values in Table 3-1 and were run for 700 model years. Due to the extreme ice-sheet forcing of those simulations, it appears that 700 model years are not enough to reach a global equilibrium using the coupled AOGCM (Figure 3-2). The ocean heat content of the first 400 meters is not totally at equilibrium at the end of the simulations (Figure 3-2f). However, the model spin-up (i.e. equilibrium with the prescribed Late Saalian topographies, orbital parameters and GHG concentrations) is achieved after 700 model-years and we assume that the slight drift that remains will not substantially affect our ice sheet simulations.

Since the ice-sheet model is run over the Northern Hemisphere extratropical latitudes (37°N–90°N), we considered the spin-up over the Northern Hemisphere only. Over this domain, surface variables are slightly closer to equilibrium after 700 model years than the global values (Figure 3-2b and 3-2d). It was therefore decided to not further run B140\_Topo1 and B140\_Topo2 and use the simulated climates to force the ice-sheet model. During the spin-up of B140\_Topo1, mean annual global air surface temperature and sea surface temperature (SST) drop by about 1.5°C, which is mostly due to the cooling of the Northern Hemisphere high latitudes due to the presence of the ice sheets (Figure 3-2a, 3-2e and 3-2b). At a first approximation, this cooling seems to be limited, but what matters most for glacial climates is the seasonal contrast. Cooling the global climate by 1.5°C is difficult and this value here shows the large-scale circulation changes that arise in B140\_Topo1.

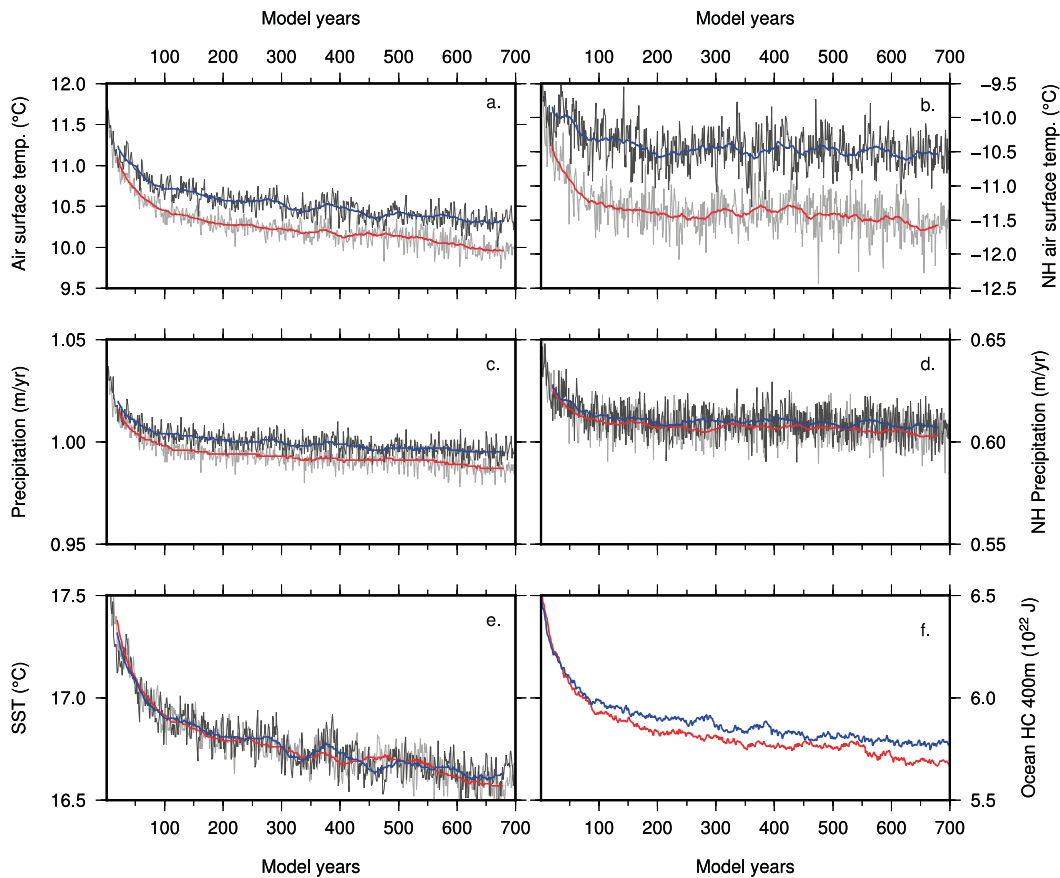


**Figure 3-2.** Spin-up of B140\_Topo1 (red) and B140\_Topo2 (blue) simulations. Zonal and meridional global mean annual average of surface air temperature (a.), precipitation (c.) and SST (e.). Zonal and meridional Northern Hemisphere (37°N–90°N) mean annual air surface temperature (b.) and precipitation (d.). Ocean heat content ( $10^{22}$  Joules), calculated over the first 400 meters, is displayed in frame f.

In B140\_Topo2, the global spin-up leads to a temperature drop of about 1°C, slightly less than in B140\_Topo1 (Figure 3-2a). This is mostly due to the fact that the Laurentide ice sheet is smaller in B140\_Topo2 than in B140\_Topo1, therefore, the albedo changes in the Northern high latitudes are less important than in B140\_Topo1, thus limiting the drop in temperature in this area (Figure 3-2b). Changes in precipitation and SST remain however similar between the two simulations (Figure 3-2c, 3-2d and 3-2e).

### 3.2 Comparison between simulated and marine SST records

Comparing simulated SSTs with marine SST records is interesting since SST is at the interface between atmosphere and ocean and can reveal potential circulation issues of the model. The methods used to estimate SST from marine sediments commonly have a bias towards summer temperatures (Goni et al. 2001). For this reason, Figure 3-3 displays the comparison between SST records and simulated mean summer SST (June-July-August) for the Late Saalian glacial maximum (~140 kyrs BP). Note that the comparison is only indicative of whether or not the main oceanic gyres and fronts are located in the right areas. In both simulations, the simulated tropical SST between 30°N–30°S is warmer than the SST proxies. This could be related to the fact that CESM, as with other coupled climate models, simulates a double ITCZ in the tropics, which induces a bias in ocean-surface circulation. At the Southern high latitudes, both simulations are in good agreement with the proxies, which suggest that the surface wind circulation and the sea-ice cover are well represented. At the Northern high latitudes, the simulated SST tends to be slightly colder than the proxies for both simulations, and especially in B140\_Topo2 due to the changes in stationary waves resulting from the lower Laurentide ice sheet (see next section for further explanation). In the North Atlantic, the wind circulation is too strong in general, and, combined with the issue of the double ITCZ, it causes the tropical surface waters to expand northward further than where they should be, especially in B140\_Topo2.

From this comparison, we can conclude that the Late Saalian ice topographies that we use for our simulations generate a mean flow over the Northern high latitudes stronger than it should be. As a consequence, it might slightly increase the amount of moisture that is advected from the North Atlantic to the west and south of the Eurasian ice sheet. However, since the Late Saalian Eurasian ice sheet is very high and large, only the ice sheet margins would be affected by this process. Given that the 0°C summer isotherm largely reaches the southern margins of the ice sheet, the excess in precipitation would not contribute to a significant growth of the ice sheet. In the tropics, the model encountered the classical tropical issue, that is in general it is difficult to cool the tropical band during the LGM as much as what the proxies suggest (Kageyama et al. 2013).

### 3.3 Climate analysis

In the following, we present the main climate variables substantially affected by the changes in topography and albedo introduced in B140\_Topo1 and B140\_Topo2. All the variables presented below have been averaged over the last 50 years of the simulations and are all mean annual averages, except for sea-ice for which seasonal minimum and maximum are discussed. For a better understanding, some of the variables are compared with a simulation of pre-industrial conditions (using similar resolution) that we performed for the need of comparison.

Compared with the pre-industrial temperatures, global air surface temperatures are lower in B140\_Topo1. This is the result of the lower GHGs concentrations and of the presence of the large ice sheets over the Northern Hemisphere whose elevation and albedo feedback contribute to decrease mean annual Northern Hemisphere temperature by about 15°C over the Arctic Ocean by up to 34°C over both ice sheets (Figure 3-4b). The large cooling simulated over the Arctic region combined with changes in the large-scale circulation causes an overall drying (Kageyama and Valdes 2000). Mean annual precipitation over the Arctic region decreases by about 30% and up to 80% over the ice sheets (Figure 3-4e). Since the climate is much cooler than during the pre-industrial period, the synoptic circulation has also intensified as shown by the increase in precipitation (~20 to 40%) simulated in the North Atlantic and Northeast Pacific mid-latitudes. As a consequence, the Gulf Stream is also deviated northward with SST exhibiting a slight increase of 2°C compared with pre-industrial values south of Greenland (Figure 3-4h).

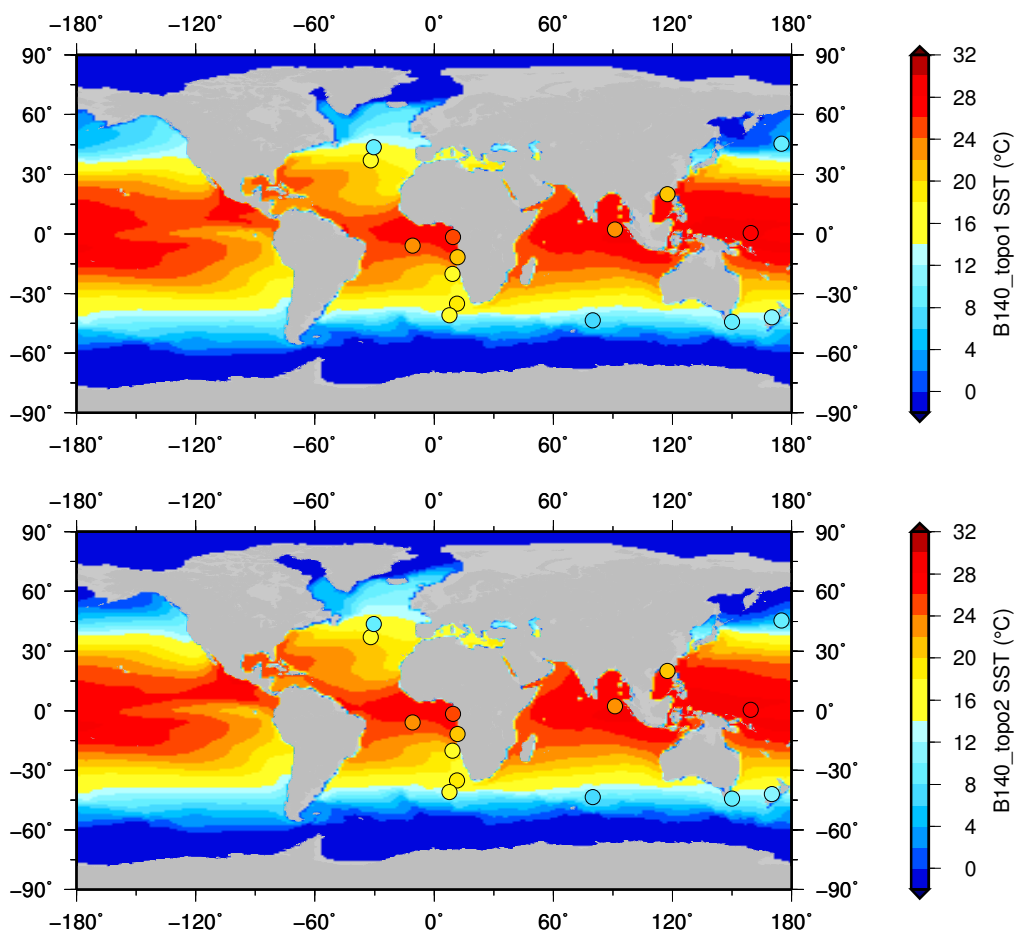


**Figure 3-3.** Comparison between computed mean summer sea surface temperatures (SST, June-July-August) for B140\_Topo1 (top) and B140\_Topo2 (bottom) and Late Saalian glacial maximum (~140 kyrs BP) marine sediment cores SST records (circles, in °C) summarised in Table A1-1 (Appendix 1). Each circle corresponds to one marine site and is compared to the associated model pixel.

The intensification of the cooling in the Northern high latitudes combined with the intensification of the wind circulation at mid-latitudes induces a large southward shift of the tropical convective system, therefore moving the Inter-Tropical Convergence Zone in the Southern Hemisphere. The maximum precipitation is thus computed in the Southern Hemisphere, both in the Atlantic and Pacific oceans, causing a drying of the Central America and Saharan areas amounting to more than 40%. In addition, due to the cooling of the Northern Hemisphere mid-latitudes and to the deviation of circulation caused by the presence of the Eurasian ice sheet over the continent, Southeast Eurasia experiences a drying of about 40%.

Compared with B140\_Topo1, B140\_Topo2 has a lower and less extensive Laurentide ice sheet (Figure 3-1). As a consequence, the mean annual temperature is higher by about 12°C over North America. Mean annual temperatures are also higher by about 14°C off Iceland because this area is ice-covered in B140\_Topo1, while it is ice-free in B140\_Topo2 (Figure 3-4b and 3-4f). Further, the combination of a lower Laurentide ice sheet with a reduced sea-ice cover induces a warming over the Eurasian ice sheet of about 2°C to 4°C. In addition, due to the orographic effect of the small Laurentide ice sheet, precipitation is three times larger over the Eastern part of the Laurentide ice sheet and over the North Atlantic (Figure 3-4d). This orographic effect also intensifies precipitation by about 10% to 60% over the northern and eastern part of the Eurasian ice sheet. Similarly, precipitation increases by 60% over Alaska (Figure 3-5f). Because the mean background climate state is colder over the Northern high latitudes, this increase in precipitation results in the accumulation of a perennial snow cover over this area, which induces a further drop in temperature of about 6°C (Figure 3-4b). The drop in temperature is in turn favorable to the expansion of the sea-ice cover in the Bering Sea (Figure 3-4f). Note that the ITCZ is globally shifted northward in B140\_Topo2 with respect to B140\_Topo1 as a result of the lower Laurentide elevation and the warmer Northern Hemisphere temperatures (Figure 3-4d).

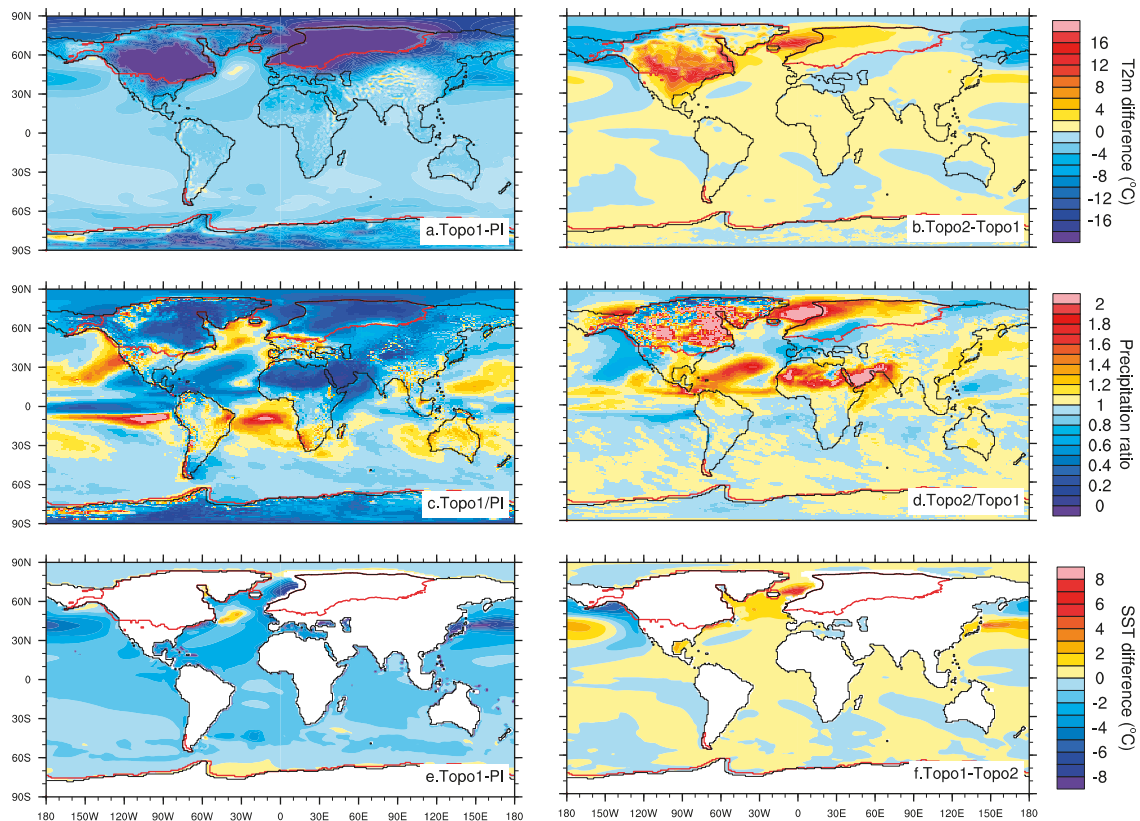


**Figure 3-4.** Mean annual surface air temperature, precipitation and sea surface temperatures: a. Air surface temperature difference between B140\_Topo1 and Pre-industrial ( $^{\circ}\text{C}$ ). Note that the scale maximum and minimum are saturated; b. same as for a. but between B140\_Topo2 and B140\_Topo1 ( $^{\circ}\text{C}$ ); c. Mean annual precipitation ratio between B140\_Topo1 and Pre-industrial (dimensionless); d. same as for c. but between B140\_Topo2 and B140\_Topo1 (dimensionless); e. Mean annual SST difference ( $^{\circ}\text{C}$ ) between B140\_Topo1 and Pre-industrial; f. same as for e. but between B140\_Topo2 and B140\_Topo1. Red contours correspond to landice-covered areas.

In the following analysis, we focus on the Northern Hemisphere mid to high latitudes where the largest changes occur and are of interest to better understand the outputs of the ice-sheet simulations. One of the most characteristic changes in the Northern high latitude synoptic circulation occurring during a glacial period is the intensification of the storm activities and the geographical shifting of storm activity in the North Atlantic (Kageyama et al. 1999). This effect is caused by an intensification and a deviation of the subtropical jet due to the presence of the ice sheet over North America, creating a topographic barrier high enough to deviate the flows southward of their normal location (Figure 3-5d and 3-5f, e.g. Kageyama and Valdes 2000, Pausata et al. 2011). In B140\_Topo1, storm tracks are effectively deviated southward. The main center of activity, usually located over Iceland, has moved south of Greenland. The second impact of high topography over North America on the North Atlantic storm tracks is to decrease the cyclogenesis and therefore decrease the intensity of the storm tracks compared with the pre-industrial simulation (Figure 3-5a and 3-5c). Similarly, in B140\_Topo2, the effect of the lower Laurentide elevation is to increase the cyclogenesis due to the fact that the mean flow strengthens and becomes more baroclinic over North America. As a consequence, the storm tracks intensity increases over the North Atlantic (Figure 3-5b and 3-5e).

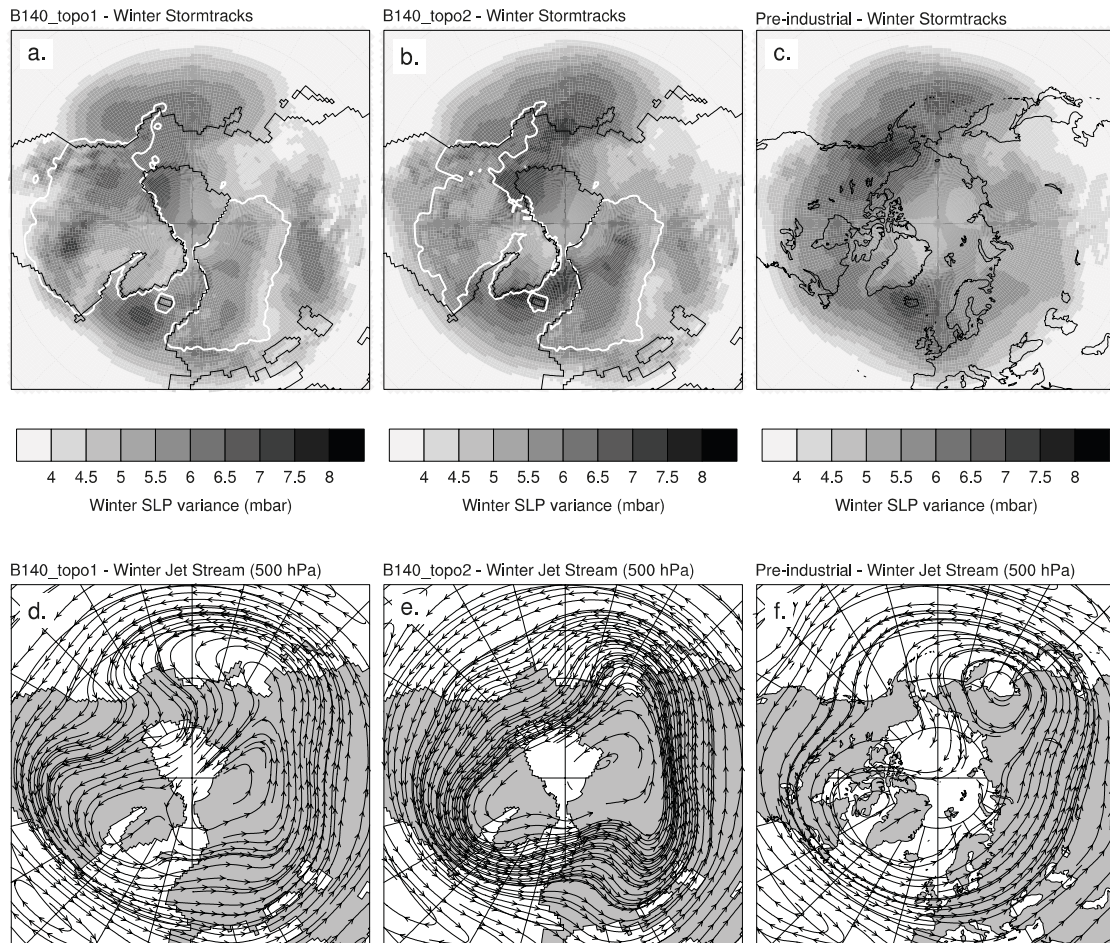


**Figure 3-5.** Storm track activity for B140\_Topo1 (a), B140\_Topo2 (b) and pre-industrial (c). Storm track activity is represented by the Northern hemisphere variance of band pass filtered (3:7) winter (DJF) sea-level pressure (mbar), following the method of Kageyama et al. (1999). White contours in (a) and (b) correspond to the ice-sheets distribution from B140\_Topo1 and B140\_Topo2, respectively. Jet streams (500 hPa winter winds) for B140\_Topo1 (d), B140\_Topo2 (e) and pre-industrial (f). The three frames display flow lines corresponding to the 10 m/s wind speed.

The presence of the Northern Hemisphere ice sheets has a large impact on the jet stream, and particularly during winter. In B140\_Topo1, the jet is deviated northward near to the western coast of Canada, where the elevation due to the presence of the Laurentide ice sheet reaches about 3,000 meters in a few tens of kilometers. The topographic barrier deviates a larger part of the jet towards the Arctic, bringing much cooler air to the Northern part of the Laurentide and the Eurasian ice sheets (Figure 3-5d). Furthermore, the Eurasian ice-sheet topography contributes to the creation of an anti-cyclonic circulation over the northernmost part of the ice sheet. In the North Atlantic, the flow does not go northward over the Nordic Seas as much as in the pre-industrial simulation because of the presence of the Eurasian ice sheet that deviates the flow slightly more southward (Figure 3-5d). In B140\_Topo2, on the contrary, the deviation of the jet stream is less pronounced than in B140\_Topo1, but the anti-cyclonic circulation over the Eurasian ice sheet persists (Figure 3-5e). It is worth noting that the difference in elevation between these two simulations, about 1,000 meters over North America (Figure 3-1), is enough to substantially affect the stationary wave and restore the direction of the mean flow over the mid latitudes (Figure 3-5d). However, because of the high Eurasian ice sheet, the mean flow in B140\_Topo2 is still stronger than in the pre-industrial simulation.

The two topographies Topo1 and Topo2 directly influence the stationary waves, which in turn affect the spatial pattern of precipitation that is simulated over the Northern high latitudes. As a result, the snow cover shows discrepancies between B140\_Topo1 and B140\_Topo2. The snow cover is at the basis of the astronomical theory of ice ages, which states that if the snow becomes perennial, i.e. resists to summer insolation, an ice sheet can grow over the continent. In our case, perennial snow is an indicator of whether our ice sheet can further expand or not with the simulated climate set-up with the Late Saalian glacial maximum external forcing values. We determined the snow cover, using the simulated daily field of snow depth and stating that perennial snow corresponds to a residence time of 365 days per year. If for one day snow melts completely in a pixel, it is not considered as perennial snow. In both simulations, snow becomes perennial, first on the top of the ice sheets, indicating that the surface mass balance of the Late Saalian ice sheets is positive in our climate simulations (Figure 3-6a and 3-6b). In addition, in B140\_Topo1, the snow becomes perennial over part of Eastern Siberia and reaches the Arctic margins of Alaska (Figure 3-6a).

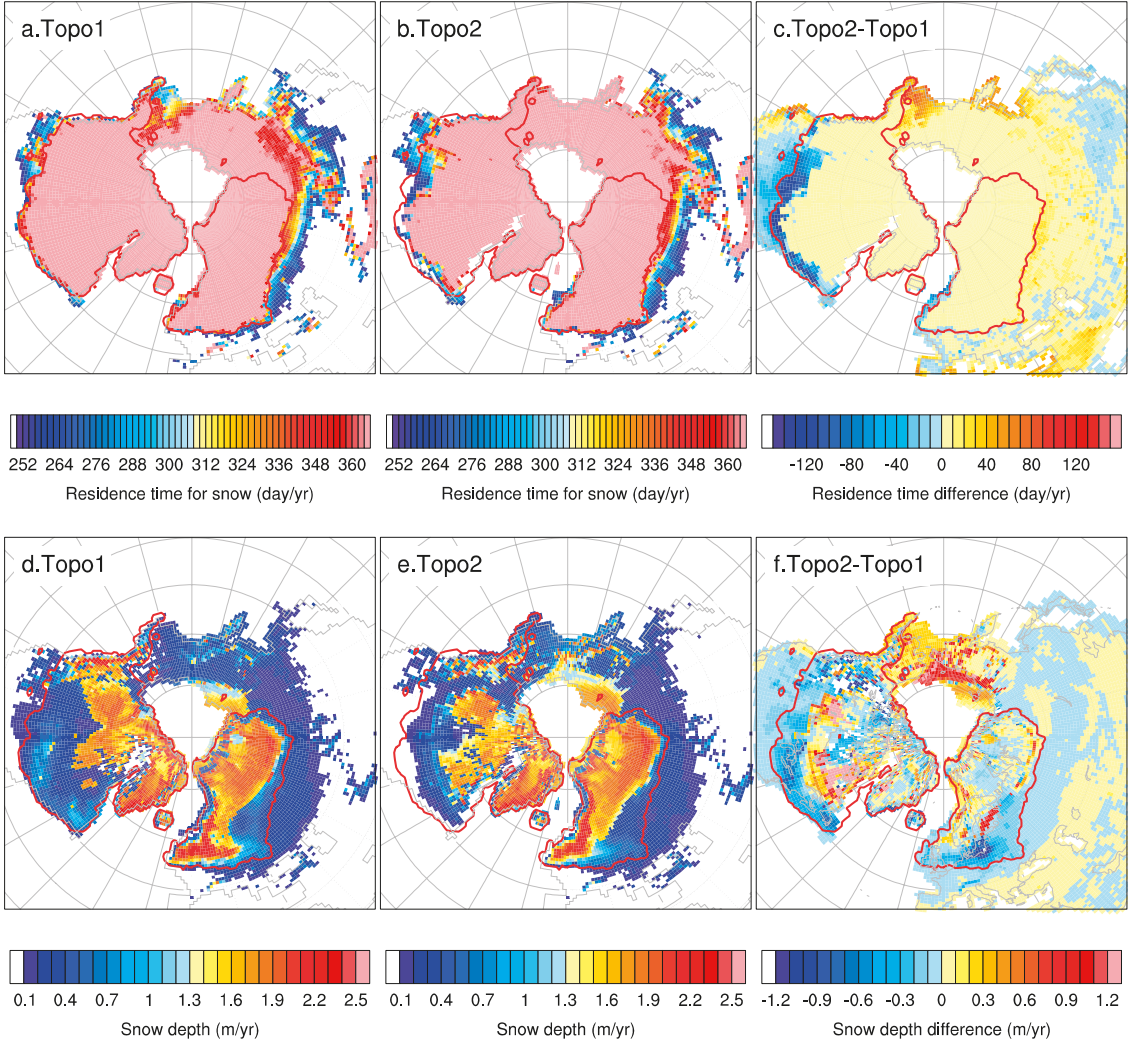


**Figure 3-6.** a. B140\_Topo1 residence time for snow (day/yr). Perennial snow cover was determined based on a residence time of 365 days per year (pink color). Note that the color bar was truncated and starts from 252 days to increase legibility. b. B140\_Topo1 snow depth (m/yr). c. same as for a. but for B140\_Topo2, d. difference in snow depth between B140\_Topo2 and B140\_Topo1. Red contours denote the Late Saalian ice sheets as prescribed in B140\_Topo1.

In B140\_Topo2, since the low Laurentide ice sheet allows for more precipitation advection over those areas, the entire Eastern Siberian and Alaska areas exhibit some perennial snow (Figure 3-6b). This could indicate that a smaller Laurentide ice sheet is more favorable to the growth of the Eurasian ice sheet if the climate is cold enough, which is in agreement with Kageyama and Valdes (2000). This also supports the hypothesis that to grow a large Late Saalian Eurasian ice sheet, the MIS 6 Laurentide ice sheet had to be much smaller than in Topo1, to allow more precipitation to reach Eurasia. A small MIS 6 Laurentide ice sheet, at least smaller than the LGM one, is in agreement with IRD records that show a decrease in iceberg fluxes during the MIS 6 glaciation from North America (de Abreu et al. 2003, Channell et al. 2012).

It is also worth noting that along the southern margin of the Eurasian ice sheet, the snow is not perennial (Figure 3-6a and 3-6b). This indicates that snow melt occurs during summer because the ice sheet extends far to south and therefore meets with the 0°C isotherm during summer. Generally, snow depth is low and does not exceed 0.2 meter in the Russian and Siberian Plains in either of the simulations (Figure 3-6d and 3-6e). In contrast, over the northern part of both the Laurentide and the Eurasian ice sheets, snow depth reaches 2.2 meters, which can be explained by the large advection of precipitation over those areas corresponding to the main flow directions of the synoptic circulation (Figure 3-5). Snow depth is also large over the Eastern Siberian shelf in the Beringia area, of the order of 1.5 meters in B140\_Topo1 and this area expands eastward reaching the Chukchi Sea in B140\_Topo2 (Figure 3-6d and 3-6e), whose shelf is emerged in our simulations. This is the consequence of the sea-level drop introduced in the topography in both simulations. When lowering sea-level by about 120 meters, this part of the continental shelf is exposed to the atmosphere. Then in the land model of CESM, the new exposed part has to be categorized among one of the existing Plant Functional Types and land use. In our case, we set all the new exposed lands to bare ground, i.e. with no vegetation.

Therefore, in response to the particularly low temperature simulated in the Arctic regions, this continental shelf becomes immediately covered by perennial snow and fed with the same amount of precipitation as occurs all along the Arctic margins. Nevertheless, in B140\_Topo2 snow depth is larger by about 0.5 m/yr to 1 m/yr over this area than in B140\_Topo1 (Figure 3-6f). This fact is important for the interpretation of the ice-sheet simulations in the next section. It has also been suggested by Mahowald et al. (1999), Krinner et al. (2006), and Colleoni et al. (2009b) that a large amount of dust deposition could occur over this area and induces a decrease in albedo and an increase in local temperature, which in turn stops snow from accumulating. However, a recent contribution from Niessen et al. (2013) shows geological evidence of a large ice cap that developed over the Beringia area during old extensive glaciations, but not during the LGM. They conclude that compared with the LGM, the atmospheric circulation as well as the moisture source could have differed significantly (Figure 3-7).

Perennial snow cover also accumulates on top of the sea-ice cover in the Arctic Ocean in both simulations (not shown). In B140\_Topo1, sea-ice thickness reaches 12.5 meters in the central Arctic (Figure 3-8a), which is coherent with the thickness found for a CESM simulation of the Last Glacial Maximum (~10 meters thick, Otto-Bliesner et al. 2006). Some seasonal sea ice also forms in the Norwegian Basin, between Greenland and Norway. In this area, sea ice melts at the end of the summer and retreats along the Eastern Greenland coasts, while no sea ice subsists in the Labrador Sea (Figure 3-9d). The fact that the sea-ice cover does not expand southward in our simulations is due to two effects: first, the Gulf Stream is deviated northward due to a stronger surface wind circulation, which brings warmer waters in the Labrador Sea areas and South of Iceland (Figure 3-4e), second, the glacial topography causes the Fram Strait to be narrow, which reduces the sea-ice transport.

In B140\_Topo2, sea ice is thicker than in B140\_Topo1 and reaches 13.5 meters in the Central Arctic (Figure 3-8b and 3-8e). This is due to larger precipitation rates that occur along the continental Arctic margins, combined with the sea-ice drifting, which induces a thickening of the overall Arctic sea-ice cover (Figure 3-4d). Because sea ice is thicker in B140\_Topo2, the export through the Fram Strait decreases. In addition, due to the orographic effect of the lower Laurentide ice sheet, temperatures are also warmer over the northern high latitudes (Figure 3-4b) and the storm activity is more intense and is shifted northward in the North Atlantic compared with B140\_Topo1 (Figure 3-5a and 9b). All together, these factors stop the sea-ice cover from expanding southward in B140\_Topo2.

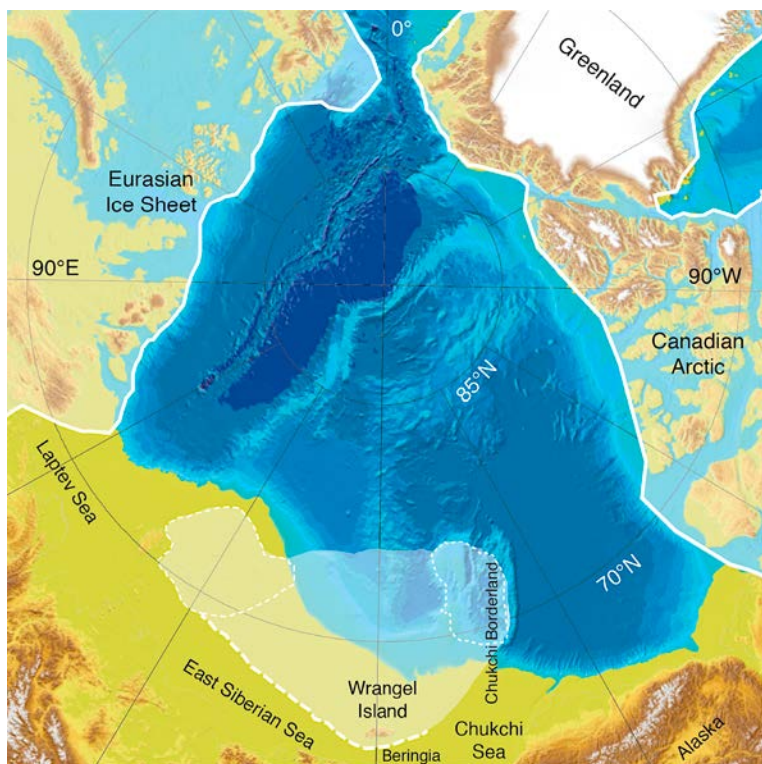


**Figure 3-7.** Proposed maximum extent of an ice sheet on the East Siberian continental during the Pleistocene glaciations after Niessen et al. (2013). White contours denote the maximum extent of Arctic glaciations, regardless of the age, from Ehlers and Gibbard (2007).

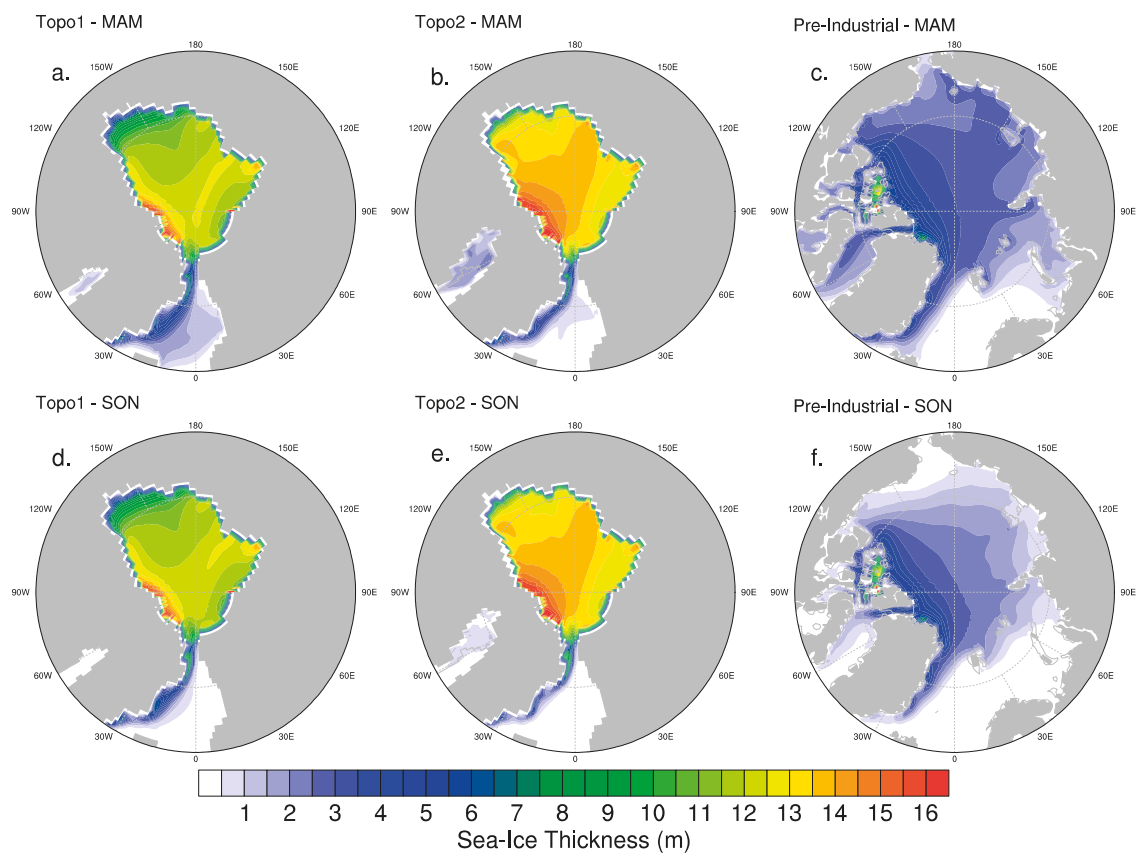


**Figure 3-8.** Spring (March-April-May) and Fall (September-October-November) Arctic sea-ice thickness for B140\_Top1 (a. and d.), B140\_Top2 (b. and e.) and Pre-industrial (c. and f.) simulations.

Finally, the simulated Late Saalian Atlantic Meridional Overturning Circulation (AMOC) is much more vigorous than during the pre-industrial period (Figure 3-9) in both simulations. Since the climate is extremely cold in B140\_Topo1, the convection process reaches a larger depth than in the pre-industrial simulation and consequently, the AMOC is generally deeper in B140\_Topo1 (Figure 3-9a). In addition, since the sea ice extends further to the south in B140\_Topo1, the convection clearly weakens at 60°N while in the pre-industrial simulation, convection occurs also beyond this latitude. The strength of the AMOC reaches 34 Sv (Sv=Sverdrup, volume flow rate equals to  $10^6\text{m}^3/\text{s}$ ) in the subtropics for the Late Saalian period and almost 28 Sv for pre-industrial at the same latitudes. The fact that the AMOC is so vigorous in our Late Saalian simulation means that the heat transport towards the northern high latitudes is larger than during the pre-industrial period to compensate for the large cooling caused by the presence of large ice sheets over the continents. Note also that the Antarctic Bottom Water (AABW) does not reach the Northern high latitudes in B140\_Topo1 and is only slightly more developed in the pre-industrial simulations. We would like to stress that the strength of the AMOC is model dependent, as shown by Otto-Bliesner et al. (2006).

But in our case, since we are testing an extreme glaciation, the AMOC is more vigorous than what the literature shows for the Last Glacial Maximum simulations (about 28 Sv). In B140\_Topo2, similarly to B140\_Topo1, convection is deeper than in the pre-industrial simulation (Figure 4-2b). However, since the B140\_Topo2 climate is generally warmer than B140\_Topo1 in the northern high latitudes, the convection is also weaker than in B140\_Topo1 and the maximum strength reaches 30 Sv. Convection still occurs beyond 60°N, similarly to the pre-industrial simulation, because the North Atlantic remains mostly ice-free throughout the year.

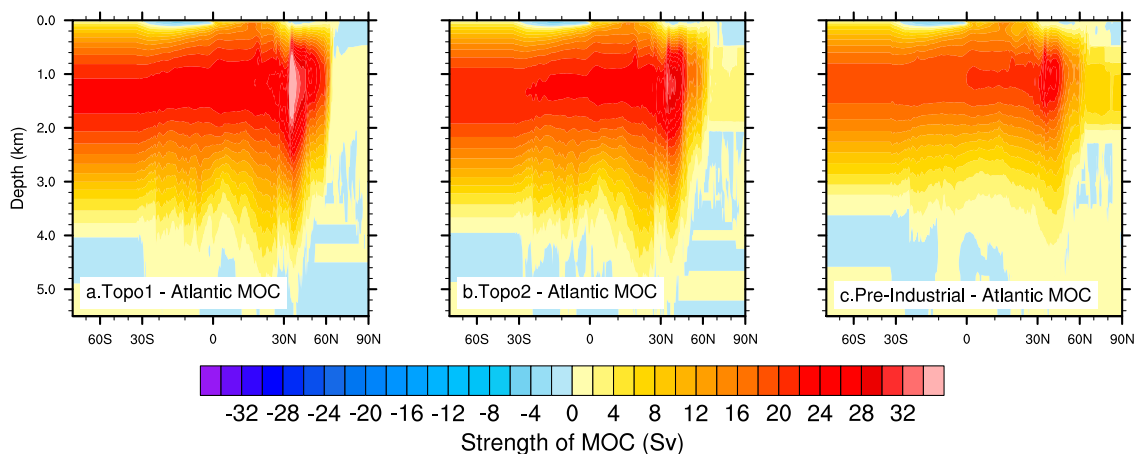


**Figure 3-9.** Atlantic Meridional Overturning Circulation (Sv) for B140\_Topo1 (a.), B140\_Topo2 (b.) and pre-industrial (c.).

## 4 Ice sheet simulations

### 4.1 The GRISLI ice-sheet model

To simulate the Late Saalian Eurasian ice sheet, we use the 3D-thermo-mechanical ice-sheet-ice-shelves and ice-stream model GRISLI (GRenoble Ice Shelf and Land Ice model, Ritz et al. 2001). GRISLI is able to simulate both grounded and floating ice. The grounded part uses the Shallow Ice Approximation (SIA, Hutter 1983) whereas ice shelves and ice streams are simulated following the Shallow Shelf Approximation (SSA, MacAyeal 1989). The ice shelf formulation in GRISLI allows for a more realistic calculation of the ice-sheet growth, and particularly of the advance of ice onto the shallow continental shelves in the high latitudes of both hemispheres. GRISLI has been validated over Antarctica (Ritz et al. 2001) and successfully applied to study the inception of ice sheet growth during the Early Weichselian period (Peyaud et al. 2007, Alvarez-Solas et al. 2011). In the following, we give a detailed description of the model. Notation of the main variables is listed in Table A2-1 and Table A2-2.

#### 4.1.1 Definition of ice flow in GRISLI

In GRISLI, three different regions of ice flow are considered: ice sheets, ice stream zones and ice shelves. Ice sheets and ice stream zones are regions with grounded ice, whereas ice shelves are regions with floating ice. During the simulation, the location of these different regions is determined in every time step. The three different regions are characterized by distinct flow behavior:

1. Ice sheets (inland ice) are areas of grounded ice where ice flow results from deformation. In addition, basal sliding might occur in areas where the base is at the pressure melting point. Here, the SIA applies, which is subject to certain restrictions: The assumptions made in the SIA are valid everywhere except in the immediate vicinity of ice domes and along the margins. Furthermore, the topography has to be sufficiently smooth and the aspect ratio has to be small (Greve and Blatter 2009, Kirchner 2011).
2. Ice streams are regions of fast-flowing ice. In reality, ice streams are glaciological features with widths of a few kilometers, much smaller than our grid size (20 to 40 km). In GRISLI, the effect of these features is parameterized by treating areas that have the large scale-characteristics of ice streams differently, i.e. narrow valleys, thick sediment layers saturated by meltwater, and areas with low effective basal pressure. In these areas we apply the SSA, a different set of momentum equations than for the slow-flowing ice sheet, following the approach by MacAyeal (1989).
3. Ice shelves are large floating ice plates in contrast to ice sheets and streams which are grounded, and are fed by inland ice. The line where ice begins to float is called the grounding line. Ice shelf nodes must satisfy a flotation criterion, and velocities in these grid points are computed from the same set of equations as the velocities in ice stream nodes but assuming a zero basal drag.

#### 4.1.2 Fundamental equations

The governing equations of ice sheet dynamics are based on the conservation of mass, momentum and energy:

$$\frac{\partial \rho}{\partial t} + \nabla \cdot (\rho \mathbf{u}) = 0, \quad (4-1)$$

$$\rho \frac{d\mathbf{u}}{dt} = \nabla \cdot \boldsymbol{\tau} + \rho \mathbf{g}, \quad (4-2)$$

$$\rho c \left( \frac{\partial T}{\partial t} + \mathbf{u} \cdot \nabla T \right) = \nabla \cdot (\kappa \nabla T) + Q_i, \quad (4-3)$$

Where the first term in Equation 4-1 is the partial time derivative.  $\rho$  stands for the ice density,  $\mathbf{u}$  for the ice velocity,  $\boldsymbol{\tau}$  for the stress tensor,  $\mathbf{g}$  for the gravitational acceleration,  $c$  for the heat capacity of ice,  $T$  for the ice temperature,  $\kappa$  for the thermal conductivity of ice, and  $Q_i$  for the deformational heat.

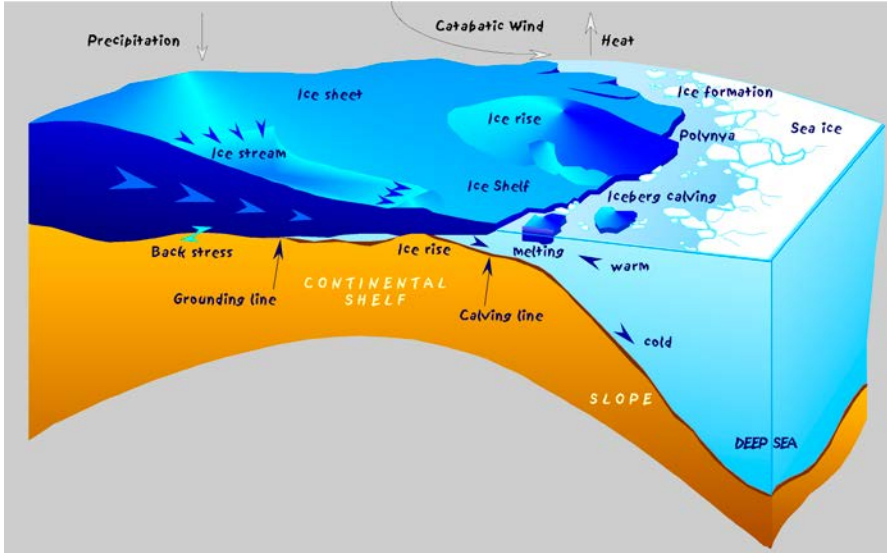


**Figure 4-1.** Sketch illustrating the different regions considered in GRISLI: ice sheets, ice streams and ice shelves. Figure from H. Grobe, AWI ([http://en.wikipedia.org/wiki/Ice\\_shelf](http://en.wikipedia.org/wiki/Ice_shelf)).

If we consider ice as an incompressible fluid with a constant density, the continuity Equation 4-1 simplifies to

$$\nabla \cdot \mathbf{u} = \frac{\partial u}{\partial x} + \frac{\partial v}{\partial y} + \frac{\partial w}{\partial z} = 0. \quad (4-4)$$

This equation is used to separate the vertical velocity from horizontal velocities (the computation of the horizontal velocity will be described later on).

The vertical integration of Equation 4-1 from the base of the ice sheet  $B$  to the surface elevation  $S$  leads to an equation for the ice thickness. Defining the ice thickness  $H$  as surface elevation minus the base of the ice sheet ( $S - B$ ), assuming that the ice density is constant and accounting for ablation and accumulation (Surface Mass Balance,  $SMB$ ) at the ice surface as well as melting at the ice base ( $F$ ) leads to:

$$\frac{\partial H}{\partial t} + \frac{\partial(Hu)}{\partial x} + \frac{\partial(Hv)}{\partial y} = SMB - F \quad (4-5)$$

The fundamental contributions that govern the mass balance of the ice sheet are:

1. The surface mass balance  $SMB$  (accumulation minus ablation) which depends on climatic conditions (surface air temperature and precipitation).
2. The basal melting rate  $F$ , which depends on the pressure melting point below the ice sheet and the geothermal heat flux. Below ice shelves, basal melting results from oceanic heat flux, and is denoted by  $b_{melt}$ .
3. Calving of the ice shelf, which depends on a thickness criterion.

Velocities within the ice sheet are rather small, and thus acceleration can be ignored: Assuming typical values for an ice sheet geometry and typical flow velocities, the ratio between acceleration and horizontal pressure gradient is  $\sim 10^{-15}$ , see Greve and Blatter (2009). Thus, the left hand side of Equation 4-2 is set to zero (Stokes assumption), and can thus be written as:

$$\frac{\partial \tau_{xx}}{\partial x} + \frac{\partial \tau_{xy}}{\partial y} + \frac{\partial \tau_{xz}}{\partial z} = 0, \quad (4-6)$$

$$\frac{\partial \tau_{yx}}{\partial x} + \frac{\partial \tau_{yy}}{\partial y} + \frac{\partial \tau_{yz}}{\partial z} = 0, \quad (4-7)$$

$$\frac{\partial \tau_{zx}}{\partial x} + \frac{\partial \tau_{zy}}{\partial y} + \frac{\partial \tau_{zz}}{\partial z} = \rho \mathbf{g}. \quad (4-8)$$

### 4.1.3 Equation of motion: grounded ice

In this section, we derive a simplified system of equations for the large-scale ice-sheet dynamics. We split up the stress tensor into a deviatoric part  $\tau'$  and an isotropic pressure:

$$\begin{aligned}\tau_{ij} &= \tau'_{ij} - \frac{1}{3}(\tau_{xx} + \tau_{yy} + \tau_{zz}) \delta_{ij} \\ &= \tau'_{ij} - p.\end{aligned}$$

We assume that the shear stresses  $\tau_{xz}$  and  $\tau_{yz}$  are small compared with the vertical normal stress  $\tau_{zz}$ . This reduces the vertical momentum equation to a balance between the vertical gradient of  $\tau_{zz}$  and the gravity force (hydrostatic approximation). Integration gives the hydrostatic pressure equation:

$$p = \rho g (H-z). \quad (4-9)$$

In GRISLI, like in other large-scale ice-sheet models, the shallow-ice approximation (SIA, Hutter 1983) is used. The SIA is a simplification that is reasonable when the horizontal length scale is much larger than the ice thickness. We assume that the flow regime is mainly characterized by bed-parallel shear. Thus the relevant components of the deviatoric stress tensor are the shear stresses in the horizontal plane,  $\tau_{xz}$  and  $\tau_{yz}$ . Then the horizontal components of the momentum balance simplify to:

$$\frac{\partial \tau_{xz}}{\partial z} = \frac{\partial p}{\partial x} = \rho g \frac{\partial H}{\partial x} \quad (4-10)$$

$$\frac{\partial \tau_{yz}}{\partial z} = \frac{\partial p}{\partial y} = \rho g \frac{\partial H}{\partial y} \quad (4-11)$$

The deviatoric stress  $\tau_{xy}$  is related to the strain rate  $\epsilon'_{xy}$  by a nonlinear Glen-type flow law (an equivalent expression holds for  $\tau_{yz}$  and  $\epsilon'_{yz}$ ):

$$\dot{\epsilon}_{xy} = \frac{1}{2} \left( \frac{\partial u}{\partial z} + \frac{\partial w}{\partial x} \right) = B_{AT} (T_{pmp}) \tau_*^{n-1} \tau_{xy}, \quad (4-12)$$

where  $B_{AT}$  is the temperature dependent flow law coefficient,  $n$  is the flow law exponent (here we use  $n=3$ ).  $\tau_*$  is the effective shear stress given by

$$\tau_* = \sqrt{\tau_{xz}^2 + \tau_{yz}^2}. \quad (4-13)$$

The ice temperature  $T_{pmp}$  is the absolute temperature corrected for the dependence on the melting point on pressure:

$$T_{pmp} = T + 9.76 \cdot 10^{-8} \rho g (S-z). \quad (4-14)$$

The flow law coefficient  $B_{AT}$  follows an Arrhenius relationship:

$$B_{AT} = B_{AT0} \exp \left( \frac{E_a}{R} \left( \frac{1}{T_{pmp}} - \frac{1}{T} \right) \right), \quad (4-15)$$

where  $B_{AT0}$  is a coefficient,  $E_a$  is the activation energy and  $R$  the universal gas constant. Combining the above equations and integrating over  $z$  gives an equation for the horizontal velocity  $\mathbf{u}$ :

$$\mathbf{u} = -(\rho g)^n (\nabla S \cdot \nabla S)^{\frac{n-1}{2}} \nabla S E_f \int_B^z B_{AT} (T_{pmp}) (S - z')^n dz' + \mathbf{u}_B, \quad (4-16)$$

$E_f$  is a parameter, the flow enhancement factor, set to 3 in this model version. We assume that sliding of ice over the bedrock occurs only if the basal ice temperature reaches the melting point. The basal velocity  $\mathbf{u}_B$  is expressed as a function of pressure resulting from the weight of the ice, surface slope and effective pressure  $N$ , following Weertman (1957):

$$\mathbf{u}_B = k (\rho g H)^3 (\nabla S \cdot \nabla S)^{\frac{1}{2}} \nabla S N^{-1}, \quad (4-17)$$

where  $k$  is an adjustable parameter, set to  $5 \cdot 10^{-11}$  in this version of GRISLI. The effective pressure  $N$  is given by

$$N = \rho g H - P_w, \quad (4-18)$$

where  $P_w$  is the sub-glacial water pressure. Again, Equation 4-17 is only valid for regions where the basal ice temperature reaches the melting point. If the basal ice temperature is below the melting point, the basal velocity is set to zero. In GRISLI, the sliding law described above is only valid for small velocities ( $< 50$  m/yr). Regions with larger velocities are considered as “fast flowing areas” and treated separately (see next section).

#### 4.1.4 Equation of motion: fast flowing areas

Ice streams and ice shelves are characterized by fast flow and low surface slopes. The sliding velocity Equation 4-17 depends strongly on the surface slope, and thus fast flowing areas would not be represented well in the model. For that reason, we treat ice stream and ice shelf areas separately in the model by applying the Shallow Shelf Approximation (SSA, MacAyeal 1989). Those regions are called “fast flowing areas”. Due to the fact that we use a horizontal resolution of 20 km and 40 km in our model setup, GRISLI cannot resolve individual ice streams. Thus, a grid point in GRISLI is considered as “ice stream grid point” if it has the large-scale characteristics of an ice stream area.

With the SSA, the horizontal velocity is independent of depth, which is reasonable for ice shelves and fast flowing ice stream areas. This leads to the following elliptic equation for horizontal vertically averaged velocity  $\bar{u}$ :

$$\frac{\partial}{\partial x} \left[ 2\bar{\eta}H \left( 2\frac{\partial u}{\partial x} + \frac{\partial v}{\partial x} \right) \right] + \frac{\partial}{\partial y} \left[ \bar{\eta}H \left( 2\frac{\partial u}{\partial y} + \frac{\partial v}{\partial x} \right) \right] = \rho g H \frac{\partial S}{\partial x} - \tau_{bx}, \quad (4-19)$$

$$\frac{\partial}{\partial y} \left[ 2\bar{\eta}H \left( 2\frac{\partial v}{\partial y} + \frac{\partial u}{\partial x} \right) \right] + \frac{\partial}{\partial x} \left[ \bar{\eta}H \left( 2\frac{\partial v}{\partial x} + \frac{\partial u}{\partial y} \right) \right] = \rho g H \frac{\partial S}{\partial y} - \tau_{by}. \quad (4-20)$$

where  $\bar{\eta}$  is the ice viscosity, vertically averaged over the ice thickness.  $\tau_{bx}$  and  $\tau_{by}$  stand for the basal drag. This set of equations is used both for ice stream areas and ice shelves.

#### Ice shelves

In case of ice shelves, the basal drag  $\tau_b$  is set to zero (since ice shelves are floating on the water without any resistance). In every time step, the position of ice shelves is determined with a flotation criterion, which is based on Archimedes’ principle of floating bodies:

$$\rho H = \rho_w (Sl - B) \quad (4-21)$$

where  $\rho$  and  $\rho_w$  are the ice and water density, respectively.  $Sl$  and  $B$  stand for sea level and the base of the ice sheet, respectively.

Calving of the ice shelf is determined by a thickness criterion. As soon as the ice thickness in an ice shelf node at the front reaches a certain threshold  $H_{calv}$ , the node is “cut off”. We set  $H_{calv}$  to 200 m, which corresponds to values observed at the large ice shelves of Antarctica. The oceanic basal melting rate below the ice shelf,  $b_{melt}$ , is determined by the temperature of the ocean. In this version of GRISLI we use a simplified approach assuming a melting rate which only depends on the water depth. Above 450 m,  $b_{melt}$  is set to 0.2 m/yr, while below 450 m depth  $b_{melt}$  is set to 2.45 m/yr. Peyaud et al. (2007), simulating the Early Weichselian Eurasian ice sheet, used a similar threshold of 450 m. The Late Saalian Eurasian ice sheet from Peyaud (2006) does not have any ice shelves, even over the Arctic region. In Section 5.3 we will show that the ice shelf area in our simulations is very small, restricted to a few grid points located between northern Norway and the area north of Severnaya Zemlya. Thus, the choice of the calving threshold  $H_{calv}$  and the basal melting rate  $b_{melt}$  might not lead to significant changes in the ice sheet.

#### Ice streams

In case of ice streams, the basal drag in Equations 4-19 and 4-20 is described by a friction law. It depends on the vertically averaged velocity  $\bar{u}$  and the effective pressure  $N$  Equation 4-18, scaled with the basal drag coefficient  $c_f$ :

$$\tau_b = c_f N \bar{u}. \quad (4-22)$$

The position of the “ice stream grid points” is determined with the following three criteria, from which at least one has to be fulfilled:

- The grid point is located in a narrow valley.
- First, the sediment layer has to be thick ( $h_{sed} > 150$  m). However, this threshold is ad-hoc and no direct evidence exists to constrain it better (see Discussion). Second, it has to be saturated by meltwater. This saturation is determined by the hydraulic head  $h_w$ , which has to exceed 250 m (the hydraulic head is calculated with a Darcy flow law, see Section 5.1.5). Third, the effective pressure  $N$  has to be lower than  $3.5 \cdot 10^7$  Pa.
- The grid point is located on an ice rise with low ice thickness and low surface slope. It has to hold that:  $\rho g H \nabla S \leq 7 \cdot 10^6$  Pa.

As boundary condition, GRISLI uses a global map of sediment thickness from Laske and Masters (1997) at  $1^\circ \times 1^\circ$  resolution (Figure 4-2a). Over Scandinavia, the sediment thickness is very thin compared with surrounding regions. The maximum sediment thickness occurs in the Barents and Kara Seas, where the thickness reaches up to 12 km. The large sediment thickness in this area and south of Scandinavia will influence the dynamics of the Eurasian ice sheet. Additionally, a high resolution data set of sediment thickness covering Sweden from Swedish Geological Survey (SGS) merged with the Laske and Masters (1997) data set was used in some experiments (Figure 4-2b). The SGS data set has a resolution of 4 km in zonal direction and 8 km in meridional direction, and is linearly interpolated onto the GRISLI grid.

#### 4.1.5 Basal hydrology

One criterion for determining the position of ice streams is the basal water head  $h_w$ . In the following, we describe how basal hydrology is implemented in GRISLI.

The basal hydrology is characterized by different hydrological features, ranging from drainage through a thin film of water ( $< 1$  mm) to flow through a network of cavities and rivers. Also percolation of basal water into the porous sub-glacial sediment plays an important role. Nonetheless, due to a lack of observations we still do not fully understand the hydrological processes occurring below ice sheets. Thus, the representation of basal hydrology in an ice-sheet model is one of the most arguable components, but indeed one of the most important processes for the dynamics of the whole ice sheet.

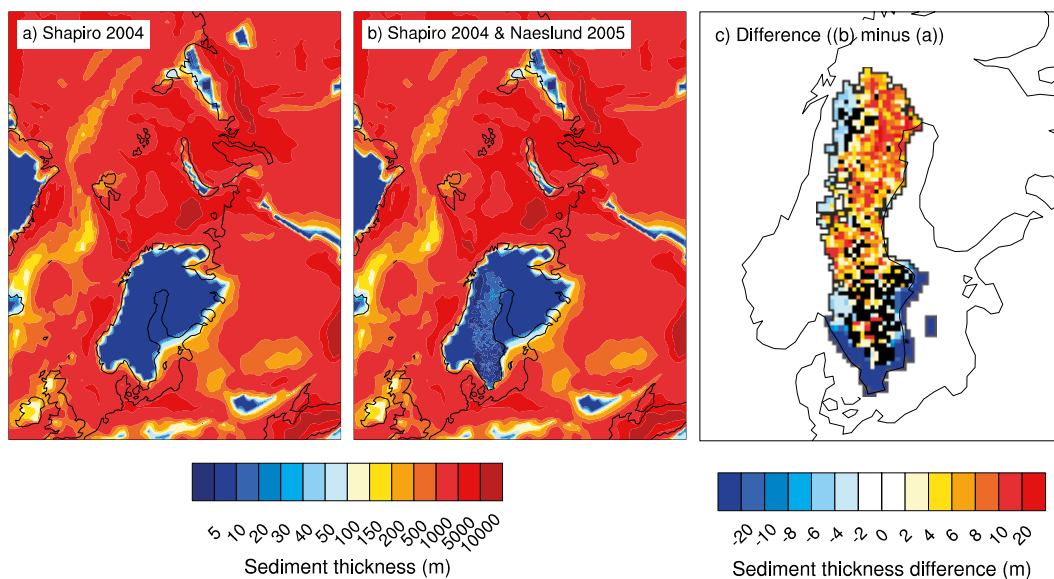


**Figure 4-2.** (a) Map of sediment thickness from Laske and Masters (1997), (b) combined sediment thickness from Laske and Masters (1997) and high-resolution SGS data set and (c) difference between the combined data set and Laske and Masters (1997) zoomed over Scandinavia. Data sets were interpolated on the Eurasian 20 km GRISLI grid.

The basal hydrology in GRISLI was implemented by Peyaud (2006), and is based on a Darcy-type flow law. The drainage of sub-glacial water depends on the pressure imposed onto the base. This pressure can be expressed as a potential, and the flow of meltwater follows its gradient. The potential can be written as:

$$\Phi = p_w + \rho_{fw}gB + \rho gH + \Phi_0. \quad (4-23)$$

$p_w$  stands for the sub-glacial water pressure. The second term represents the influence of the altitude of the base, while the third term represents the pressure resulting from the weight of the ice.  $\Phi_0$  is an arbitrary constant. Then, the gradient of  $\Phi$  can be expressed as

$$\nabla\Phi = \nabla p_w + \nabla(\rho_{fw}gB + \rho gH) = \nabla p_w + \rho g \left[ \left( \frac{\rho_{fw}}{\rho} - 1 \right) \nabla B + \nabla S \right]. \quad (4-24)$$

Note that the magnitude of the surface gradient  $\nabla S$  is around 10 times larger than that of the bedrock. Darcy's law states that flow through a porous medium is proportional to a hydraulic gradient, which corresponds to the variation of the hydraulic head,  $h_w$ . This leads to an equation for the flow velocity, and with expressing the hydraulic head as  $h_w = \Phi/\rho_{fw}g$  we obtain

$$V_e = -K \nabla h_w = -\frac{K}{\rho_{fw}g} \nabla\Phi, \quad (4-25)$$

with the proportionality constant  $K$  (the hydraulic conductivity). This parameter depends on the property of the soil (e.g. clay:  $<10^{-9}$  m/s, till:  $10^{-12}$  to  $10^{-5}$  m/s, fine sand:  $10^{-7}$  to  $10^{-5}$  m/s). In GRISLI,  $K$  is set in the following way: If the base is cold (with the ice temperature below the pressure melting point), we make the assumption that the ground is impermeable and thus  $K$  is set to zero. If the base is warm (with the ice temperature above the pressure melting point) and the effective pressure is high, we choose a constant value of  $K_0 = 10^{-6}$  m/s. If the effective pressure is low, the hydraulic conductivity increases:

$$K = \begin{cases} K_0 & \text{if } N > 1000 \text{ bar} \\ K_0 \cdot \frac{1000}{N} & \text{if } N \leq 1000 \text{ bar} \end{cases} \quad (4-26)$$

#### 4.1.6 Ice temperature

The ice temperature is required to calculate the flow law coefficient  $B_{AT}$ , the basal melting rate  $F$  below the grounded regions, and the basal ice velocity  $u_b$ , since sliding occurs only in areas where the basal ice temperature is at the melting point. The time-dependent heat Equation 4-3 is solved in the ice sheet, and accounts for horizontal and vertical advection of ice, vertical diffusion and production of heat through deformation.

At the surface, the ice temperature is determined by climatic conditions (which also depend on surface elevation). The ice temperature 10 m below the ice surface is almost the same as the annual mean surface air temperature  $T_{ann}$ . Thus we use  $T_{ann}$  as a surface boundary condition for ice temperature. At the base of the ice sheet, a geothermal heat flux (GHF) is prescribed. In this model setup, we use a map of geothermal heat flux reconstructed by Shapiro and Ritzwoller (2004) (Figure 4-3a). Over Sweden and Finland, GHF ranges from 41.9 to 60.5 mW/m<sup>2</sup>, with a mean value of 49.5 mW/m<sup>2</sup>. Additionally, a high-resolution data set covering Sweden and Finland from Näslund et al. (2005) is used in some experiments (Figure 4-3b). This data set has a resolution of 5 km, and is linearly interpolated onto the GRISLI grids.

At the ice-bedrock interface we distinguish between warm and cold conditions: Below the melting point, the heat flux at the interface consists of geothermal heat, which is transmitted by vertical diffusion into the ice. At the melting point, the melting rate depends on the difference between the heat fluxes on both sides, including heat generated by friction during the sliding. If basal temperature  $T_b$  is at the melting point, it is held constant:

$$T_b = T_{pmp} \quad \text{if } T_b \geq T_{pmp}; \quad (4-27)$$

and the excess in heat is used for basal melting  $F$ . This basal melting rate  $F$  is one of the components of the vertically integrated mass balance equation (Equation 4-5).

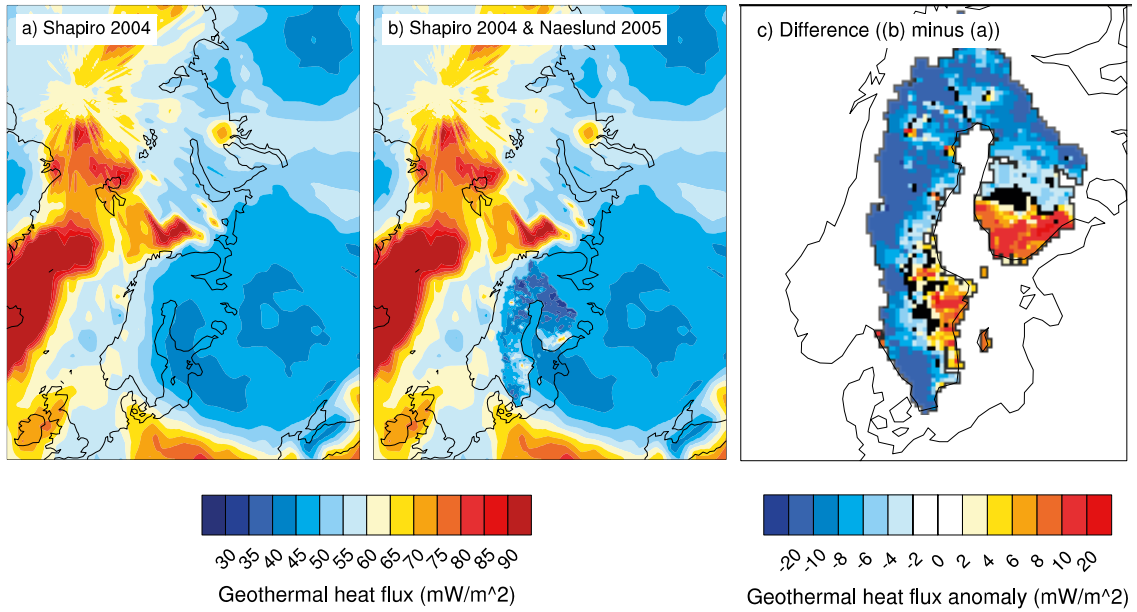


**Figure 4-3.** (a) Map of geothermal heat flux ( $mW/m^2$ ) from Shapiro and Ritzwoller (2004), (b) combined GHF from Shapiro and Ritzwoller (2004) and Näslund et al. (2005) and (c) difference between the combined data set and Shapiro and Ritzwoller (2004) zoomed over Scandinavia. Data sets were interpolated on the Eurasian 20 km GRISLI grid.

#### 4.1.7 Surface mass balance

The surface mass balance (SMB) in the ice-sheet model is composed of accumulation and ablation:

##### **SMB = Accumulation – Ablation**

The accumulation corresponds to the mean annual total precipitation obtained from CESM, which is turned into snow using a density of  $917 \text{ kg/m}^3$ . In GRISLI, ablation is parameterized using the Positive-Degree-Day (PDD) semi-empirical method (Reeh 1991). This method is based on an empirical relationship between the number of positive degree days, computed from annual mean and July surface air temperature, and the snow and ice melting rates which depend on the melting factors  $C_{snow}$  and  $C_{ice}$ , derived from observations. The number of positive degree days (PDD) is given by:

$$PDD = \frac{1}{\sigma\sqrt{2\pi}} \int_{1yr} \int_0^\infty \exp\left(\frac{-(T - T_d)^2}{2\sigma^2}\right) dT dt \quad (4-28)$$

where  $T_d$  is the daily temperature and  $\sigma$  the standard deviation of the daily temperature, usually set to  $5^\circ\text{C}$ . This formulation allows for positive temperatures even when the average daily temperature is below the melting point. As a consequence, it may also overestimate melting in general (Bougamont et al. 2007). The daily temperature  $T_d$  is reconstructed from annual mean and July temperatures,  $T_{Ann}$  and  $T_{July}$ , by assuming that the annual temperature cycle follows a cosine function:

$$T_d(t) = T_{Ann} + (T_{July} - T_{Ann}) \cos(2\pi t/365). \quad (4-29)$$

Ablation is then calculated in several steps:

1. Snow, if it is present, is melted at rate  $C_{snow}$ . Meltwater is supposed to percolate into the snow layer and refreezes as superimposed ice. Runoff occurs when the amount of superimposed ice exceeds 60% of the yearly snowfall.
2. Superimposed ice is melted at rate  $C_{ice}$ .
3. Glacier ice is melted.

Depending on the available energy, not all steps or even none of the steps will be carried out. The melting factors  $C_{snow}$  and  $C_{ice}$  are typically set to 3 and  $8 \text{ mm d}^{-1} \text{ }^\circ\text{C}^{-1}$ .  $C_{ice}$  and  $C_{snow}$  take different values to account for the difference in albedo between snow and ice. The portion of melted water that can refreeze, denoted by  $csi$ , is set to 60% in GRISLI, but can reach values up to 70% (Pfeffer et al. 1991).

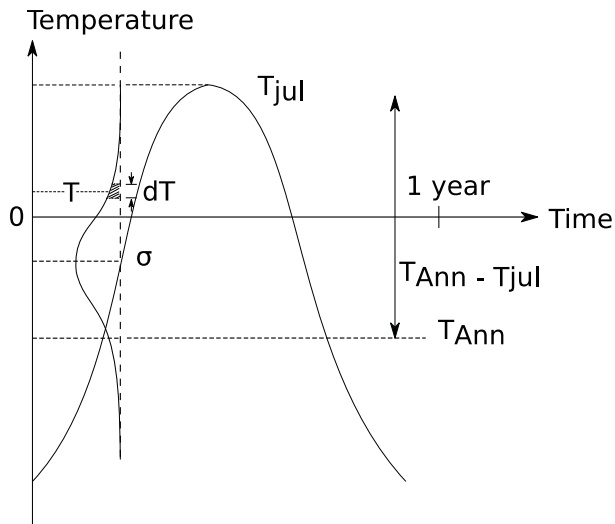


**Figure 4-4.** Reconstructed annual temperature cycle used to calculate the number of positive degree days. The annual cycle is retrieved from the annual mean temperature and the July temperature. Figure modified from Reeh (1991).

#### 4.1.8 Isostasy

The bedrock reacts to changes in surface load and the process is called “isostasy” (Figure 4-5). In GRISLI, this isostatic response to ice surface load is described by the ELRA (elastic lithosphere-relaxed asthenosphere) method (Le Meur and Huybrechts 1996). The lithosphere is treated as a thin elastic plate. This allows a regional response to the ice load, so that the bedrock at some distance from the imposed ice load can still be affected (in contrast to the rather simple “local lithosphere”-method which accounts only for a local response). The underlying asthenosphere is assumed to be viscous. Due to its viscous property the asthenosphere responds to an imposed ice load with a time lag, namely characteristic relaxation time  $\tau_r$ . In GRISLI the default value of this parameter is 3,000 years (Turcotte and Schubert 2002).

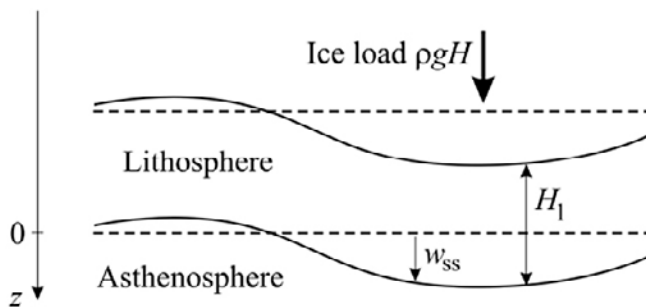


**Figure 4-5.** Sketch of the ELRA-method. Figure from Greve and Blatter (2009).  $H_1$  corresponds to the lithosphere thickness while  $W_{ss}$  corresponds to the amplitude of the isostatic depression.

## 4.2 Model setup

### 4.2.1 Horizontal Grid

The ice-sheet simulations were run on a 20 km regular rectangular grid covering the Eurasian domain (grid ID: Eu20). The grid is projected using the Lambert Equal Area geographical projection (center of projection: 0°; 90°N) and coordinates are expressed in native Cartesian distances (km). The grid has 210 points in the X direction and 270 points in the Y direction. In order to investigate the effect of the spatial resolution on the ice-sheet simulations, the simulations have also been performed on a 40 km resolution grid covering the Northern hemisphere down to ~37°N (grid ID: NH40). This coarser grid consists of 241 points in each of the X and Y directions. In the vertical, both grids have 21 levels evenly spaced along the z-axis, scaled to the ice thickness. Furthermore, there are 4 levels in the bedrock layer. Finally, the equations governing ice flow, ice thickness and ice temperature evolution are discretized with the finite difference method.

### 4.2.2 Initial conditions and climate forcing

GRISLI needs three initial conditions, namely surface topography, bed topography, i.e. topography below the existing ice sheets, and ice thickness if some ice sheets already exist in the initial topography. Over ice-free regions, bed topography equals surface topography, whereas over ice-covered regions, ice thickness equals surface topography minus bed topography. Thus, the three initial conditions are not independent from each other. In our experiments, we use two different sets of initial conditions. The first one, Topo1, is the reconstructed Late Saalian ice sheet distribution (Figure 4-6, after Colleoni 2009) composed of the Late Saalian Eurasian ice sheet from Peyaud (2006) and of the Last Glacial Maximum Laurentide ice sheet from ICE-5G (Peltier 2004). The second set of initial conditions is composed of a smaller North American ice sheet from Peltier (2004) and the Late Saalian Eurasian ice sheet from Peyaud (2006) (see Colleoni 2009 for a description of Topo2 initial conditions).

The ice-sheet model is forced by the simulated steady-state annual mean and July surface air temperatures and mean annual total precipitation from the B140\_Topo1 and B140\_Topo2 climate simulations. Those simulations use initial, boundary and forcing conditions representative for the MIS 6 glacial maximum ~140 kyrs BP (i.e. orbital parameters, greenhouse gases, Late Saalian topography from Colleoni 2009). Climate simulations B140\_Topo1 and B140\_Topo2 differ in the prescribed North American ice sheet topography, using those in Topo1 and Topo2, respectively (Figure 4-6). Figure 4-7 depicts the surface air temperature and precipitation input fields from both climate simulations, and their difference, interpolated and downscaled onto the Eurasian 20 km GRISLI grid.

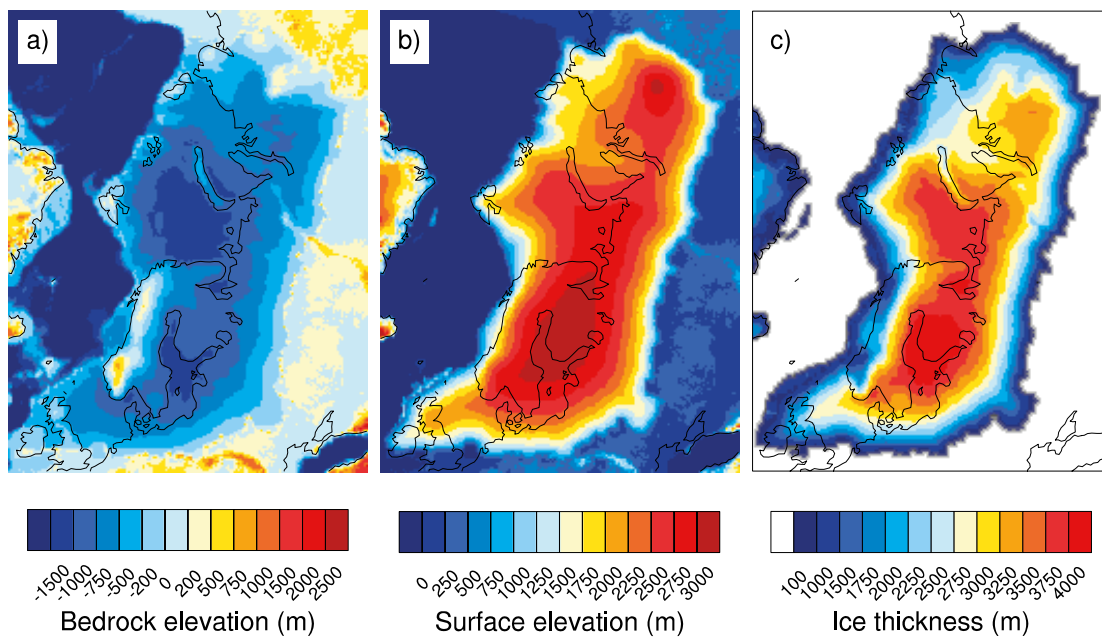


**Figure 4-6.** Reconstructed Late Saalian bedrock elevation (a), surface elevation (b) and ice thickness (c) according to Peyaud (2006) used as initial condition for our simulations, interpolated on the Eurasian 20 km GRISLI grid.

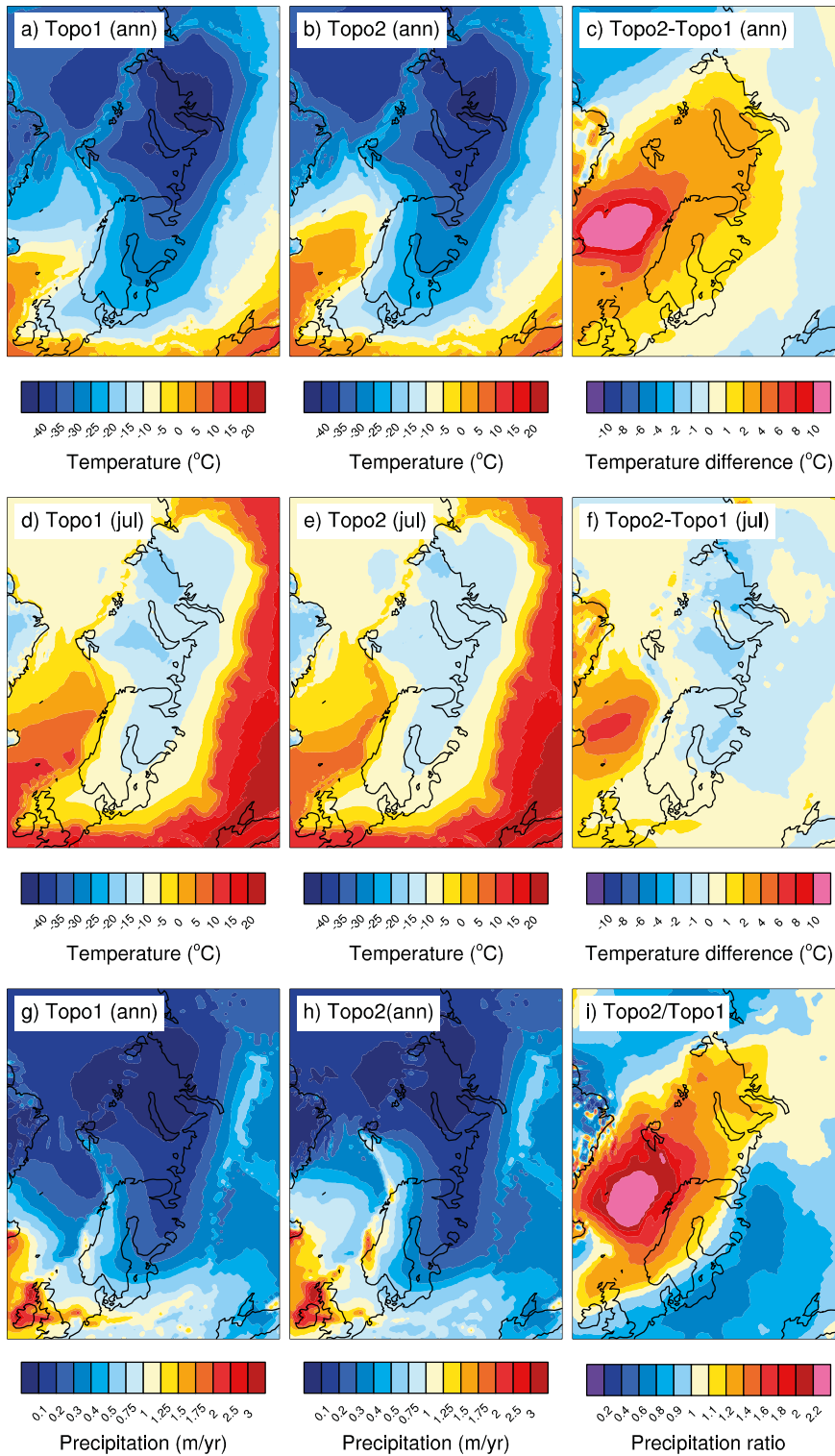


**Figure 4-7.** Annual mean (top) and July (middle) surface air temperature and annual mean total precipitation (bottom) averaged over the last 50 years of the CESM climate simulations, interpolated and downscaled on the Eurasian 20 km ISM grid. The left and middle panels show fields for B140\_Topo1 and B140\_Topo2, respectively. The right panel shows the difference (for temperature) and ratio (for precipitation) between the two simulations.

### **Downscaling procedure**

Since the Eurasian grid used in GRISLI has a horizontal resolution of 20 km and the CESM simulation was performed using a resolution of roughly  $1^\circ \times 1^\circ$ , a downscaling of the climate fields is necessary to account for the differences in elevation caused by the difference in resolution between the two models. Preparation of the climatic input fields for GRISLI therefore comprised the following steps.

1. The temperature field from the CESM simulation was horizontally interpolated on the higher resolution Eurasian ice-sheet model (ISM) grid:

$$T_{CESM}(1^\circ \times 1^\circ) \rightarrow T_{ISM}(20 \text{ km} \times 20 \text{ km}). \quad (4-30)$$

2. Interpolation of the surface elevation field from the coarse resolution CESM grid onto the ice-sheet model grid introduces small differences in elevation. Temperature fields have to be corrected for these elevation changes by means of a lapse rate value (downscaling):

$$T_{ISM-cor} = T_{ISM} + \lambda (S_{CESM-on-ISM} - S_{ISM}): \quad (4-31)$$

where  $T_{ISM-cor}$  and  $T_{ISM}$  are the final downscaled temperature field and the interpolated temperature field, respectively.  $S_{ISM}$  denotes the high resolution topography of the ice-sheet model grid, and  $S_{CESM-on-ISM}$  is the CESM topography interpolated on the high-resolution ice-sheet model grid. The atmospheric lapse rate  $\lambda$  is derived from literature on LGM Eurasian ice-sheet modeling (Abe-Ouchi et al. 2007) and set to  $5^\circ\text{C}/\text{km}$  for annual temperatures and  $4^\circ\text{C}/\text{km}$  for July temperatures in our case.

### **Climate correction during runtime**

Changes in ice-sheet altitude lead to changes in the surface air temperature, and also to changes in precipitation, as colder air leads to increased aridity: with increasing altitude, temperatures cool and precipitation decreases. In GRISLI, temperatures account for elevation changes at each time step, by means of a lapse rate value:

$$T_{cor}(t) = T_0 + \lambda (S(t) - S_0), \quad (4-32)$$

where  $T_{cor}$  and  $T_0$  are the corrected and initial temperature fields, respectively,  $S$  is the elevation at time step  $t$ , and  $S_0$  is the initial elevation. The lapse rate  $\lambda$ , as described above, takes different values for annual mean and July temperatures. Additionally, precipitation is corrected for changes in elevation:

$$P_{cor}(t) = P_0 \cdot \exp(\gamma \cdot (T_{cor}(t) - T_0)) \quad (4-33)$$

where  $P_{cor}$  and  $P_0$  stand for the corrected and initial precipitation, respectively. The precipitation correction factor  $\gamma$  is set to  $0.05^\circ\text{C}^{-1}$ , but ranges from  $0.03^\circ\text{C}^{-1}$  to  $0.078^\circ\text{C}^{-1}$  in the literature (see for example, Charbit et al. 2002). Note that the use of an exponential function in the precipitation formulation (Equation 4-33) is motivated by the saturation pressure of water vapor in the atmosphere (Clausius-Clapeyron relationship), which increases roughly exponentially with temperature. This exponential function leads to an increase in precipitation if the temperature at time step  $t$ ,  $T_{cor}(t)$ , is higher than the initial temperature  $T_0$ . This is the case when the elevation at time step  $t$ ,  $S(t)$ , is lower than the initial elevation  $S_0$ . Conversely, if  $T_{cor}(t)$  is lower than  $T_0$ , which implies that  $S(t)$  is larger than  $S_0$ , precipitation is reduced.

## **4.3 Reference simulations**

In this section, we present the ice sheets simulated by GRISLI under steady-state B140\_Topo1 and B140\_Topo2 climate forcing. These simulations were run with a standard set of parameters (see Table 4-1), and serve as “reference simulations”. The sensitivity experiments described later on are branched from these reference simulations. The reference experiments with both climate forcings (denoted by REF\_Topo1 and REF\_Topo2) were carried out on the Eurasian grid with 20 km horizontal resolution, Eu20, and integrated for around 300 kyrs until steady state is reached. Initial conditions, surface topography, bedrock elevation and ice thickness from the Late Saalian reconstruction, were used for both experiments (Figure 4-6).

**Table 4-1. List of parameters used in the reference simulations REF\_Topo1 and REF\_Topo2.**

<b>Climate forcing</b>		
$\lambda_{Ann}$	5°C/km	Lapse rate for annual mean air temperature
$\lambda_{July}$	4°C/km	Lapse rate for July air temperature
$\gamma$	0.05°C <sup>-1</sup>	Precipitation correction factor
<b>PDD parameters</b>		
$C_{ice}$	3 mm/d/°C	Melting factor of ice
$C_{snow}$	8 mm/d/°C	Melting factor of snow
$\sigma$	5°C	Standard deviation of the daily air temperature
$CSI$	60%	Percentage of ice that refreezes
<b>Ice stream areas</b>		
$C_f$	2·10 <sup>-5</sup>	Basal drag coefficient
$h_{sed}^*$	150 m	Critical sediment thickness
$h_w^*$	250 m	Critical hydraulic head
$N^*$	3.5·10 <sup>7</sup> Pa	Critical effective pressure
<b>Ice shelf areas</b>		
$H_{calv}$	200 m	Critical thickness of ice shelves at the front
$b_{melt}$ (above / below 450 m)	0.2/2.45 m/yr	Melting rate below ice shelves
<b>Solid earth</b>		
$\tau_r$	3,000 yrs	Characteristic relaxation time

During runtime surface topography changes, and as a result, the climate fields (surface air temperature and total precipitation) have to be corrected for elevation changes as described in Section 4.2.2. For surface air temperature correction, lapse rates are set to 5°C/km and 4°C/km for annual means and July, respectively (Abe-Ouchi et al. 2007). The choice of the reference parameters listed in Table 4-1 is further discussed in the next section.

Table 4-2 lists the most important numbers related to the simulated Eurasian ice sheet geometry obtained at the end of the reference simulations. For convenience, ice volume is converted into meters sea level equivalent (m SLE), which is calculated as

$$h_{SLE} = \frac{\rho_{ice}}{\rho_w \cdot A_{oce}} V_{ice} \quad (4-34)$$

where  $A_{oce}$  is an estimate of the global ocean area (3.62·10<sup>6</sup> km<sup>2</sup>) and  $V_{ice}$  is the simulated ice sheet volume.  $\rho_{ice}$  is the ice density set to 917 kg/m<sup>3</sup> and  $\rho_w$  is the sea water density set to 1,028 kg/m<sup>3</sup>.

**Table 4-2. Geometric parameters of the simulated ice sheets of reference simulations REF\_Topo1 and REF\_Topo2 at the end of the integration: ice volume in meters sea level equivalent (m SLE), ice extent area (10<sup>6</sup> km<sup>2</sup>), ice thickness (m) and bedrock elevation (m). Numbers for the Late Saalian Eurasian ice sheet from Peyaud (2006) are given for comparison.**

	REF_Topo1	REF_Topo2	Initial topography
Eurasian ice volume (m SLE)	55	53	70
Eurasian ice extent area (10 <sup>6</sup> km <sup>2</sup> )	11.9	11.79	11.2
Ice thickness Forsmark (m)	3,196	2,969	4,247
Bedrock elevation Forsmark (m)	-752	-700	-983

The initial volume of the Eurasian ice sheet from Peyaud (2006) corresponds to  $\sim 70$  m SLE. The spin-up phase takes around 200 kyrs, by when the simulated ice sheet is in equilibrium with the imposed climate forcing (Figure 4-8a). At the end of the simulations, the Eurasian ice volume has decreased substantially to 55 and 53 m SLE for REF\_Topo1 and REF\_Topo2, respectively. This strong decrease, relative to the initial ice-sheet volume, is due to the fact that for the reconstruction of the Eurasian ice sheet, Peyaud (2006) used a climate forcing based on Early Weischelian cycle ( $\sim 90$  kyrs BP) climate forcing from Krinner et al. (2004), which he modified to match the Late Saalian extent from Svendsen et al. (2004). As a consequence, the large-scale circulation from Peyaud 's climate forcing and ours is different, leading to differences in precipitation pattern as explained in Section 3.3. In our climate simulations B140\_Topo1 and B140\_Topo2, the presence of two large ice sheets causes a large cooling and drying of the Northern high latitudes. When forcing GRISLI with these simulated cold and dry climate conditions, the overall Late Saalian Eurasian ice thickness decreases until it reaches a volume equilibrium lower than in the original reconstruction.

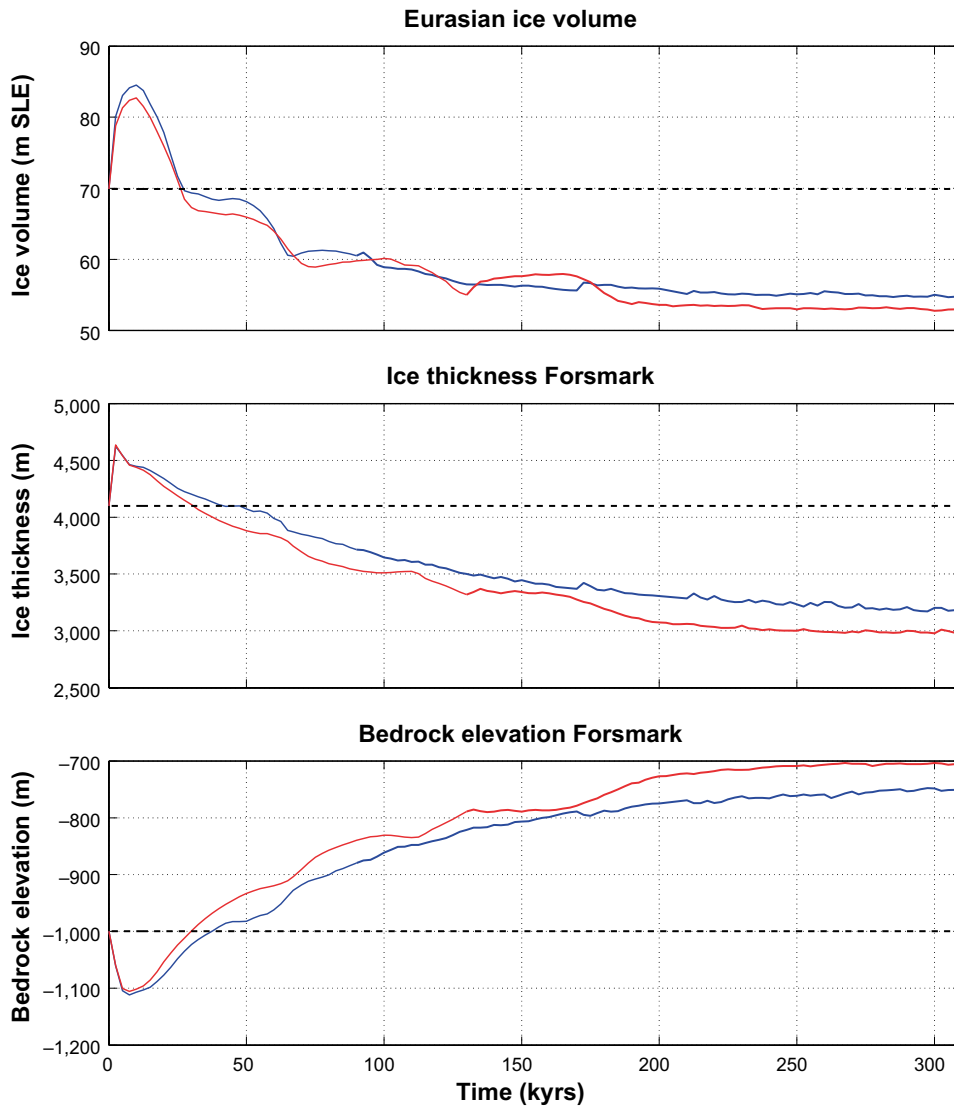


**Figure 4-8.** Time series of the simulated Eurasian ice-sheet volume (in m SLE, top panel), ice thickness over Forsmark (in m, middle panel) and bedrock elevation in Forsmark (in m, bottom panel) for reference simulations REF\_Topo1 (blue) and REF\_Topo2 (red). Dashed lines correspond to the original topography from Peyaud (2006).

The strong changes in simulated ice volume in the first 20 kyrs can be attributed to the initialization. When starting a simulation with prescribed ice thickness, the initial ice temperature is set to a constant value of 0°C. Thus, the vertical structure of ice temperature has to build up in the beginning of the simulation. It evolves as a result of diffusion, advection, deformational heat production and prescribed boundary conditions from the surface to the base (Equation 4-3). This equilibrating process takes about 20 kyrs (Figure 4-8). If we had initialized the model with a realistic vertical temperature profile, ice volume would have reached equilibrium much faster.

Forsmark is located under one of the main ice sheet domes. The initial ice thickness in this location is 4,250 m, and reduces by ~1,050 m in REF\_Topo1 and by ~1,280 m in REF\_Topo2 at the end of the simulations (Figure 4-8b). As a consequence, the bedrock is subject to an uplift of ~230 m (REF\_Topo1) and ~280 m (REF\_Topo2) as a result of glacial isostatic adjustment.

Figure 4-9 depicts the final simulated ice thickness for both experiments, and the difference relative to the initial ice thickness from Peyaud (2006). Regarding the difference to the initial topography, both experiments show a similar thickness pattern: In most areas, the ice sheet shrinks strongly, particularly in the south-west and in the Barents Sea. In contrast, the ice sheet gains mass over eastern Siberia. The extent of the ice sheet in experiments REF\_Topo1 and REF\_Topo2 does not exceed the ice margin limits of the initial state of the Eurasian ice sheet reconstruction by Peyaud (2006) and comparable to the QUEEN reconstruction by Svendsen et al. (2004), (magenta line in Figure 4-9a and 4-9b), except for the East Siberian shelf. This is due to the initial topography prescribed in the climate simulations B140\_Topo1 and B140\_Topo2, in which this area is emerged due to the imposed sea-level drop. As a consequence of the simulated cold climate, a perennial snow cover accumulates over this emerged area (Figure 3-7). In addition, the snow cover in this area is particularly thick, which further strengthens the snow-albedo feedback. Therefore these conditions are favorable to the growth of an ice sheet in GRISLI.

The final Eurasian ice volume of simulations REF\_Topo1 and REF\_Topo2 differs by 2 m SLE, whereas the difference in ice thickness at the Forsmark location is around 230 m. Under the B140\_Topo2 climate forcing, the ice sheet loses mass particularly in the south-west, as shown in Figure 4-10a. This is due to higher surface air temperature (Figures 4-7c and 4-7f) and to lower precipitation rates (Figure 4-7i) in climate forcing B140\_Topo2. At the end of the simulation, the difference in temperature and accumulation remains almost the same between the two experiments (Figures 4-10b, 4-10c and 4-10d). Ablation along the south-western margin is much stronger in simulation REF\_Topo2 than in REF\_Topo1 (Figure 4-10e). This is a result of the higher July air temperature of climate forcing B140\_Topo2, particularly along the south-western margin of the ice sheet (up to 2°C, Figure 4-7f). Note that in GRISLI, July surface air temperature is only required for the computation of ablation (for reconstructing the annual temperature cycle within the PDD method), while annual mean temperature is, additionally to the computation of ablation, needed as a surface boundary condition for vertical ice temperature. Similarly over the northern part of the ice sheet, annual mean surface air temperature is much higher in B140\_Topo2 than in B140\_Topo1. But in contrast to the southern part of the ice sheet, accumulation is much higher as well. These two effects partly compensate each other, resulting in slightly higher ice thickness over northern Scandinavia and slightly lower ice thickness over the eastern Barents Sea in the REF\_Topo2 simulation.

Figure 4-11 illustrates the different areas considered in GRISLI as simulated in the reference experiments. Half of the ice sheet is treated using the SIA and is considered as grounded (beige shading in Figure 4-11a and 4-11b). The other half is computed using the SSA (orange and red shading in Figure 4-11a and 4-11b). The south-western part of the ice sheet, except for Scandinavia, parts of the Siberian continental shelf and parts along the southern margin are considered as fast flow areas (orange shading in Figure 4-11a and 4-11b). This pattern is mostly coherent with the spatial distribution of sediment thickness (Figure 4-2). The area covered by ice shelves is very small in both reference simulations (red shading in Figure 4-11a and 4-11b). Ice shelves develop only north of Norway and north of Severnaya Zemlya.

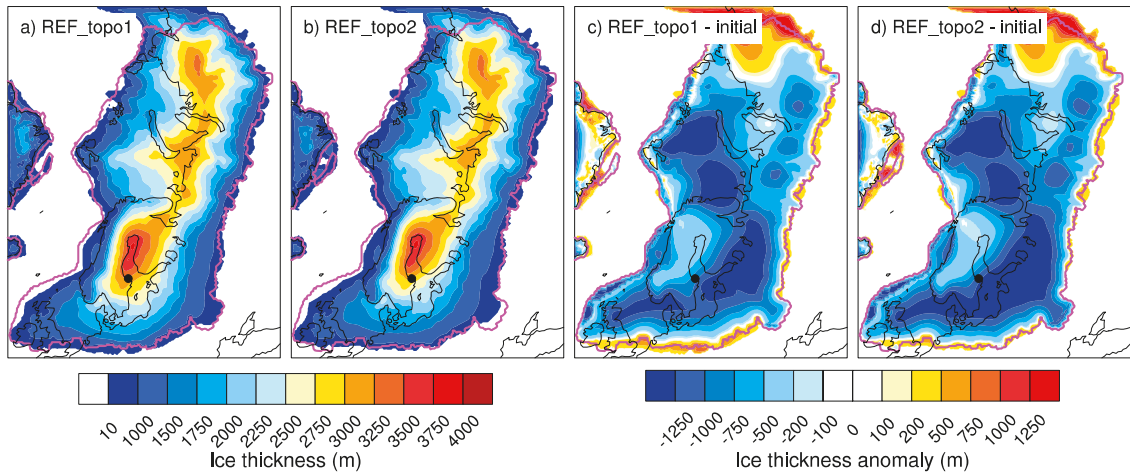


**Figure 4-9.** Simulated ice thickness for reference simulations *REF\_Topo1* (a) and *REF\_Topo2* (b), and difference between the initial ice thickness and simulations *REF\_Topo1* (c) and *REF\_Topo2* (d). The magenta line indicates the extent of the reconstructed Late Saalian ice sheet from Peyaud (2006).

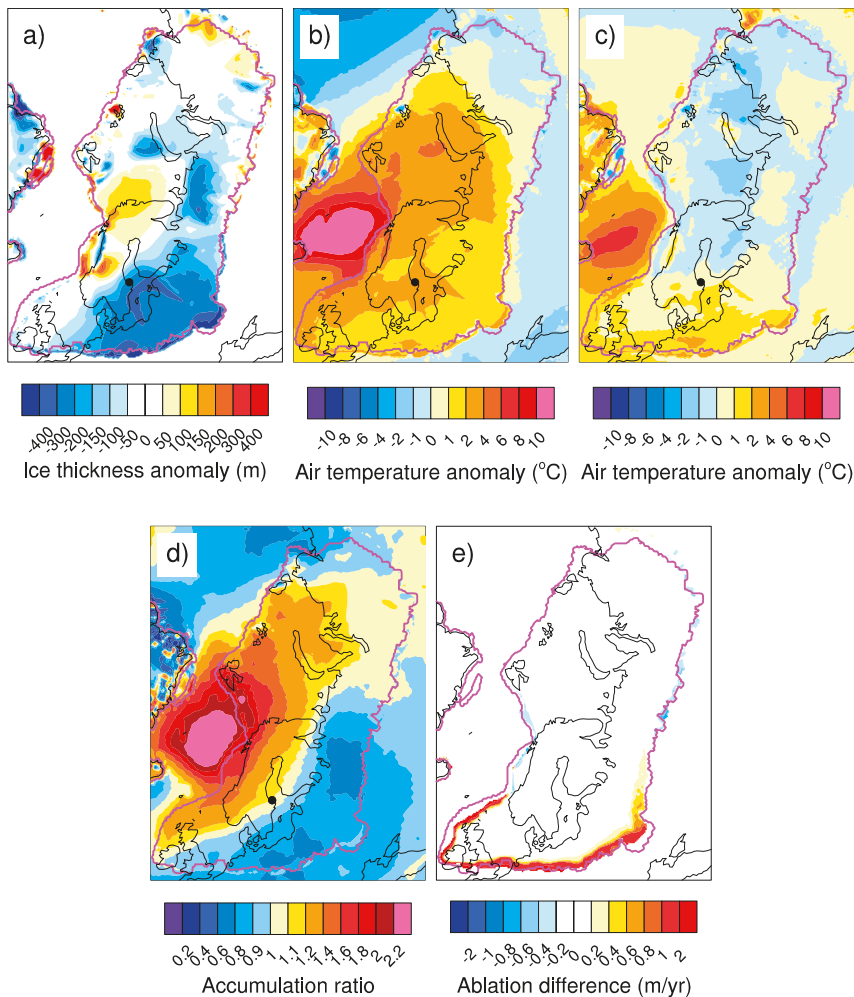


**Figure 4-10.** Difference in ice thickness (a), annual mean (b) and July (c) surface air temperature, ablation (e) and ratio of accumulation (d) between reference simulations *REF\_Topo1* and *REF\_Topo2* at the end of the integration (*REF\_Topo2* minus (or divided by) *REF\_Topo1*). The black dot indicates the Forsmark site, and the magenta line indicates the extent of the reconstructed Late Saalian ice sheet from Peyaud (2006).

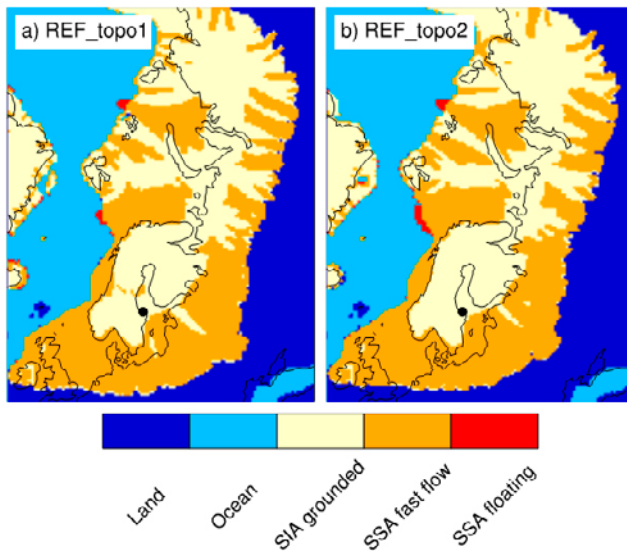


**Figure 4-11.** Map of the different regions considered in GRISLI in the reference experiments *REF\_Topo1* (a) and *REF\_Topo2* (b) at the end of the simulation: Land not covered by ice sheets (blue), ocean (light blue), grounded ice area where the SIA applies (beige), fast-flowing ice area where the SSA applies (orange) and ice shelves where the SSA applies (red). The black dot indicates the Forsmark site.

Figure 4-12 depicts the basal temperature of both reference experiments at the end of the simulation. Note that basal temperature is computed relative to the pressure melting point. The western part of the Eurasian ice sheet, parts of the Siberian continental shelf and parts along the southern margin are warm based, i.e. at the pressure melting point. Over the western part of the ice sheet, this is partly due to relatively warm surface air temperatures (Figure 4-7a and 4-7b), which, though diffusion, affect the base of the ice sheet, and partly due to high ice thickness (the main dome is located over Scandinavia) which increases the pressure at the base of the ice sheet. Particularly over the eastern part of the ice sheet we find a strong resemblance between the warm-based area and the ice-stream area (orange shading in Figure 4-11). This can be explained by heat input generated by friction during sliding, which increases the basal temperature. Therefore, topographic features such as the sediment thickness indirectly affect the basal temperature.

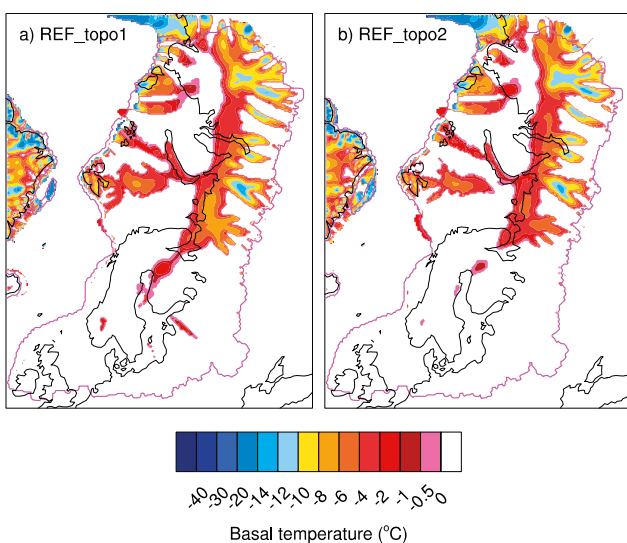


**Figure 4-12.** Simulated basal temperature relative to the pressure melting point of reference experiments *REF\_Topo1* (a) and *REF\_Topo2* (b) at the end of the simulation. The magenta line indicates the extent of the reconstructed Late Saalian ice sheet from Peyaud (2006).

Observations of basal conditions for the MIS 6 glacial maximum are not available, but, for the LGM, Kleman and Hättestrand (1999) deduced the distribution of frozen- and thawed-bed conditions from the occurrence of ribbed moraines in modern landscapes. Their study shows that large parts of northern Scandinavia must have been characterized by frozen-bed conditions at odd with what we obtain using our Late Saalian Eurasian ice sheet. But it has to be noted that the geometry of the Late Saalian ice sheet is very different from LGM Eurasian ice sheet reconstructions (Kleman et al. 2013, Peltier 2004). Over western Finland, the simulated basal temperature of REF\_Topo1 agrees with the LGM basal temperature reconstruction from Kleman and Hättestrand (1999), whereas the remaining parts of Scandinavia are warm-based in our simulation. Due to higher surface air temperatures in REF\_Topo2, basal conditions are even warmer in this simulation. Again, the geometry of the Late Saalian Eurasian ice sheet is different from LGM reconstructions, and then a direct match is not expected from a comparison.

#### 4.4 Sensitivity experiments: impact of model parameters

In this section, we investigate the impact of a parameter space on the simulated ice sheet geometry. The overall aim is to investigate uncertainties in the ice-sheet model reconstruction and to obtain an ensemble of ice-sheet geometries. This allows for a more reliable estimate of the MIS 6 Eurasian ice thickness, and, in particular, of the ice thickness over the Forsmark site. In this respect, we investigate the impact of physical parameters that are of importance for the mass balance of the ice sheet. The values that we explore in the sensitivity experiments are taken from the literature. All sensitivity experiments are listed in Table 4-3. In total, 70 experiments, including the reference simulations, were conducted on the Eurasian 20 km grid, using both climate forcing B140\_Topo1 and B140\_Topo2. All simulations were also carried out on the Northern Hemisphere 40 km grid.

To be sure that the outcome of the sensitivity tests results from the change of the parameters that we modified only, all experiments are branched from the reference simulation. Given Equation 4-5, the main processes that substantially modify the computation of ice thickness are linked with surface mass balance, basal melting and advection-diffusion. Therefore, our sensitivity tests are divided into five groups:

##### **A: Climate corrections**

- Lapse rates  $\lambda_{Ann}$  and  $\lambda_{July}$ .
- Precipitation correction factor  $\gamma$
- Accumulation: snow vs. total precipitation.

##### **B: Ablation (PDD parameters)**

- Melting rates for ice and snow  $C_{ice}$  and  $C_{snow}$
- Standard deviation of the daily temperature cycle  $\sigma$
- Refreezing rate of melted snow  $csi$ .

##### **C: Ice stream areas**

- Extent of the ice stream area: sediment thickness threshold
- Basal drag coefficient  $c_f$

##### **D: Ice shelves**

- Calving rate: thickness threshold at the front  $H_{calv}$
- Basal ocean melting rate  $b_{melt}$

##### **E: Solid earth response and geothermal heat flux**

- geothermal heat fluxes amplitude
- Relaxation time of the asthenosphere  $\tau_r$

In the following paragraphs, we explain the choice of the parameters shown in Table 4-3 and we give a detailed description of the results of the various sensitivity experiments.

**Table 4-3. Overview of the sensitivity experiments performed in this study.**

Parameter	Default value	Exp. ID	Experiment values	Description
<b>Climate forcing</b>				
$\lambda_{\text{Ann}} / \lambda_{\text{July}}$	5 / 4	A1	3 / 2	Lapse rates for surface air temperature ( $^{\circ}\text{C}/\text{km}$ )
		A2	6.5 / 5	
		A3	8.5 / 6	
$\gamma$	0.05	A4	0.03	Precipitation correction factor ( $^{\circ}\text{C}^{-1}$ )
		A5	0.07	
		A6	0.09	
		A7	0	
$p_{\text{solid}}$	–	A8	2	
		A9	4	
		A10	6	
	–	A11	snowfall CESM	
<b>PDD parameters</b>				
$C_{\text{snow}} / C_{\text{ice}}$	3 / 8	B1	4 / 9	Melting factors of ice and snow ( $\text{mm}/\text{d}/^{\circ}\text{C}$ )
		B2	2 / 7	
$\sigma$	5	B3	3	Standard deviation of daily surface air temperature ( $^{\circ}\text{C}$ )
		B4	4.5	
		B5	5.5	
		B6	7	
csi	60	B7	30	Percentage of refreezing (%)
		B8	70	
<b>Ice stream areas</b>				
$h_{\text{sed}}^* / h_w^*$	150 / 250	C1	30 / 50	Critical sediment thickness and critical hydraulic head (m)
sediment thickness	Laske and Masters 1997	C2	Laske and Masters 1997 and SGS merged	
$c_f$	$2 \cdot 10^{-5}$	C3	$1 \cdot 10^{-5}$	Basal drag coefficient (–)
		C4	$3 \cdot 10^{-5}$	
<b>Ice shelf areas</b>				
$H_{\text{calv}}$		D1	100	Critical thickness of ice shelves at the front (m)
		D2	150	
		D3	250	
		D4	300	
$b_{\text{melt}}$ (above / below 450 m)	0.2/2.45	D5	4	Melting rate below ice shelves (m/yr)
		D6	10	
<b>Solid earth</b>				
$\tau_r$		E1	5,000	Characteristic relaxation time (yrs)
		E2	10,000	
GHF	Shapiro and Ritzwoller 2004	E3	reduction by 10%	Geothermal heat flux ( $\text{mW}/\text{m}^2$ )
		E4	increase by 10%	
		E5	Shapiro and Ritzwoller 2004 and Näslund et al. 2005 merged	

#### 4.4.1 Results: overview

Figure 4-13 and Table 4-4 summarize the most important geometric parameters resulting from the simulated ice sheets (Eurasian ice volume, ice thickness and bedrock elevation at the Forsmark site) for all experiments conducted on the Eurasian 20 km grid using the B140\_Topo1 and B140\_Topo2 climate forcing.

All experiments were also conducted on the Northern Hemisphere 40 km grid, as initially planned in the project. Several of these experiments are used to explain some of the physical processes. For some of the experiments at 20 km, numerical instabilities resulting from substantial changes in some of the investigated parameters have not been overcome. As a result, those experiments are missing in Figure 4-13 and Table 4-4. Nevertheless, the missing experiments were conducted on the 40 km Northern Hemisphere grid (Figure 4-26 and Table 4-6). The overall results on the 40 km grid present the same trends as those conducted on the 20 km grid, see Section 4.5 below. Therefore, the overall interpretation of the impacts of the changes in parameters is similar for both grid resolutions. In the following subsections, we describe the results for each of the categories shown in Figure 4-13 and Table 4-4.

#### 4.4.2 Climate correction

##### Climate corrections during runtime

During runtime, the climate input fields are corrected for elevation changes, as described in Section 4.2.2. Surface air temperatures are corrected by means of a lapse rate, which takes different values for mean annual and July temperatures (Equation 4-32). In our simulations we varied these values between 3°C/km and 8°C/km, based on peer-reviewed literature.

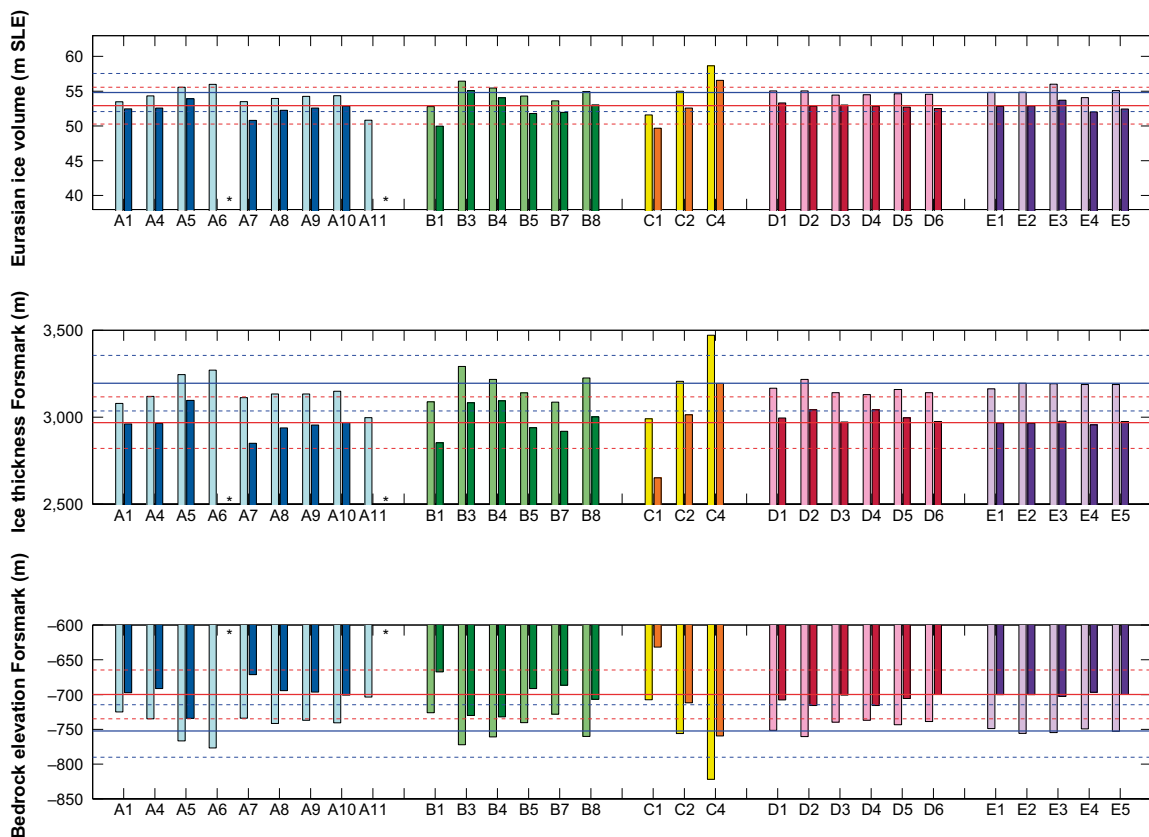


**Figure 4-13.** Final Eurasian ice volume (top), ice thickness in Forsmark (middle) and bedrock elevation in Forsmark (bottom) of experiments using B140\_Topo1 forcing (light colors) and B140\_Topo2 forcing (dark colors). The blue and red solid lines indicate the values of reference simulations REF\_Topo1 and REF\_Topo2, respectively (Figure 4-9). The dashed blue and red lines indicate  $\pm 5\%$  of the respective reference simulations values. Stars indicate sensitivity experiments that could not be conducted at 20 km resolution due to numerically unstable behavior of the model, but could be conducted at 40 km resolution (Figure 4-26).

**Table 4-4. Final Eurasian ice volume (m SLE), ice thickness (m) and bedrock depression in Forsmark (m) for all sensitivity experiments performed on the Eurasian 20 km grid. For each value, the change relative to the respective reference experiment is also given (in %). Experiments are grouped according to categories: Climate corrections (A), PDD parameters (B), Ice streams (C), Ice shelves (D) and Solid earth (E). Maximum and minimum values are highlighted.**

Run id	Eurasian ice volume				Ice thickness Forsmark				Ice thickness Forsmark			
	Topo1		Topo2		Topo1		Topo2		Topo1		Topo2	
	[m SLE]	[%]	[m SLE]	[%]	[m]	[%]	[m]	[%]	[m]	[%]	[m]	[%]
REF	54.8		52.9		3,196		2,969		-752		-700	
A1	53.5	-2.4	52.5	-0.9	3,078	-3.7	2,961	-0.3	-725	-3.7	-697	-0.4
A4	54.3	-0.9	52.6	-0.7	3,119	-2.4	2,964	-0.2	-735	-2.3	-691	-1.3
A5	55.6	1.4	53.9	1.9	3,244	1.5	3,097	4.3	-767	1.9	-734	4.9
A6	56.0	2.1	-	-	3,270	2.3	-	-	-777	3.3	-	-
A7	53.5	-2.4	50.8	-4.0	3,113	-2.6	2,850	-4.0	-734	-2.5	-671	-4.1
A8	54.0	-1.5	52.3	-1.3	3,134	-1.9	2,938	-1.0	-742	-1.4	-694	-0.8
A9	54.2	-1.0	52.6	-0.7	3,134	-1.9	2,955	-0.5	-737	-2.1	-696	-0.6
A10	54.4	-0.8	-	-	3,150	-1.4	-	-	-741	-1.5	-	-
A11	50.8	-7.3	-	-	2,997	-6.2	-	-	-704	-6.4	-	-
B1	52.8	-3.7	50.0	-5.6	3,088	-3.4	2,852	-3.9	-726	-3.5	-668	-4.6
B3	56.5	3.0	55.1	4.1	3,293	3.0	3,082	3.8	-772	2.6	-730	4.3
B4	55.4	1.2	54.0	2.1	3,217	0.7	3,094	4.2	-761	1.1	-732	4.6
B5	54.3	-0.9	51.8	-2.1	3,139	-1.8	2,940	-1.0	-740	-1.7	-691	-1.3
B7	53.6	-2.2	51.9	-1.9	3,086	-3.4	2,919	-1.7	-728	-3.3	-686	-2.0
B8	54.9	0.2	53.0	0.2	3,225	0.9	3,002	1.1	-760	1.0	-707	1.0
C1	51.6	-5.9	49.7	-6.1	2,991	-6.4	2,650	-10.7	-707	-6.0	-632	-9.7
C2	55.0	0.4	52.6	-0.7	3,206	0.3	3,013	1.5	-756	0.5	-712	1.7
C4	58.7	7.0	56.6	6.9	3,472	8.6	3,195	7.6	-822	9.2	-760	8.6
D1	55.0	0.4	53.3	0.7	3,167	-0.9	2,995	0.9	-751	-0.2	-708	1.2
D2	55.0	0.4	52.8	-0.2	3,217	0.7	3,042	2.5	-760	1.0	-716	2.3
D3	54.4	-0.7	53.0	0.2	3,141	-1.7	2,972	0.1	-740	-1.7	-701	0.2
D4	54.5	-0.6	52.6	-0.6	3,129	-2.1	2,961	-0.3	-737	-2.1	-698	-0.3
D5	54.6	-0.3	52.7	-0.4	3,159	-1.2	2,996	0.9	-743	-1.3	-706	0.9
D6	54.5	-0.5	52.5	-0.8	3,141	-1.7	2,976	0.3	-739	-1.8	-700	0.0
E1	54.8	0.0	52.8	-0.2	3,163	-1.0	2,966	-0.1	-749	-0.5	-700	0.0
E2	54.8	0.1	52.9	-0.1	3,196	0.0	2,965	-0.1	-756	0.5	-700	0.0
E3	56.0	2.2	53.7	1.5	3,193	-0.1	2,977	0.3	-755	0.3	-703	0.4
E4	54.1	-1.3	52.0	-1.7	3,188	-0.2	2,956	-0.4	-749	-0.5	-697	-0.4
E5	55.1	0.5	52.4	-0.9	3,188	-0.2	2,975	0.2	-753	0.1	-700	0.0

Present-day observations in East and West Antarctica reveal lapse rates ranging from 5.7 to 12.7°C/km, with larger values in higher elevations (Magand et al. 2004). Krinner and Genthon (1999) computed lapse rates for Greenland and Antarctica from the output of an Atmospheric General Circulation Model, and obtained values of ~5°C/km near the coast and ~10°C/km in plateau areas. Much lower lapse rates ( $\lambda_{Ann}=4.1^\circ\text{C}/\text{km}$ ,  $\lambda_{July}=4.3^\circ\text{C}/\text{km}$ ) were recently observed on the Prince of Wales ice field on Ellesmere Island, Canada (Marshall et al. 2007).

In our reference experiment, annual mean and July lapse rates are set to 5°C/km and 4°C/km. Our lapse rate for mean annual temperature follows Abe-Ouchi et al. (2007) who focused on the Northern Hemisphere ice sheets during the last glacial cycle. In their combined climate and ice-sheet modeling study the authors retrieved lapse rates from the simulated air temperature. Other ice-sheet modeling studies apply values slightly larger than ours (Table 4-5). Based on this, we decided to explore the impact of lapse rates on the ice sheet mass balance: For our sensitivity experiments, we choose lapse rates of  $\lambda_{Ann}=3^\circ\text{C}/\text{km}$  /  $\lambda_{July}=2^\circ\text{C}/\text{km}$  (experiment A1) in order to explore the effect of a rather small temperature correction, and larger lapse rates of  $\lambda_{Ann}=6^\circ\text{C}/\text{km}$  /  $\lambda_{July}=5^\circ\text{C}/\text{km}$  and  $\lambda_{Ann}=8^\circ\text{C}/\text{km}$  /  $\lambda_{July}=6.5^\circ\text{C}/\text{km}$  (experiments A2 and A3, respectively) to cover the range of commonly used values in the literature.

**Table 4-5. Atmospheric lapse rates commonly used in ice sheet modeling literature.**

	Model	Annual mean lapse rates	July lapse rates
<b>Abe-Ouchi et al. (2007):</b> NH ice sheets during the last glacial cycle	IcIES	5°C/km	5°C/km
<b>Charbit et al. (2002):</b> NH ice sheets during the last deglaciation	GRISLI	8°C/km	6.5°C/km
<b>Peyaud et al. (2007):</b> Early Weichselian Eurasian ice sheets	GRISLI	6°C/km	5°C/km
<b>Quiquet et al. (2012):</b> Present-day Greenland ice sheet	GRISLI	6.309°C/km	5.426°C/km
<b>Ritz et al. (2001):</b> Antarctic ice sheet over the past 420,000 yrs	GRISLI	9.14°C/km	9.14°C/km
<b>Vizcaíno et al. (2010):</b> Future ice sheet changes	SICOPOLIS	6.5°C/km	6.5°C/km

Compared with reference experiments REF\_Topo1 and REF\_Topo2, using  $\lambda_{Ann} = 3^\circ\text{C}/\text{km}$  /  $\lambda_{July} = 2^\circ\text{C}/\text{km}$  (experiment A1) leads to a smaller Eurasian ice volume (~4%) and to a lower ice thickness in Forsmark by 120 m (Table 4-4 and Figure 4-14a). This is because the temperature correction relative to the reference values  $5^\circ\text{C}/\text{km}$  /  $4^\circ\text{C}/\text{km}$  results in a smaller correction, which leads to a cooling over the entire ice sheet (Figure 4-14b). As a consequence, accumulation is lower than in REF\_Topo1 and REF\_Topo2 (Figure 4-14c). However, the combination of lapse rates tested in this experiment is smaller than commonly used values to simulate the Eurasian ice sheet (Abe-Ouchi et al. 2007, Peyaud et al. 2007), and therefore the results should be interpreted with care.

Experiments A2 and A3, exploring the effect of rather large lapse rates, could not be conducted on the Eurasian 20 km grid due to numerically unstable behavior of the model. These instabilities occurred particularly at the transition zone between SIA and SSA, (e.g. Calov et al. 2010). Even if the model time step was decreased substantially to meet the CFL conditions, the instabilities were not overcome. However, these experiments could be carried out on the Northern Hemisphere 40 km grid (Figure 4-26). Note that most of the published Eurasian ice-sheet simulations have been carried out with a horizontal resolution coarser than 40 km (e.g. Peyaud et al. 2007, Ritz et al. 2001, Abe-Ouchi et al. 2007). At this resolution, topography is also smoother and the transition between SIA and SSA is more stable. Results from the Northern Hemisphere 40 km runs indicate that using very high lapse rates such as  $\lambda_{Ann} = 8^\circ\text{C}/\text{km}$  /  $\lambda_{July} = 6.5^\circ\text{C}/\text{km}$  (experiment A3) leads to a retreat of the western part of the Eurasian ice sheet. Therefore, assuming that the whole Late Saalian ice sheet topography should remain, these large lapse rates are not suitable to simulate the MIS 6 Eurasian ice sheet with the currently imposed climate forcing and maintain its particularly high topography mean annual (see the Discussion in Section 5.6). Experiment A2 ( $\lambda_{Ann} = 6.5^\circ\text{C}/\text{km}$  /  $\lambda_{July} = 5^\circ\text{C}/\text{km}$ ),

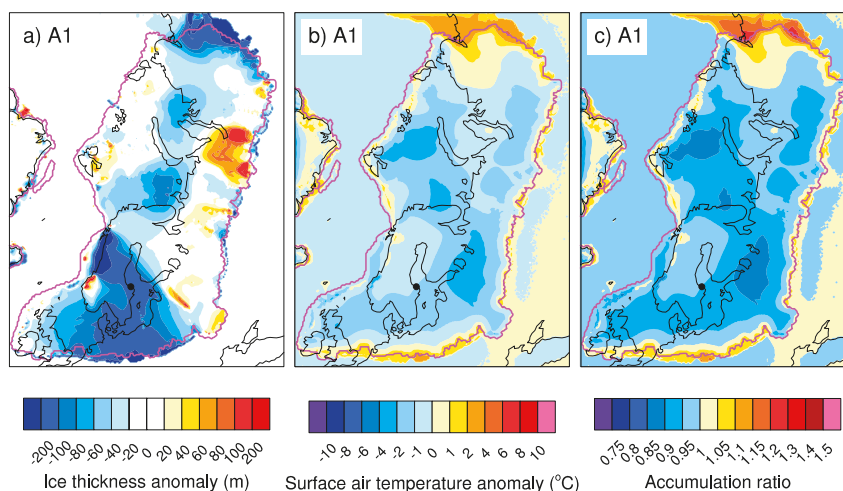


**Figure 4-14. Impact of lapse rates:** Difference in (a) ice thickness, (b) mean annual surface air temperature and (c) ratio of accumulation of experiment A1 relative to the reference experiment REF\_Topo1 at the end of the simulation (experiment A1 minus (or divided) by reference experiment). The black dot indicates the Forsmark site, and the magenta line indicates the extent of the Late Saalian ice sheet from Peyaud (2006). See Appendix 3 for the figures using B140\_Topo2 forcing.

performed on the Northern Hemisphere 40 km grid, shows a slight increase in Eurasian ice volume of 0.3 m SLE compared with REF\_Topo1. Over the Forsmark site, ice thickness increases by ~40 m relative to REF\_Topo1 (Table 4-4). Therefore, a moderate increase in lapse rates relative to the reference experiment leads to a compensating effect. On the one hand, increasing lapse rates leads to higher surface air temperatures and therefore more ablation and a warmer base through diffusion; on the other hand it leads to an increase in accumulation.

In general, the sensitivity of the Eurasian ice sheet to moderate changes in lapse rates is not very large. But this is only valid for a certain range of lapse rate (e.g. lapse rates in A1 and A2). Exceeding this range (e.g. experiment A3) results in a retreat of the ice sheet in areas where air temperatures are particularly warm.

Precipitation is corrected for elevation changes as well, based on changes in the saturation water pressure (Clausius-Clapeyron relationship, Equation 4-34). For the precipitation correction factor  $\gamma$ , we adopt a value of  $0.05^\circ\text{C}^{-1}$  for the reference experiments. This is similar to the value used by Charbit et al. (2002), who also tested values ranging from  $0.03^\circ\text{C}^{-1}$  to  $0.078^\circ\text{C}^{-1}$  in their study of last deglaciation Northern Hemisphere ice sheets. However, Charbit et al. (2002) stated that varying  $\gamma$  has a negligible impact on the deglaciation process. Ritz et al. (2001) and Quiquet et al. (2012) choose a slightly larger value,  $0.07^\circ\text{C}^{-1}$ , for studying Antarctic and Greenland paleo-ice sheets, respectively.

In order to test the effect of the precipitation correction factor  $\gamma$ , we performed experiments with  $\gamma=0.03^\circ\text{C}^{-1}$ ,  $\gamma=0.07^\circ\text{C}^{-1}$  and  $\gamma=0.09^\circ\text{C}^{-1}$  (experiments A4, A5 and A6, respectively), following Charbit et al. (2002). Compared with REF\_Topo1 and REF\_Topo2, a smaller factor as in experiment A4 reduces the overall accumulation, while a larger factor increases accumulation (Figures 4-15c and 4-15d, Equation 4-34). This results in a slightly smaller Eurasian ice volume in case of experiment A4 (0.5 m SLE smaller than REF\_Topo1, Figure 4-15a), and a larger Eurasian ice volume in case of A5 and A6 (0.8 and 1.2 m SLE larger than REF\_Topo1, respectively, Figure 4-15b). Ice thickness at the Forsmark site is ~80 m lower in experiment A4, while it is ~50 m and ~70 m higher in experiments A5 and A6 compared with REF\_Topo1, respectively (Table 4-4). Over east Siberia, the opposite effect occurs: In the reconstruction of the MIS 6 Eurasian ice sheet from Peyaud (2006), the ice sheet does not extent over the eastern Siberian shelf. But in our reference simulation, an ice sheet builds up over this area. Hence, climate correction during runtime is performed relative to sea-level elevation. As a consequence, a decreased precipitation correction, as in experiment A4, leads to a growth of the ice sheet in this area, and vice versa for experiments A5 and A6.

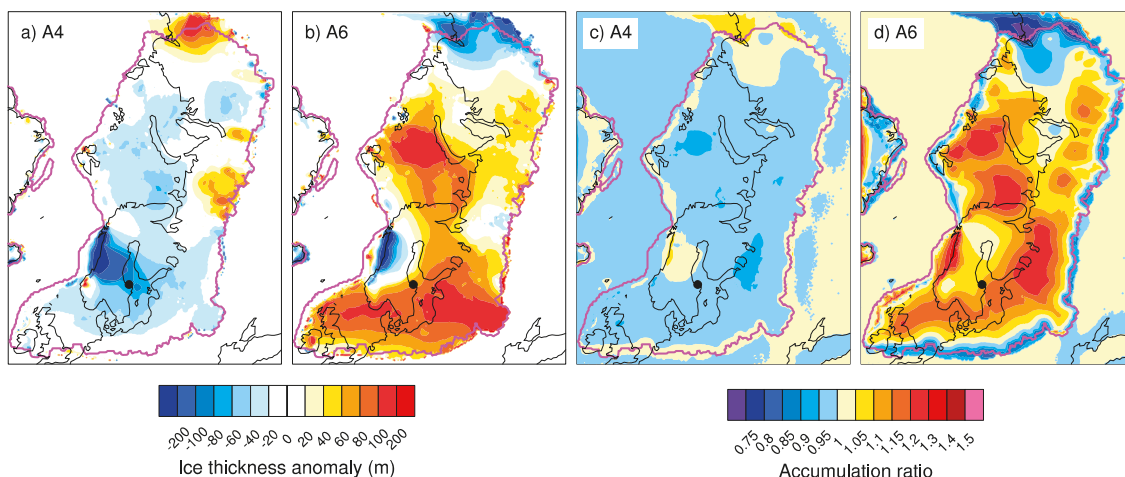


**Figure 4-15.** Impact of precipitation correction factor  $\gamma$ : Difference in ice thickness (left) and accumulation (right) between the reference experiment REF\_Topo1 and experiments A4 (a, c) and A6 (b, d) at the end of the simulation (sensitivity experiments minus reference experiment). The black dot indicates the Forsmark site, and the magenta line indicates the extent of the reconstructed Late Saalian ice sheet from Peyaud (2006). See Appendix 3 for the figures using B140\_Topo2 forcing.

### Impact of temperature on precipitation conversion into snow

In our reference simulations, the total precipitation is turned into snow with a density of  $917 \text{ kg/m}^3$ . Another approach would be to define a temperature threshold for the conversion of precipitation into snow. In this case, we would scale the total precipitation with the fraction of days per year below a certain temperature threshold  $p_{solid}$  ( $^{\circ}\text{C}$ ):

$$P_{cor}(t) = P_0 \cdot \exp(\gamma \cdot (T_{cor}(t) - T_0)) \cdot FT, \quad (4-35)$$

where  $FT$  stands for the fraction of days per year below the temperature threshold  $p_{solid}$ . In the ice sheet model GLIMMER, for example  $p_{solid}$  is set to  $1^{\circ}\text{C}$  (Rutt et al. 2009). In our case, the prescribed surface air temperatures from B140\_Topo1 and B140\_Topo2 forcing are already very low (Figure 4-7), therefore most of the total precipitation corresponds to snowfall except at the ice-sheet margins where the temperature is warmer. But nonetheless in a first phase we investigated the impact of this particular temperature threshold  $p_{solid}$ , and conducted experiments in which we set this parameter to  $0^{\circ}\text{C}$ ,  $2^{\circ}\text{C}$ ,  $4^{\circ}\text{C}$  and  $6^{\circ}\text{C}$  (experiments A7, A8, A9 and A10).

Compared with the reference simulations in which no threshold is imposed, the use of  $p_{solid}$  leads to a decrease in the accumulation rate, ranging from a decrease of 2% (experiment A10,  $p_{solid}=6^{\circ}\text{C}$ ) to 9% (experiment A7,  $p_{solid}=0^{\circ}\text{C}$ ). Therefore, ice volume reduces by up to 1.3 m SLE in the case of  $p_{solid}=0^{\circ}\text{C}$  (experiment A7) compared with REF\_Topo1 (Figure 4-13 and Table 4-4). Simulated ice thickness over Forsmark in experiment A7 is  $\sim 90 \text{ m}$  lower than in the reference experiment. The sensitivity of those experiments is similar when using B140\_Topo2 climate forcing. Compared with REF\_Topo2,  $p_{solid}=0^{\circ}\text{C}$  induces a decrease of about 2 m SLE, and of about 120 m in ice thickness over Forsmark.

In a second phase, instead of considering a temperature threshold, we use the snowfall field from both climate simulations in Experiment A11. Using snowfall instead of total precipitation reduces the ice volume by about 4 m SLE compared with REF\_Topo1 and by 4.8 m SLE compared with REF\_Topo2. Over Forsmark, it leads to 200 m and 220 m difference in ice thickness with respect to REF\_Topo1 and REF\_Topo2, respectively (Figure 4-16, Figure 4-13 and Table 4-4).

To conclude, these experiments reveal that the model is relatively sensitive to changes in the accumulation rate. In this category, the snowfall experiment (A11) marks the lower bound of the experiments with a decrease of ice volume by up to 3.6 m SLE (relative to REF\_Topo1).

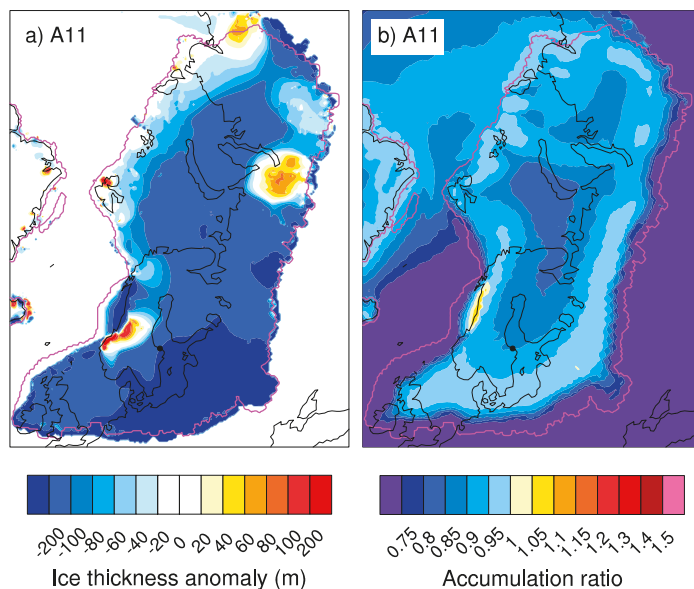


**Figure 4-16.** Comparison between total precipitation and snowfall from B140\_Topo1 climate forcing: (a) Difference in ice thickness between experiment A11 and REF\_Topo1 (A11 minus REF\_Topo1) and (b) accumulation ratio between experiment A11 and REF\_Topo1 (A11 divided by REF\_Topo1). The black dot indicates the Forsmark site, and the magenta line indicates the extent of the reconstructed Late Saalian ice sheet from Peyaud (2006).

### 4.4.3 Positive Degree Day semi-empirical model

As listed in the previous section, we investigate some of the parameters affecting the calculation of ablation: melting rates,  $C_{snow}$  and  $C_{ice}$ , the standard deviation of the daily temperature cycle,  $\sigma$ , and the amount of refreezing ice,  $csi$ . Ablation in GRISLI is calculated with the semi-empirical PDD method following Reeh (1991), which assumes that the number of positive degree days (Equation 4-28) is proportional to melting of snow and ice.

Generally, melting rates for snow and ice are set to 3 mm/d/°C and 8 mm/d/°C, respectively, taking into account the difference in albedo between snow and ice. These values result from observations by Braithwaite (1995). Rather high melting rates of 17 mm/d/°C and 8 mm/d/°C for snow and ice, respectively, were used by Peyaud et al. (2007) in their study of the Early Weichselian Eurasian ice sheet. Quiquet et al. (2012) adopted values of 5 mm/d/°C and 8 mm/d/°C for snow and ice, respectively, for a present-day Greenland ice-sheet modeling study.

The standard deviation of daily temperature is commonly set to 5°C (Abe-Ouchi et al. 2007, Rutt et al. 2009, Bonelli et al. 2009), but it can range from 4.5°C (Greve 2005) to 5.5°C (Tarasov and Peltier 1999). Marshall et al. (2002) tested values ranging from 3°C to 7°C in their modeling study of the Laurentide ice sheet.

In the standard PDD method from Reeh (1991), the maximum amount of refreezing  $csi$  cannot exceed 60% of the amount of water coming from melting of the annual snowfall. A larger value, 70%, was proposed by Pfeffer et al. (1991), who use a simple energy balance model.

In order to span the range of PDD parameters commonly used in the literature, we performed experiments with higher melting rates ( $C_{ice} = 9$  mm/d/°C and  $C_{snow} = 4$  mm/d/°C, experiment B1), and lower melting rates ( $C_{ice} = 7$  mm/d/°C and  $C_{snow} = 2$  mm/d/°C, experiment B2). Four experiments were conducted to test different values of  $\sigma$ , namely 3°C (experiment B3), 4.5°C (experiment B4), 5.5°C (experiment B5) and 7°C (experiment B6). The amount of refreezing is set to 30% in experiment B7 and to 70% in experiment B8.

Compared with both reference experiments REF\_Topo1 and REF\_Topo2, using higher melting rates for ice and snow (experiment B1) increases the amount of ablation occurring along the western margins of the ice sheet by about 1 m/yr and by about 0.5 m/yr along the eastern and southern margins (Figure 4-17b). The stronger ablation destabilizes the southern margins of the ice sheet, leading to larger sliding velocities (Figure 4-17c), which further enhances mass loss from the ice sheet (Figure 4-17a). Consequently, this affects the overall dynamics of the Eurasian ice sheet. Ice thickness over Forsmark reduces by ~110 m and ~120 m, and the total ice volume decreases by 2 m SLE and 2.9 m SLE, relative to REF\_Topo1 and REF\_Topo2 (Figure 4-13 and Table 4-4). The opposite effect occurs when decreasing melting factors (experiment B2): Using factors of  $C_{ice} = 7$  mm/d/°C and  $C_{snow} = 2$  mm/d/°C results in an increase of the Eurasian ice volume by 2 m SLE (experiment performed on NH40 grid, see Figure 4-26).

Decreasing or increasing the standard deviation of the daily temperature cycle induces changes of the same order as the changes resulting from melting rates: Ablation decreases by about 0.5 m/yr at the margins of the ice sheet in experiment B4 using  $\sigma=4.5^\circ\text{C}$  and increases by about 0.3 m/yr in experiment B5 using  $\sigma=5.5^\circ\text{C}$  (Figure 4-18). Consequently, the ice volume increases in B4 by 0.6 m SLE, while it decreases in B5 by 0.5 m SLE relative to REF\_Topo1 (Figure 4-13). An even smaller value ( $\sigma=3^\circ\text{C}$ , experiment B3) leads to an increase in ice volume by 1.7 m SLE compared with REF\_Topo1.

In experiment B6 which explores the effect of a large daily air temperature standard deviation of 7°C, the Eurasian ice volume exhibits oscillatory surges. In this case, the ice sheet does not converge towards a steady state. These oscillations are due to instabilities at the transition zone of the Shallow Ice and Shallow Shelf Approximation (Calov et al. 2010). We do not include this experiment in the further analysis.

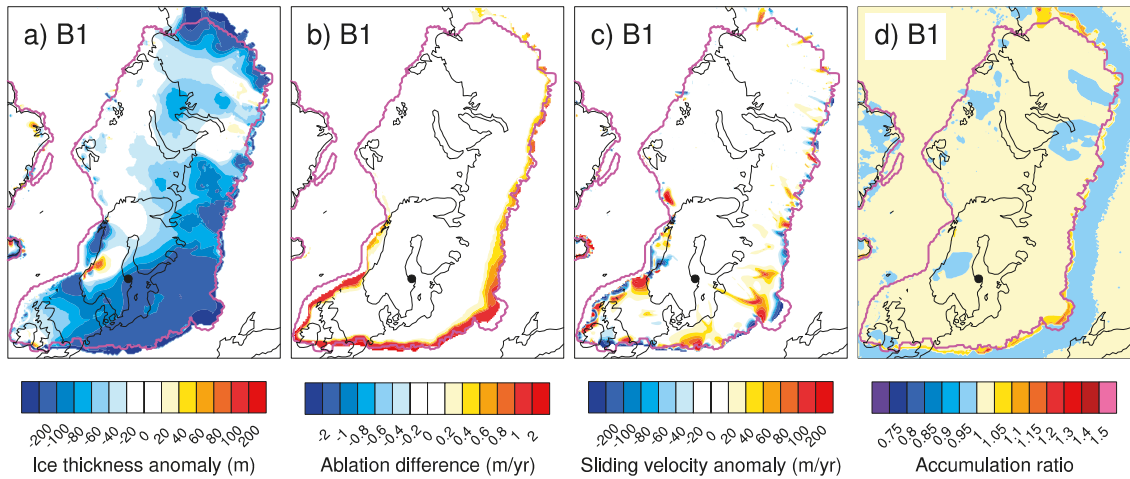


**Figure 4-17.** Impact of  $C_{snow}$  and  $C_{ice}$ : Difference in ice thickness (a), ablation (b), sliding velocity (c) and ratio of accumulation (d) of experiment B1 relative to the reference experiment REF\_Topo1 at the end of the simulation (experiment B1 minus (or divided by) reference experiment). The black dot indicates the Forsmark site, and the magenta line indicates the extent of the reconstructed Late Saalian ice sheet from Peyaud (2006). See Appendix 3 for the figures using B140\_Topo2 forcing.

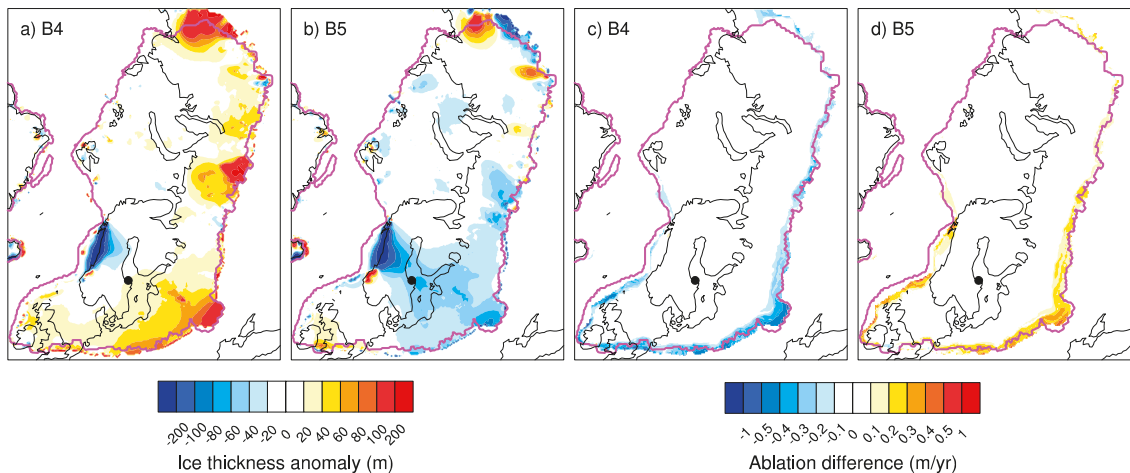


**Figure 4-18.** Impact of daily temperature standard deviation  $\sigma$ : Difference in ice thickness (left) and ablation (right) between the reference experiment REF\_Topo1 and experiments B4 (a, c) and B5 (b, d) at the end of the simulation (sensitivity experiments minus reference experiment). The black dot indicates the Forsmark site, and the magenta line indicates the extent of the reconstructed Late Saalian ice sheet from Peyaud (2006). See Appendix 3 for the figures using B140\_Topo2 forcing.

The ice sheet also responds to changes in the amount of refreezing,  $csi$ . Increasing this to 70% increases the amount of meltwater allowed to refreeze on the ice sheet surface by 10% compared with REF\_Topo1 and REF\_Topo2. This leads to a slight increase in the Eurasian ice volume by 1 m SLE (experiment B7, Figure 4-13). Reducing  $csi$  to 30%, as in experiment B8, leads on the contrary to a thinner Eurasian ice sheet (by 1 m SLE), as the rate of runoff increases. This low  $csi$  value is relatively unrealistic, as observations suggest values around 60%. Nonetheless this experiment gives an idea of the sensitivity of the Eurasian ice sheet to refreezing, which appears to be weak because ablation is already low in our experiments. Therefore, even when using lower or larger rates of refreezing, changes in ice volume are small.

In general, the results of the sensitivity tests described in this section indicate that PDD parameters, particularly melting factors  $C_{snow}$  and  $C_{ice}$  and the standard deviation of the daily temperature cycle  $\sigma$ , have an important effect on the geometry of the ice sheet. Hence, the effect of PDD parameters should preferably be further investigated. One aspect could be to include a dependency of melting factors and  $\sigma$  on surface elevation, as described in Charbit et al. (2013).

#### 4.4.4 Ice streams

##### **Extent of ice stream areas**

Ice streams play an important role for the overall dynamics of ice sheets (Goldstein et al. 1993, Joughin et al. 2001). The treatment of these fast-flowing areas is one of the advantages of GRISLI, as it allows for a more realistic simulation of areas characterized by ice streams. Other ice-sheet models do not include this specific treatment of ice-stream areas (e.g. GLIMMER, Rutt et al. 2009). In the early versions of the model, a simple criterion based on basal drag was applied (e.g.  $\tau < 0.25$  bar, see Ritz et al. 2001) to decide in every time step whether a grid point is considered as an “ice stream grid point”. Peyaud (2006) significantly improved the criterion for ice stream areas by including a basal hydrology scheme into GRISLI (see Section 5.1.5). In this scheme, a new criterion to define ice streams is based on the presence of a thick sediment layer at the base of the ice sheet, which is saturated by meltwater (determined by the hydraulic head). Note that besides areas with thick and saturated sediment, ice streams can also occur in narrow valleys and ice rises (Section 5.1.4). The importance of the connection between sediment and ice-sheet fast-flow areas was highlighted by Clark et al. (1996), who showed in their study of the Laurentide ice sheet during the LGM that a soft bed (wet, deformable till or sediment) is closely related to enhanced flow. However, the authors do not specify the critical sediment thickness which is necessary to trigger fast flow.

The basal hydrology is constrained by two thresholds:  $h_w^*$  (hydraulic head) set to 250 m and determined based on a Darcy-type flow law, and  $h_{sed}^*$ , which corresponds to the minimum sediment thickness saturated by meltwater to activate the ice streams. This value is set to 150 m in Peyaud (2006). The distributed sediment thickness is from Laske and Masters (1997). However, there exists no direct evidence constraining these values, which constitute the largest uncertainties in our experiments.

In a first phase we investigated the impact of these two thresholds, and conducted a first experiment with smaller values ( $h_{sed}^* = 30$  m and  $h_w^* = 50$  m, experiment C1). These thresholds lead to an expansion of the area of fast flow compared with REF\_Topo1 and REF\_Topo2, consequently basal velocities are enhanced (Figure 4-19d). This reduces the Eurasian ice volume by 3.2 m SLE compared with both REF\_Topo1 and REF\_Topo2, and the ice thickness over Forsmark by ~200 m and ~370 m compared with REF\_Topo1 and REF\_Topo2, respectively (Figure 4-13 and Table 4-4).

In a second phase, a high-resolution data set of sediment thickness (over Sweden) from the Swedish Geological Survey (SGS) was prescribed. This dataset was merged with the global data set from Laske and Masters (1997), and used as input for sensitivity experiment C2 (Figure 4-2). Compared with the reference experiment REF\_Topo1, the overall Eurasian ice volume and ice thickness over Forsmark does not change significantly (Figure 4-13 and Table 4-4). However, in contrast to the Laske and Masters (1997) data set, the sediment thickness from SGS is almost zero along the southern Swedish coast. This leads to lower sliding velocities in this area, and consequently a slightly larger ice thickness at the southern tip of Sweden (Figure 4-19b and 4-19e). The difference in ice thickness along the Norwegian coast can be attributed to variable ice thickness in this area where an ice shelf is developing. However, this ice shelf is unstable and never spreads over the ocean domain more than a few grid points. This is indicated by a high standard deviation of ice thickness in this area (Figure A3-10 in Appendix 3).

##### **Basal drag coefficient**

An important parameter in the velocity equation for ice stream areas (Equation 4-19 and 4-20) is the basal drag coefficient  $c_f$ , which is a scaling factor for the basal drag  $\tau_b$ . In the work of Peyaud (2006),  $c_f$  is set to  $1 \cdot 10^{-5}$  and  $2 \cdot 10^{-5}$ . Alvarez-Solas et al. (2011) chose larger values ( $1 \cdot 10^{-4}$ ,  $2 \cdot 10^{-4}$  and  $1 \cdot 10^{-3}$ ) in order to simulate Heinrich events, which are characterized by very unstable ice sheet behavior. In our reference experiments,  $c_f$  is set  $2 \cdot 10^{-5}$ , while we investigate the effect of  $c_f = 1 \cdot 10^{-5}$  and  $c_f = 3 \cdot 10^{-5}$  in the sensitivity experiments (C3 and C4).

Compared with REF\_Topo1 and REF\_Topo2, a larger basal drag coefficient, as in experiment C4, reduces the velocities at the base of the ice sheet in ice-stream areas (Figure 4-19f), which are located mostly where the sediment layer is thick. Consequently, compared with REF\_Topo1 and REF\_Topo2, the ice sheet gains mass and the overall Eurasian ice volume increases by ~3.9 m SLE and 3.7 m SLE, while ice thickness over Forsmark increases by ~280 m and ~230 m, respectively (Figure 4-13 and Table 4-4).

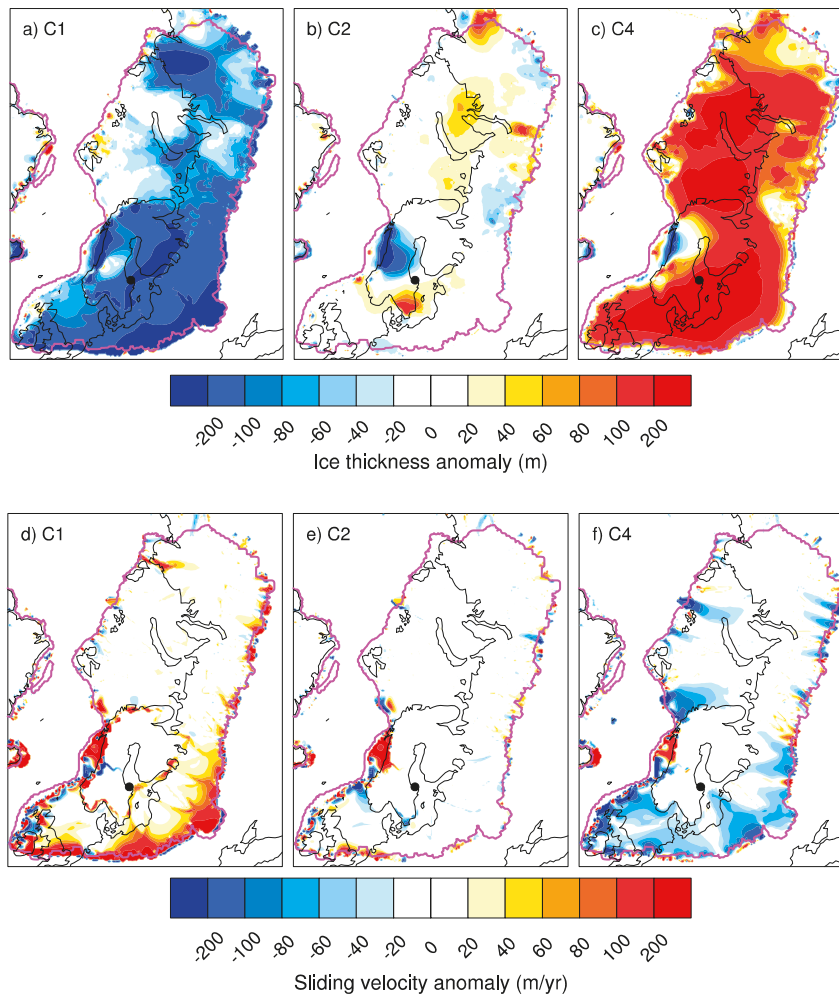


**Figure 4-19.** Impact of ice-stream parameters: Difference in ice thickness (top) and sliding velocity (bottom) between experiments C1 (a, d) and C2 (b, e) and C4 (c, f) and the reference experiment REF\_Topo1 at the end of the simulation (sensitivity experiments minus reference experiment). The black dot indicates the Forsmark site, and the magenta line indicates the extent of the reconstructed Late Saalian ice sheet from Peyaud (2006). See Appendix 3 for the figures using B140\_Topo2 forcing.

Due to numerical instabilities, we could not conduct experiment C3 on the Eurasian 20 km grid. The small basal drag coefficient results in large sliding velocities, leading to instabilities in the transition zone of SIA and SSA. However, the experiment was conducted on the Northern Hemisphere 40 km grid, and revealed a decrease in Eurasian ice volume by 3.7 m SLE relative to the reference simulation using B140\_Topo1 climate forcing. Over Forsmark, the ice thickness reduces by ~350 m compared with REF\_Topo1 (Figure 4-26).

In general, the model is highly sensitive to changes in parameters defining the ice-stream area, and also to changes in the basal drag coefficient. The “ice stream” experiments described in this section clearly mark the lower and upper bounds of all performed sensitivity experiments, ranging from a decrease of the Eurasian ice volume of 3.2 m SLE (experiment C1) to an increase by 4 m SLE (experiment C4) compared with REF\_Topo1. Note that some of the tested parameter such as the sediment thickness threshold  $h_{sed}^*$  are not constrained due to the lack of observations. Therefore, the interpretation of the result has to be done cautiously.

#### 4.4.5 Ice shelves

##### Calving

Calving of the ice shelf in this model version is simulated with a thickness criterion. As soon as the ice thickness in an ice shelf node at the front reaches a certain threshold  $H_{calv}$ , the node is “cut off”. In the literature, this threshold ranges from 150 m to 250 m, mostly based on observation of Antarctic ice shelves (Ritz et al. 2001, Peyaud et al. 2007, Vizcaíno et al. 2010). In the reference experiment,  $H_{calv}$  is set to 200 m. In order to investigate the impact of this parameter, we performed sensitivity experiments with lower thresholds of  $H_{calv} = 100$  m (experiment D1) and  $H_{calv} = 150$  m (experiment D2), and larger thresholds of  $H_{calv} = 250$  m (experiment D3) and  $H_{calv} = 300$  m (experiment D4).

Most parts of the simulated ice sheet are grounded and almost no ice shelf develops in our simulations (Figure 4-11). When using a lower calving threshold compared with the reference value of 200 m (100 m in experiment D1), the ice shelf area is slightly larger than in the reference experiment, and vice versa for a larger calving threshold (Figure 4-20e and 4-20f). However, the simulated ice shelf area is so small (only a few grid points) that slight changes in the area do not lead to significant changes in the overall ice thickness (Figure 4-20a and 4-20b). However, there are some differences in ice thickness compared with the reference simulation (Figure 4-20a and 4-20b), which can be explained by the overall variability of the simulated Eurasian ice sheet, as shown in a map of standard deviation of ice thickness (Figure A3-10a in Appendix 3). To conclude, sensitivity experiments testing different calving thresholds reveal that the overall Eurasian ice volume is not affected because most of the ice sheet is grounded (Table 4-4).

##### Oceanic basal melting rate

Basal melting below the ice shelves is strongly affected by the large-scale oceanic circulation (e.g. Hellmer et al. 2012). Thus, it has to be noted that assuming a homogeneous melting rate as in our experiments is a substantial simplification, but common in ice-sheet modeling studies. Ritz et al. (2001) set the basal melting rate to 0.2 m/yr and to 0.4 m/yr, and varied it linearly with temperature to simulate the transient evolution of Antarctica over the last 420 kyrs. Peyaud et al. (2007), who simulated the evolution of the Eurasian ice sheet, used a depth criterion for basal melting ranging from 0.2 to 2 m/yr for depths smaller than 450 m. Below 450 m depth, a higher rate of 8 m/yr was chosen in both studies.

Similarly in our reference experiments, the oceanic basal melting rate  $b_{melt}$  depends on depth and is set to 0.2 m/yr above 450 m and to 2.45 m/yr below 450 m depth. In order to test the sensitivity of our simulated Late Saalian Eurasian ice sheet to this model parameter, we explored the impact of substantially higher values,  $b_{melt} = 4$  m/yr and  $b_{melt} = 10$  m/yr (experiments D3 and D4). Keeping in mind that our simulated climate representative of the MIS 6 glacial maximum is very cold, these values are relatively high even compared with commonly used values in the literature and might not be realistic. According to the modeling study of present-day and future ice shelf-ocean interaction at the Filchner-Ronne Ice Shelf (Antarctica) by Hellmer et al. (2012), melting rates are around 0.2 m/yr, and might rise to 4 m/yr during the second half of the twenty-first century.

The model reacts to changes in the basal melting rate in a similar way as to changes in the calving threshold. The area along the Norwegian coast is particularly sensitive to the basal melting rate, since in this area an ice shelf is developing over the oceanic domain. As a consequence of the higher melting rates, the ice thickness decreases in this area by ~200 m (Figures 33c and 33d). This affects the nearby Forsmark site and leads to a reduction in ice thickness by ~50 m (experiment D3) and ~60 m (experiment D4) compared with REF\_Top01 (Table 4-4).

In our simulations, ice shelves are only present in a few grid points located in the area between northern Norway and Svalbard and north of Severnaya Zemlya (Figure 4-10). Therefore, the Eurasian ice sheet is not particularly sensitive to calving front thickness and basal melt rate below ice shelves in general. However, in the future we would like to test the impact of spatially varying oceanic heat fluxes.

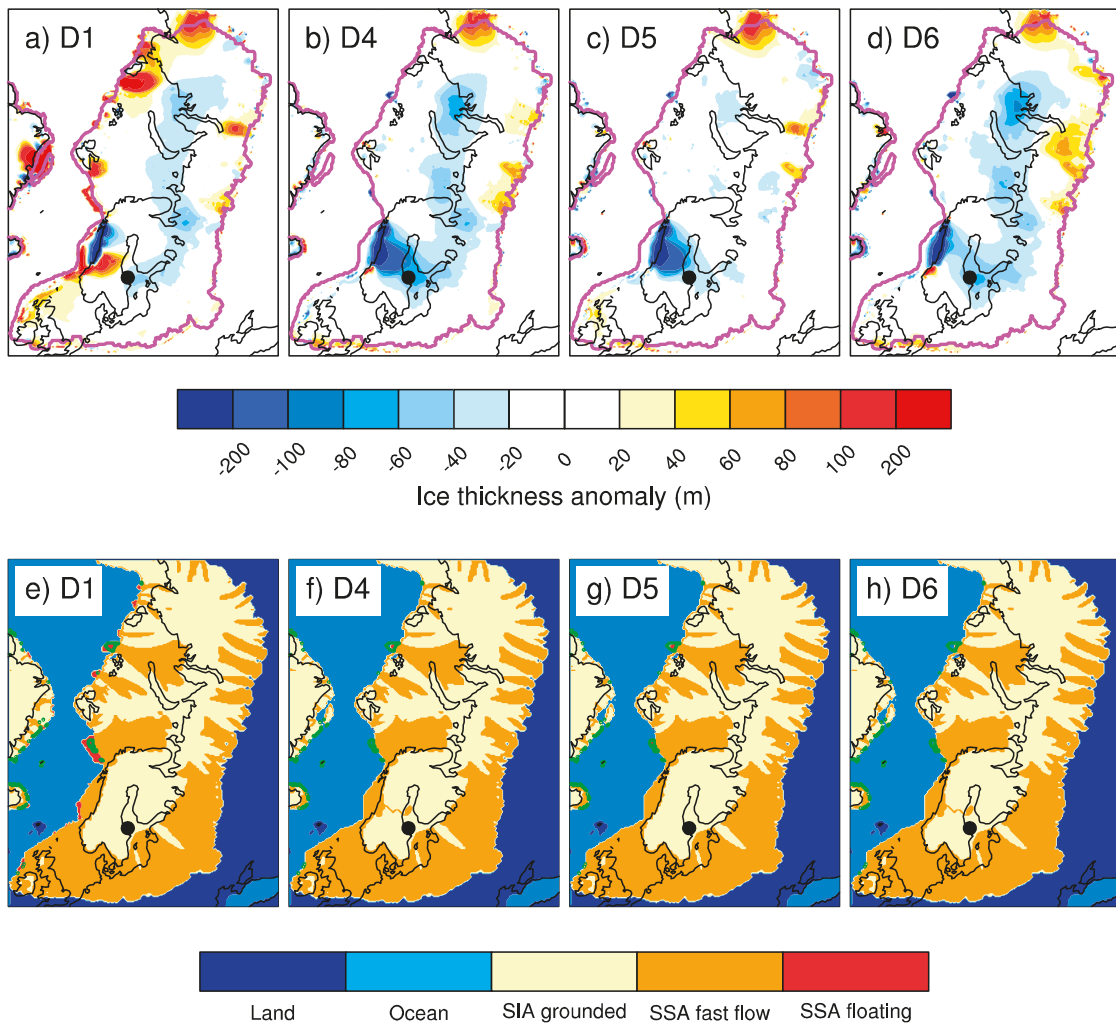


**Figure 4-20.** Impact of calving and ocean heat fluxes. Upper panel: Difference in ice thickness between experiments D1 (a), D4 (b), D5 (c) and D6 (d) and the reference experiment REF\_Topo1 at the end of the simulation (sensitivity experiments minus reference experiment). The black dot indicates the Forsmark site, and the magenta line indicates the extent of the reconstructed Late Saalian ice sheet from Peyaud (2006). Lower panel: Map of the different regions considered in GRISLI in experiments D1 (e), D4 (f), D5 (g) and D6 (h) at the end of the simulation: Land not covered by ice sheets (blue), ocean (light blue), grounded ice sheet area where the SIA applies (beige), fast-flowing ice sheet area where the SSA applies (orange) and ice shelves where the SSA applies (red). The green line indicates the ice shelf area of the reference experiment REF\_Topo1. See Appendix 3 for the figures using B140\_Topo2 forcing.

#### 4.4.6 Solid Earth

##### Isostasy

Isostatic processes are very important for ice-sheet dynamics. Crucifix et al. (2001) claimed that isostasy acts as a negative feedback for ice volume during the glaciation process and as a positive feedback during the deglaciation: Isostatic processes during the growth period lead to a lowering of the surface elevation, thereby increasing the area where melting might occur. In contrast, van den Berg et al. (2008) showed that the subsidence might be slower than the ice-sheet growth, and the ice sheet might still be able to grow despite the subsiding bedrock. They explain that there might even be a positive feedback, as lower surface elevation leads to warmer air temperatures, and as a result accumulation would increase. It is important to keep in mind that climate is acting at short time scales, while isostatic processes are acting on timescales of several millennia. Therefore, isostasy might matter most for the overall ice volume history, while climate matters at smaller time scales to build up the ice sheet.

In GRISLI, we apply the ELRA method to account for isostatic depression of the solid earth, treating the lithosphere-asthenosphere system with a visco-elastic rheology depending on time (see Section 4.1.8). The response time of the asthenosphere to changes in ice load is given by the characteristic relaxation time  $\tau_r$ , set to 3,000 yrs in GRISLI (Ritz et al. 2001, Huybrechts and de Wolde 1999, Charbit et al. 2013). But it might also be set to 5,000 yrs as in Abe-Ouchi et al. (2007) and Bonelli et al. (2009). Van den Berg et al. (2008) tested values of  $\tau_r$  ranging from 3,000 to 9,000 yrs, and concluded that a relaxation time of 3,000 yrs might be rather short for modeling the Eurasian ice sheet and suggested to rather use 5,000 yrs.

In two sensitivity experiments, we explored the impact of a larger relaxation time on the ice-sheet geometry (5,000 yrs and 10,000 yrs in experiments E1 and E2, respectively). We find that the simulated Eurasian ice sheet does not respond to changes in this time constant, both using B140\_Topo1 and B140\_Topo2 climate forcing (Figure 4-13 and Table 4-4). This is due to the fact that these experiments were branched from an already spun-up ice sheet (the reference experiments), which is already in isostatic equilibrium. Therefore, since elevation is not significantly changing in our sensitivity experiments, no substantial additional relaxation occurs. On top of this, ablation is low and only occurs along the southern margins of the ice sheet, where the ice sheet is thinnest. Therefore, our experiments are insensitive to changes in the characteristic time for relaxation.

### **Geothermal heat flux**

In GRISLI, geothermal heat flux (GHF) is used as a boundary condition for the computation of ice temperature at the base of the ice sheet. The basal ice temperature  $T_b$  is very important for the ice-sheet dynamics, as sliding of ice over the bedrock occurs only in areas where  $T_b$  exceeds the melting point.

Generally, a constant value of GHF is applied for the whole model domain: Ritz et al. (2001) use a constant value of 55 mW/m<sup>2</sup> for simulating the Antarctic ice sheet over the last 420 kyrs, while Abe-Ouchi et al. (2007) use a constant value of 42 mW/m<sup>2</sup> for their study of the Northern Hemisphere ice sheet during the last glacial cycle. In this model setup, we use a map of geothermal heat flux reconstructed by Shapiro and Ritzwoller (2004) with a resolution of 1°×1° (Figure 4-3), used also by Peyaud et al. (2007), Quiquet et al. (2012) and Bindschadler et al. (2013). Over Sweden and Finland, GHF from Shapiro and Ritzwoller (2004) ranges from 41.9 to 60.5 mW/m<sup>2</sup>, with a mean value of 49.5 mW/m<sup>2</sup>. A more accurate, high-resolution data set of GHF covering Sweden and Finland was provided by Näslund et al. (2005), ranging from 30 to 83 mW/m<sup>2</sup> over this area, with a mean value of 45.9 mW/m<sup>2</sup>. Using this high-resolution data set, Näslund et al. (2005) observe that basal meltwater volume is 1.4 times larger than using a low resolution data set when simulating the last glacial cycle.

In order to investigate the impact of GHF on the ice-sheet geometry, three experiments were carried out: First, we reduced the GHF from Shapiro and Ritzwoller (2004) by 10%, and second, we increased it by 10% (experiments E3 and E4). Over Sweden and Finland, the mean values of these two modified data sets are still in the range of constant values used in the studies of Ritz et al. (2001) and Abe-Ouchi et al. (2007). Third, the data set of Näslund et al. (2005) covering Sweden and Finland was merged with that of Shapiro and Ritzwoller (2004), and used as input map for GRISLI (experiment E5). Note that the average value from Näslund et al. (2005) leads to decrease of about 8% relative to Shapiro and Ritzwoller (2004) over Sweden and Finland.

Reducing GHF (experiment E3) increases the Eurasian ice volume by around 1 m SLE, while increasing GHF (experiment E4) leads to a decrease of 1 m SLE (Figure 4-13 and Table 4-4). As shown in Figure 4-21a and 4-21b, the changes in GHF affect mainly the eastern part of the Eurasian ice sheet. In this region, the lower (higher) GHF is associated with a decrease (increase) of basal temperatures of about -3°C (or +3°C) with respect to REF\_Topo1 and REF\_Topo2 (Figure 4-21d and 4-21e). Over the western part of the ice sheet, basal temperatures are already at the melting point (Figure 4-12), partly due to relatively warm surface air temperatures over this area (Figure 4-7). This basal temperature threshold is particularly important, as basal sliding is only permitted in case of a “warm” base. Hence there are no significant changes in ice thickness over the Forsmark area in these two experiments.

Applying the merged GHF data set (Shapiro and Ritzwoller (2004) and Näslund et al. (2005) over Sweden and Finland) as input in GRISLI (experiment E5) led to no significant changes in Eurasian volume and in Forsmark ice thickness. This is due to basal temperatures in REF\_Topo1 and REF\_Topo2 which are already at the pressure melting point over the western part of the ice sheet (Figure 4-12).

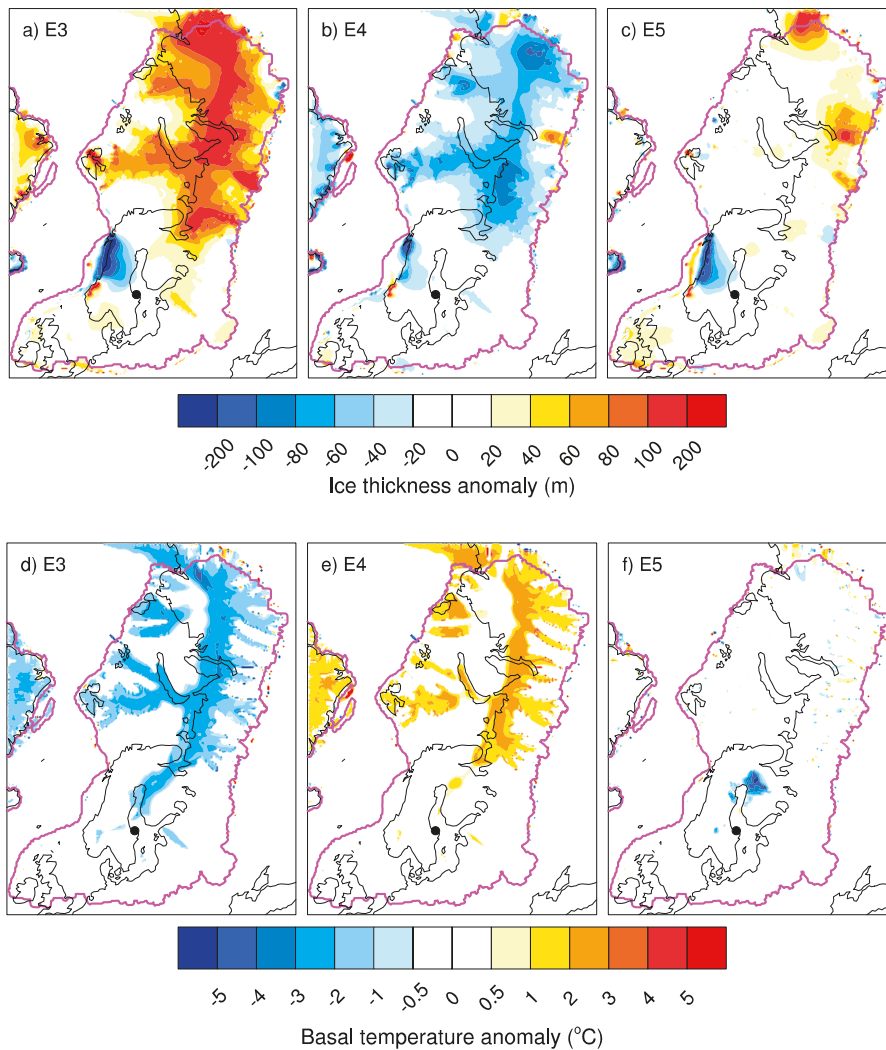


**Figure 4-21.** Impact of geothermal heat fluxes: Difference in ice thickness (top) and basal temperature relative to the pressure melting point  $T_b$  (bottom) between experiments E3 (a, d), E4 (b, e) and E5 (c, f) and the reference experiment REF\_Topo1 at the end of the simulation (sensitivity experiments minus reference experiment). Note that  $T_b$  is only computed for negative temperatures. The black dot indicates the Forsmark site, and the magenta line indicates the extent of the reconstructed Late Saalian ice sheet from Peyaud (2006). See Appendix 3 for the figures using B140\_Topo2 forcing.

To conclude, the model does not react very sensitively to changes in GHF. This is due to the relatively warm input climate (Figure 4-7) and the large volume of the Eurasian ice. Both factors lead to a base where large parts, and particularly the western part, are already at the pressure melting point when using the original data set from Shapiro and Ritzwoller (2004). Thus, reducing GHF might only lead to a slightly colder base.

#### 4.5 Sensitivity experiments: preliminary multi-parameters simulations

The aim of the whole study was to explore the range of ice thicknesses obtained varying the most commonly used parameters within an ice-sheet model. Our study shows that performing univariate experiments leads to a reasonable range of ice volume and ice thickness compared to the existing reconstructions of the Late Saalian Eurasian ice sheet. The aim of the parameter combination experiments is to demonstrate that even changing several parameters in the same simulation can lead to a reasonable ice volume compared to the upper and lower bound of the univariate sensitivity experiments.

We are aware that the three combinations that we describe below are not representative for a whole set of space parameters as investigated in Stone et al. (2010) or Applegate et al. (2012). These experiments are just preliminary simulations in which we tested the parameters that have been found to be the most sensitive given our sensitivity study and given the literature.

In the first combination (experiment F1), we wanted to test the effect of PDD parameters in combination with a threshold for solid precipitation, since the ice sheet was sensitive towards changes in these parameters. In this run, we choose a temperature threshold of 2°C for the conversion of total precipitation into snow, which reduces the amount of accumulation compared with the reference simulation. In addition, we reduce the standard deviation of the daily temperature cycle,  $\sigma$ , from 5°C to 4.5°C and increase the amount of refreezing. Both changes in PDD parameters induce a decrease in ablation compared with the reference simulation. The combined data set of geothermal heat flux from Shapiro and Ritzwoller (2004) and Näslund et al. (2005) is used in experiment F1, which provides a high-resolution GHF distribution over Sweden and Finland (see Table 4-6 for the choice of parameters). The parameter combination in experiment F1 leads to a slightly smaller Eurasian ice volume by 0.4 and 0.2 m SLE compared with REF\_Topo1 and REF\_Topo2, respectively. The ice thickness over Forsmark reduces by ~60 m compared with the reference simulation using B140\_Topo1 forcing, whereas it increases slightly by ~25 m in the case of B140\_Topo2 forcing (Figure 4-22 and Table 4-7). Compared with REF\_Topo1, imposing a temperature threshold for the conversion of total precipitation into snow slightly reduces the amount of accumulation, particularly along the south-western margin of the Eurasian ice sheet where summer temperatures are positive (Figure 4-23g). Consequently, the ice sheet loses mass particularly in these areas (Figure 4-23a). Due to temperature corrections for elevation changes, the mass loss along the margin leads to warmer surface air temperatures there (Figure 4-23d), and therefore higher ablation (Figure 4-24a). This is a positive feedback. The higher ablation is partly compensated by the choice of a lower  $\sigma$ -value (4.5°C compared with 5°C in the reference simulation) and by a higher amount of refreezing compared with the reference simulation. Using B140\_Topo2 forcing in experiment F1 leads to a lower mass loss in the southern part of the Eurasian ice sheet compared with B140\_Topo1 climate forcing, and consequently the ice thickness over Forsmark does not change significantly compared with the reference simulation (Figure 4-22a). This is due to differences between the two climate forcings B140\_Topo1 and B140\_Topo2 (Figure 4-7), which leads to a slightly different response of the ice sheet to changes in model parameters.

**Table 4-6. List of parameters used in sensitivity experiments exploring parameter combinations (F1, F2 and F3). Parameters, which deviate from reference default values, are highlighted.**

Parameter	Unit	Default value	Exp. F1	Exp. F2	Exp. F3
<b>Climate forcing</b>					
$\lambda_{Ann} / \lambda_{July}$	°C/km	5 / 4	5 / 4	5 / 4	5 / 4
$\gamma$	°C <sup>-1</sup>	0.05	0.05	0.03	0.05
$p_{solid}$	°C	–	2	2	2
<b>PDD parameters</b>					
$C_{ice} / C_{snow}$	mm/d/°C	8 / 3	8 / 3	8 / 3	8 / 3
$\sigma$	°C	5	4.5	5.5	5
csi	%	60	70	70	60
<b>Ice stream areas</b>					
$h_{sed}^* / h_w^*$	m	150 / 250	150 / 250	150 / 250	150 / 250
sediment thickness		Laske and Masters 1997	Laske and Masters 1997	Laske and Masters 1997	Laske and Masters 1997
$c_f$	–	$2 \cdot 10^{-5}$	$2 \cdot 10^{-5}$	$3 \cdot 10^{-5}$	$3 \cdot 10^{-5}$
<b>Ice shelf areas</b>					
$H_{calv}$	m	200	200	200	200
$b_{melt}$ (above/below 450 m)	m/yr	0.2 / 2.45	0.2 / 2.4	0.2 / 2.45	0.2 / 2.45
<b>Solid earth</b>					
$T_r$	kyrs	3,000	3,000	3,000	3,000
GHF	mW/m <sup>2</sup>	Shapiro and Ritzwoller 2004	Shapiro and Ritzwoller 2004 and Näslund et al. 2005	Shapiro and Ritzwoller 2004 and Näslund et al. 2005	Shapiro and Ritzwoller 2004 and Näslund et al. 2005

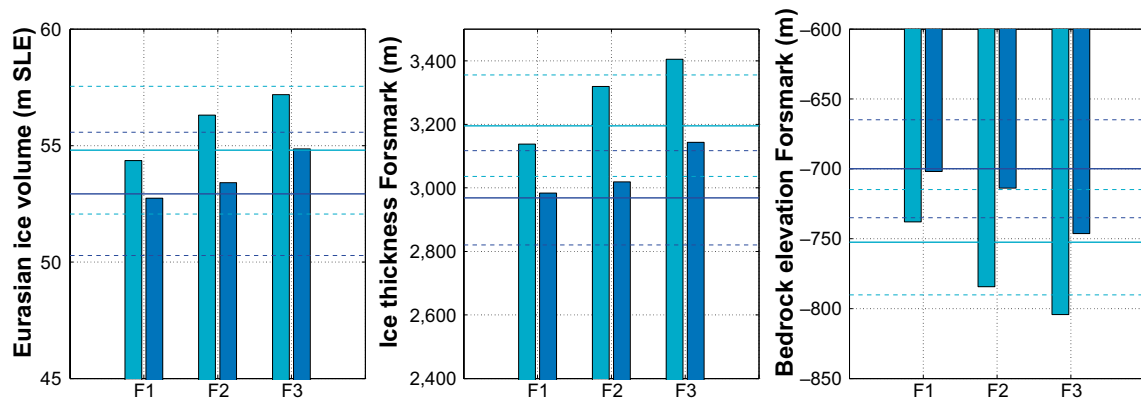


**Figure 4-22.** Eurasian ice volume (left), ice thickness in Forsmark (middle) and bedrock elevation in Forsmark (right) of experiments F1, F2 and F3 using B140\_Topo1 forcing (cyan) and B140\_Topo2 forcing (blue) at the end of the simulations. The cyan and blue lines indicate the reference simulations REF\_Topo1 and REF\_Topo2, respectively (Figure 4-9). The dashed cyan and blue lines indicate  $\pm 5\%$  of the respective reference simulation.

In the second combination (experiment F2), we explore the impact of higher basal drag compared with the reference value, in combination with a higher standard deviation of the daily temperature, a higher refreezing rate and lower accumulation by reducing the precipitation correction factor and by prescribing a temperature threshold of  $p_{solid} = 2^{\circ}\text{C}$  for the conversion of total precipitation into snow. Again, the combined data set of geothermal heat flux from Shapiro and Ritzwoller (2004) and Näslund et al. (2005) is used (Table 4-6). Using a higher basal drag leads to an increase in Eurasian ice volume by  $\sim 3.9$  m SLE and  $\sim 3.7$  m SLE compared with REF\_Topo1 and REF\_Topo2, respectively (Experiment C4, Figure 4-13 and Table 4-4). In experiment F2, the lower accumulation rate (smaller precipitation correction factor compared with the reference simulation and  $p_{solid} = 2^{\circ}\text{C}$ ) and the higher standard deviation of the daily temperature cycle counteract the increase in basal drag, as well as the increase in refreezing, therefore leading to a moderate increase in Eurasian ice volume by  $\sim 1.5$  m SLE and  $\sim 0.5$  m SLE compared with REF\_Topo1 and REF\_Topo2 (Figure 4-22 and Table 4-7). The increase in ice thickness is particularly strong in the central and eastern part of the ice sheet, i.e. ice stream areas, mainly due to lower sliding velocities (Figure 4-24h). In contrast, the south-western margin loses mass (Figure 4-23b) as a result of the decrease in accumulation along the margin (Figure 4-23h) and the increase in ablation (Figure 4-24b).

**Table 4-7.** Final Eurasian ice volume (m SLE), ice thickness (m) and bedrock depression in Forsmark (m) for the six multivariate sensitivity experiments exploring parameter combinations performed on the Eurasian 20 km grid. For each value, the change relative to the respective reference experiments (REF\_Topo1 and REF\_Topo2) is also given (in %).

Run id	Eurasian ice volume				Ice thickness, Forsmark				Ice thickness, Forsmark			
	Topo1		Topo2		Topo1		Topo2		Topo1		Topo2	
	[m SLE]	[%]	[m SLE]	[%]	[m]	[%]	[m]	[%]	[m]	[%]	[m]	[%]
REF	54.8		52.9		3,196		2,969		-752		-700	
F1	56.3	2.7	53.4	0.9	3,319	3.9	3,019	1.7	-784	4.2	-714	2.0
F2	57.2	4.4	54.9	3.6	3,405	6.5	3,144	5.9	-804	6.8	-746	6.6
F3	54.4	-0.8	52.7	-0.4	3,138	-1.8	2,984	0.5	-738	-1.9	-702	0.3

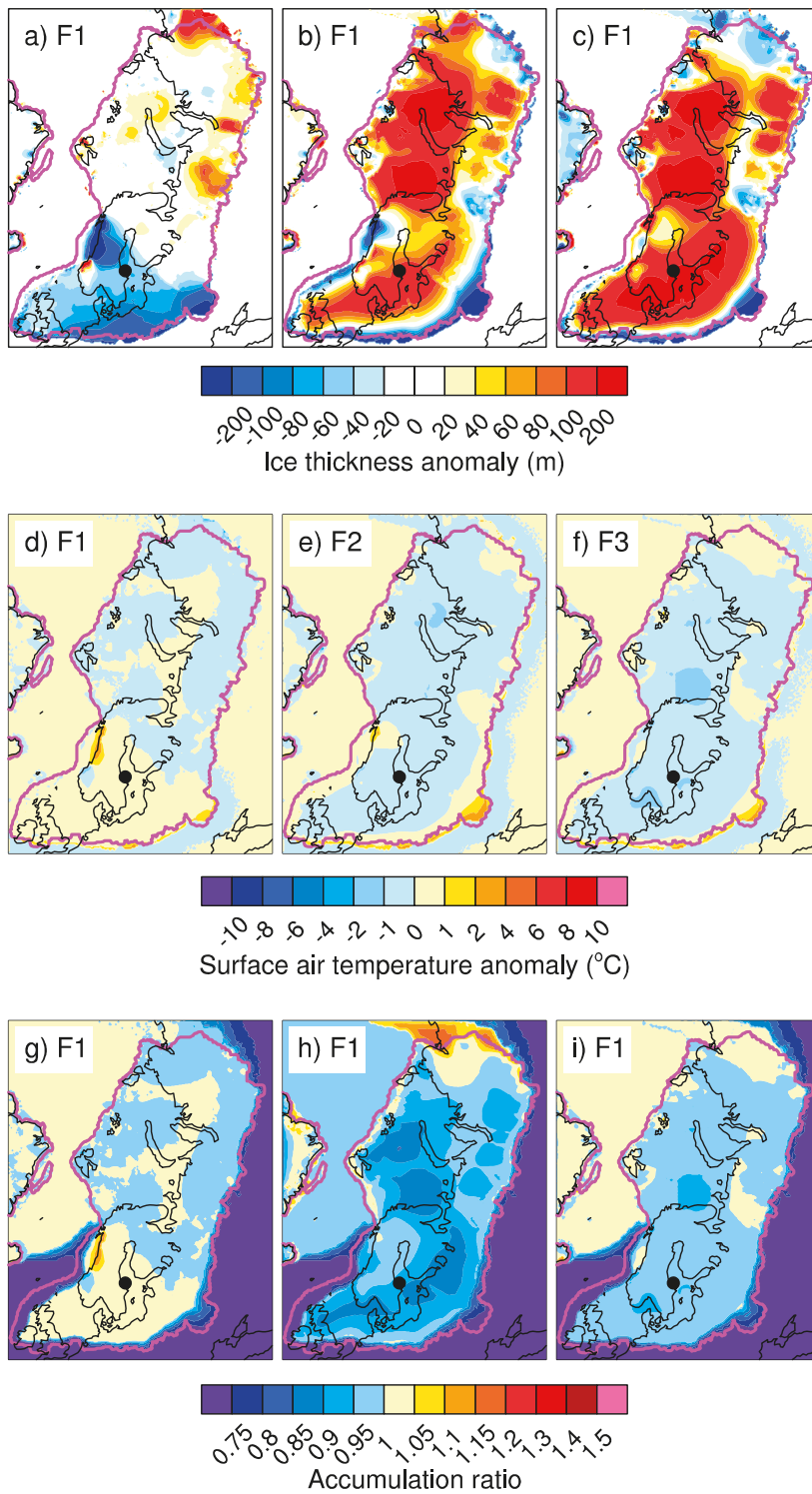


**Figure 4-23.** Impact of parameter combinations: Difference in ice thickness (a, b, c), mean annual temperature (d, e, f) and accumulation (g, h, i) between experiments F1 (left panel), F2 (middle panel) and F3 (right panel) and the reference experiment REF\_Top1 at the end of the simulation (sensitivity experiments minus (or divided by) reference experiment). The black dot indicates the Forsmark site, and the magenta line indicates the extent of the reconstructed Late Saalian ice sheet from Peyaud (2006). See Appendix 3 for the figures using B140\_Top2 forcing.

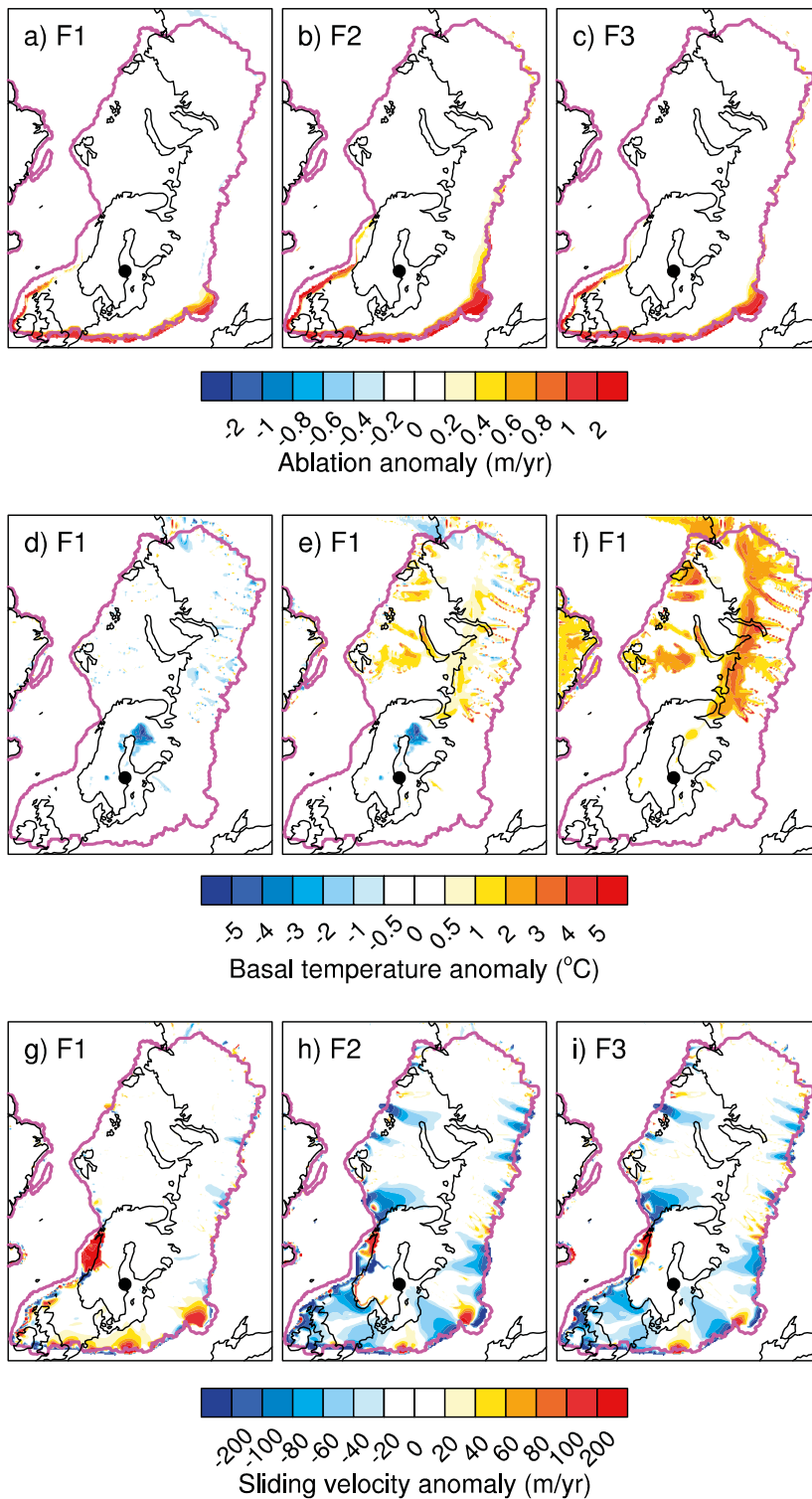


**Figure 4-24.** Impact of parameter combinations: Difference in ablation (a, b, c), basal temperature relative to the pressure melting point (d, e, f) and sliding velocity (g, h, i) between experiments F1 (left panel), F2 (middle panel) and F3 (right panel) and the reference experiment REF\_Top01 at the end of the simulation (sensitivity experiments minus (or divided by) reference experiment). The black dot indicates the Forsmark site, and the magenta line indicates the extent of the reconstructed Late Saalian ice sheet from Peyaud (2006). See Appendix 3 for the figures using B140\_Topo2 forcing.

With the third combination (experiment F3) we investigate the impact of higher basal drag combined with higher geothermal heat flux. PDD parameters are set to reference values, whereas accumulation is slightly decreased by imposing a temperature threshold of 2°C for the conversion of total precipitation into snow (Table 4-6). In experiment F3, the effect of lower accumulation ( $p_{solid}=2^{\circ}\text{C}$ ) and of a warmer base (GHF increased by 10%) is partly compensated by an increase in basal drag relative to REF\_Topo1 and REF\_Topo2. As a result, the overall Eurasian ice volume in experiment F3 is subject to a strong increase compared with the reference simulation, which is however less strong than in experiment C4 (which investigated the response to an increase in basal drag). The Eurasian ice volume increases by 2.1 m SLE and 2 m SLE, while ice thickness over Forsmark increases by ~200 m and ~180 m compared with REF\_Topo1 and REF\_Topo2 (Figure 4-22 and Table 4-7). As in experiment F2, the ice sheet gains mass in the central and eastern part, and loses mass along the south-western margin (Figure 4-23c).

In multivariate experiments we did not vary lapse rates, as we found out that lapse rates of 5°C/km and 4°C/km for annual mean and July surface air temperatures, respectively, are well motivated parameters for our climate forcing (Section 4.4.2). In addition, we did not vary “ice shelf” parameters, since the results in Section 4.4.5 show that the overall simulated Eurasian ice sheet is rather insensitive to changes in these parameters (Section 4.4.5).

## 4.6 Sensitivity experiments: impact of horizontal grid resolution

As previously mentioned, the univariate ice-sheet simulations were performed on two different horizontal grids: Eu20 covers the Eurasian domain and has a horizontal resolution of 20 km, whereas NH40 covers the Northern Hemisphere with a resolution of 40 km. In this section, we analyze the impact of horizontal grid resolution on the simulated Eurasian ice sheet geometry.

When using a resolution of 40 km, the Eurasian ice sheet loses mass, in the case of REF\_Topo1 2.5 m SLE and 3 m SLE in the case of REF\_Topo2 compared the simulation with 20 km resolution. Ice thickness at the Forsmark site reduces by ~200 m (REF\_Topo1) and by ~130 m (REF\_Topo2) compared with the 20 km simulation. The difference in simulated ice thickness between simulations Eu20\_REF\_Topo1 (denoted by REF\_Topo1 in the previous sections) and NH40\_REF\_Topo1 is particularly high along the Norwegian coast (Figure 4-25). There, the surface elevation is very steep. By increasing the grid resolution to 20 km, we are able to better resolve this complex topography. Using a coarser resolution of 40 km leads to a smoother topography, resulting in a stronger ice flow. Resolving the steep topography along the Norwegian coast not only affects the coastal areas, but also large parts of Scandinavia. Similarly, differences in ice thickness are apparent along the south-western margins of the ice sheet (again due to better resolving the steep margins in the Eu20 grid). Using a horizontal resolution of 10 km might even increase ice thickness over Forsmark slightly, since ice thickness is higher when using 20 km resolution instead of 40 km resolution. However, we did not perform experiments with 10 km resolution in this study.

A recent study focusing on the ice sheet-ice shelf transition and using a full-Stokes ice sheet model (Durand et al. 2009) shows that to properly capture the ice dynamics in those steep areas, horizontal grid resolution should be of about 5 km and up to about 200 m at the grounded line. However, a SIA ice-sheet model cannot reach those high resolutions since the assumptions made in this approximation might not be valid anymore. Furthermore, given the computational cost, a full-Stokes model is needed only if the area of interest is located in narrow valleys or nearby the margins. Another approach would be to activate a full-Stokes scheme in areas where the SIA does not hold, and apply the SIA in the remaining regions of the ice sheet. Forsmark is located over an area where, at 20 km resolution, the SIA is used (Figure 4-10), which means that as a first approximation, it would not change the results to much compared with a full-Stokes scheme.

The range of sensitivity experiments that was performed on the Eurasian 20 km grid was also carried out on the Northern Hemisphere 40 km grid. In general, the response to the parameter changes goes in the same direction as for the Eu20 experiments and does not depend on the horizontal resolution of the grid (Figure 4-26). Furthermore, the sensitivity between the reference experiments and the sensitivity test is similar between Eu20 and NH40. The sensitivity of the model is therefore independent of resolution in a qualitative sense. However, resolution affects the magnitude of the simulated ice volume. The difference in ice volume between sensitivity experiments performed on the Eu20 grid and those performed on the NH40 grid can reach 2 m SLE (Table 4-8).

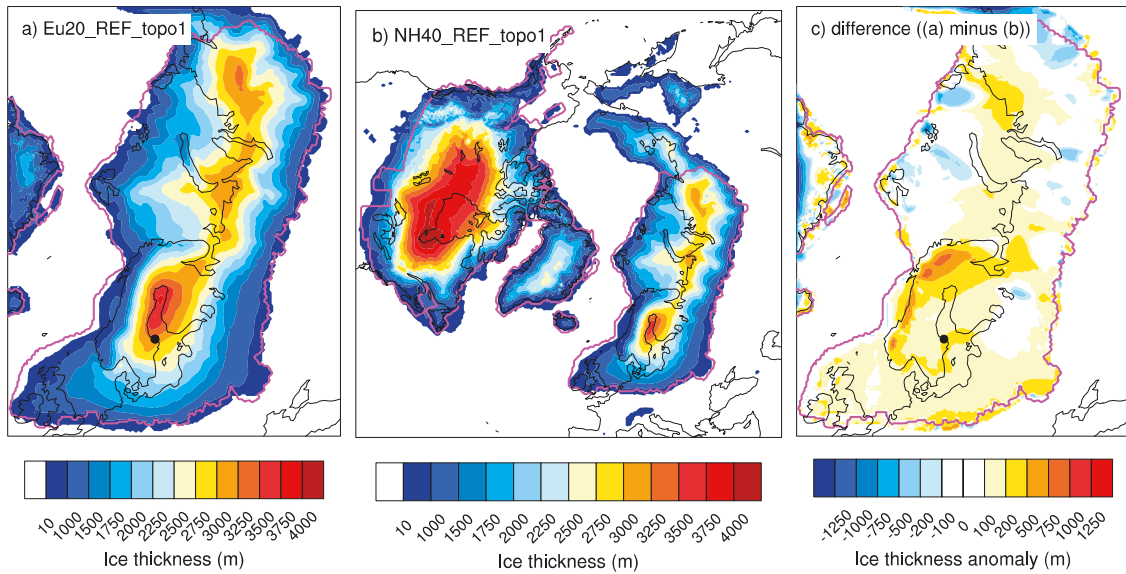


**Figure 4-25.** Impact of grid resolution: Ice thickness of simulations (a) *Eu20\_REF\_Topo1*, (b) *NH40\_REF\_Topo1* and (c) difference (*Eu20\_REF\_Topo1* minus *NH40\_REF\_Topo1*) at the end of the simulation.

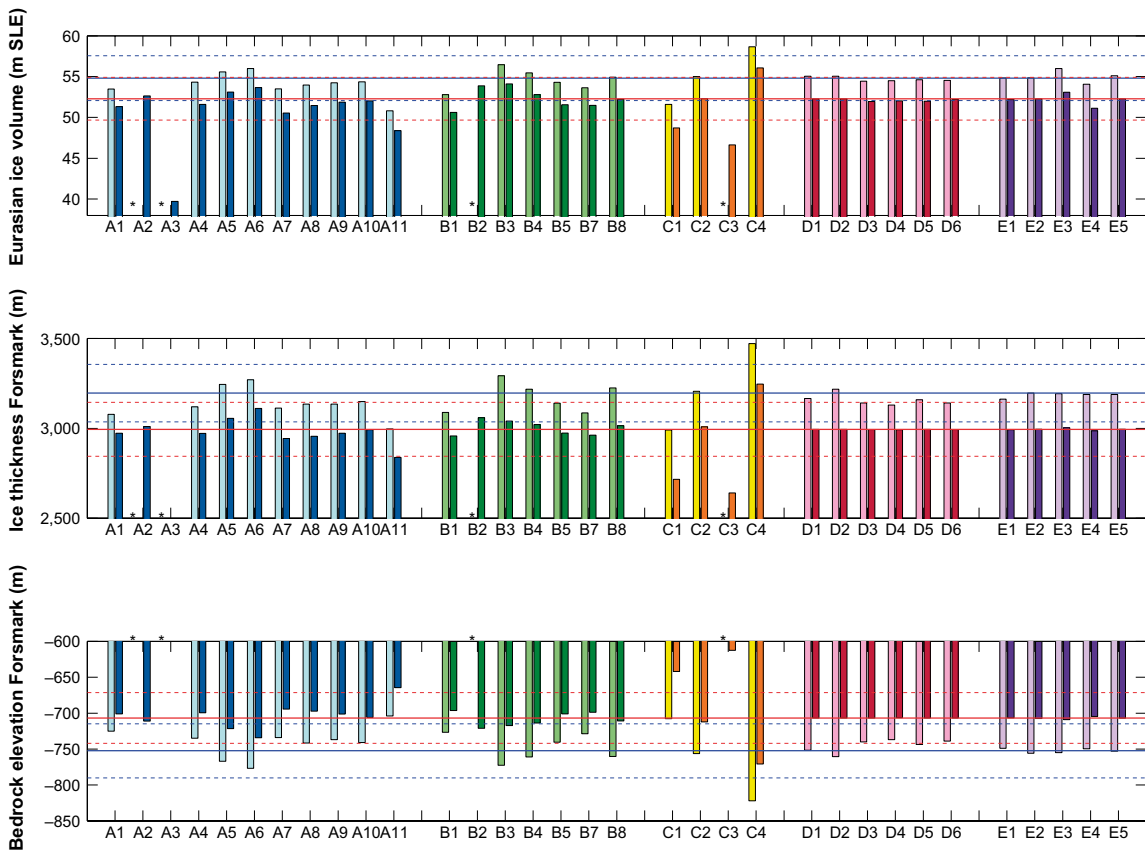


**Figure 4-26.** Eurasian ice volume (top), ice thickness in Forsmark (middle) and bedrock elevation in Forsmark (bottom) of experiments conducted on the *Eu20* grid (light colors) and on the *NH40* grid (dark colors) using *B140\_Topo1* climate forcing at the end of the simulations. The blue and red solid lines indicate the reference simulations *Eu20\_REF\_Topo1* and *NH40\_REF\_Topo1*, respectively. The dashed blue and red lines indicate  $\pm 10\%$  of the respective reference simulation. Stars indicate experiments which could not be conducted on the Eurasian 20 km grid due to numerically unstable behavior of the model.

**Table 4-8. Final Eurasian ice volume (m SLE), ice thickness (m) and bedrock elevation in Forsmark (m) for all sensitivity experiments performed on the Northern Hemisphere 40 km grid. For each value, the change relative to the respective reference experiment is also given (in %). Experiments are grouped according to categories: Climate corrections (A), PDD parameters (B), Ice streams (C), Ice shelves (D) and Solid earth (E). Minimum and maximum values are highlighted.**

Run id	Eurasian ice volume				Ice thickness Forsmark				Ice thickness Forsmark			
	Topo1		Topo2		Topo1		Topo2		Topo1		Topo2	
	[m SLE]	[%]	[m SLE]	[%]	[m]	[%]	[m]	[%]	[m]	[%]	[m]	[%]
REF	52.3		50.3		2,994		2,886		-707		-680	
A1	51.3	-1.8	50.2	-0.1	2,972	-0.7	2,845	-1.4	-701	-0.8	-668	-1.7
A2	52.6	0.7	51.2	1.8	3,010	0.5	2,844	-1.4	-711	0.6	-667	-1.9
A3	39.7	-24.1	35.9	-28.5	0	-100	0	-100	0	-100	0	-100
A4	51.6	-1.3	49.5	-1.5	2,971	-0.8	2,798	-3.0	-699	-1.1	-656	-3.5
A5	53.1	1.5	51.1	1.6	3,055	2.0	2,918	1.1	-721	2.0	-687	1.1
A6	53.7	2.6	52.3	4.0	3,110	3.9	2,985	3.4	-734	3.9	-705	3.7
A7	50.5	-3.3	47.0	-6.6	2,943	-1.7	2,647	-8.3	-694	-1.8	-616	-9.4
A8	51.4	-1.6	48.5	-3.5	2,956	-1.3	2,747	-4.8	-697	-1.4	-641	-5.7
A9	51.9	-0.8	48.9	-2.6	2,973	-0.7	2,771	-4.0	-701	-0.8	-647	-4.8
A10	52.0	-0.5	49.8	-1.0	2,992	-0.1	2,827	-2.0	-706	-0.1	-664	-2.3
A11	48.4	-7.5	45.0	-10.4	2,838	-5.2	2,583	-10.5	-664	-6.0	-598	-12.0
B1	50.6	-3.2	46.8	-7.0	2,958	-1.2	2,676	-7.3	-696	-1.5	-620	-8.8
B2	53.9	3.0	52.7	4.8	3,058	2.1	2,927	1.4	-721	2.0	-691	1.6
B3	54.1	3.5	52.6	4.7	3,040	1.5	2,911	0.9	-717	1.5	-686	0.9
B4	52.8	1.0	51.4	2.2	3,021	0.9	2,878	-0.3	-714	1.0	-678	-0.3
B5	51.5	-1.4	49.1	-2.4	2,974	-0.7	2,811	-2.6	-701	-0.8	-659	-3.1
B7	51.5	-1.6	48.7	-3.2	2,961	-1.1	2,744	-4.9	-699	-1.1	-639	-6.0
B8	52.2	-0.1	50.7	0.8	3,015	0.7	2,859	-0.9	-711	0.6	-673	-1.0
C1	48.7	-6.8	46.1	-8.2	2,715	-9.3	2,488	-13.8	-642	-9.2	-588	-13.5
C2	52.3	0.0	50.0	-0.4	3,009	0.5	2,866	-0.7	-712	0.7	-675	-0.7
C3	46.6	-10.8	45.3	-9.9	2,640	-11.8	2,525	-12.5	-613	-13.3	-583	-14.2
C4	56.0	7.2	53.7	6.8	3,247	8.4	3,073	6.5	-771	9.1	-727	6.9
D1	52.3	0.0	49.9	-0.7	2,994	-0.0	2,844	-1.4	-707	0.0	-668	-1.7
D2	52.3	0.0	49.9	-0.7	2,994	-0.0	2,844	-1.4	-707	0.0	-668	-1.7
D3	51.9	-0.7	49.8	-0.9	2,994	-0.0	2,843	-1.5	-707	0.0	-668	-1.7
D4	52.0	-0.5	49.6	-1.3	2,993	-0.0	2,840	-1.6	-706	-0.1	-667	-1.9
D5	52.0	-0.6	49.7	-1.1	2,994	-0.0	2,841	-1.6	-707	0.0	-667	-1.9
D6	52.2	-0.2	49.8	-0.9	2,994	-0.0	2,840	-1.6	-707	0.0	-668	-1.7
E1	52.2	-0.2	49.8	-1.0	2,993	-0.0	2,842	-1.5	-707	0.0	-668	-1.7
E2	52.3	0.0	49.8	-0.9	2,995	0.0	2,840	-1.6	-707	0.0	-668	-1.7
E3	53.1	1.5	50.7	0.8	3,003	0.3	2,847	-1.3	-709	0.3	-669	-1.6
E4	51.1	-2.2	48.9	-2.7	2,986	-0.3	2,832	-1.9	-704	-0.4	-665	-2.2
E5	52.3	-0.0	49.9	-0.6	2,995	0.0	2,842	-1.5	-707	0.0	-668	-1.7

## 5 Discussion

The aim of this project was to obtain an ensemble of ice thicknesses over the Forsmark area representative of the most extensive glaciation that occurred over Eurasia over the last 400 kyrs based on dated marginal positions, namely the Late Saalian glaciation (~140 kyrs BP). Two climate simulations, representative of the Late Saalian glacial maximum, and accounting for different Laurentide ice sheet extents were carried out using an AOGCM. The climate simulations were used to force off-line a 3D-thermomechanical ice-sheet/ice-shelves model to simulate the Eurasian ice-sheet thickness response to various internal physical parameters and parametrisations changes.

In total, 70 univariate ice-sheet simulations have been run at 20 km resolution over the Eurasian domain and the same number was run at 40 km over the entire Northern Hemisphere. In addition, six multi variate simulations were carried out for both grids. Those results were obtained using specific initial conditions and one particular climate-ice-sheet model combination. Therefore, some hypotheses need to be discussed in detail in order to assess the impact of the results. In particular, we discuss the initial conditions related to ice-sheet extent. The large Late Saalian Eurasian extent is debated in the scientific community, since no clear evidence really defines the chronology of the maximum Saalian ice sheet extent from Svendsen et al. (2004). Another important point deals with the impact of the distribution of vegetation that we used in our climate experiments. The snow-vegetation-albedo feedback is one of the major regional feedbacks substantially acting on the growth of ice sheets at high latitudes. Then we discuss some aspects of the ice-sheet simulations, starting with the impact of the initialization procedure for vertical ice temperature on the final simulated ice sheet geometry, as well as the impact of performing steady-state experiments, then proceeding with the impact of the choice of atmospheric lapse rate. We also discuss the impact that the use of an Energy Balance Model rather than the PDD method could have on our results. Finally we briefly discuss the role of isostasy in our steady-state experiments.

### 5.1 Laurentide and Eurasian ice sheet extents

The Late Saalian glaciation over Eurasia is characterized by two major advances at ~160 kyrs BP and ~140 kyrs BP and a substantial retreat around 150 kyrs BP (mainly due to the large summer insolation peak occurring at this time, Figure 1-1, Svendsen et al. 2004, Astakhov 2004). Colleoni (2009) showed that even though the summer insolation at about 150 kyrs BP seems not favorable to maintain an ice sheet over the Northern Hemisphere high latitudes, the ablation occurring along the southern margins is compensated for by increased accumulation. In the Colleoni (2009) experiments, the Late Saalian Eurasian ice sheet is able to survive this insolation peak. However, geological evidence shows that a major retreat occurred at ~150 kyrs BP. If we consider that the Late Saalian extent from the QUEEN project corresponds to MIS 6 glacial maximum at ~140 kyrs BP, this left only 10 kyrs for the Eurasian ice sheet to regrow to this large extent. This timing does not seem reasonable and suggests that the major extent could have been reached at different moments of the cycle rather than at the MIS 6 glacial maximum, towards 140 kyrs BP. This hypothesis appears to be reasonable if compared to the last glacial cycle, which results in larger Eurasian ice-sheet extents over Eastern Siberia at the beginning of the cycle, i.e. ~85 kyrs BP or ~60 kyrs BP, than at the Last Glacial Maximum, where most of the Eurasian ice sheet developed over Western Europe.

The fact that only indirect evidence of glacial dynamics during MIS 6 exists for North America appears to be a strong limitation to computing a well-defined MIS 6 Northern Hemisphere climate. In a first phase, we considered an extreme Late Saalian glaciation case for which the Northern Hemisphere ice topography is composed of the Eurasian ice sheet from Peyaud (2006) and the Laurentide ice sheet prescribed from LGM ICE-5G (Peltier 2004). Since no geological evidence supports this extreme MIS 6 ice-sheet configuration, we also chose to prescribe a smaller ice sheet over North America from Peltier (2004) to investigate the impact that the Laurentide ice sheet has on the Eurasian climate (Figure 3-1). This second topography appears to be more in line with paleo proxies and is also less extreme than the first glacial topography that we used. Those considerations are further supported by two main lines of evidence:

- Ice-rafted debris records from the Hudson Bay area (de Abreu et al. 2003, Channell et al. 2012) reveal that the fluxes of icebergs from the Laurentide ice sheet during the MIS 6 glacial maximum were much lower than during the LGM. This is a clear indication that ice dynamics was reduced compared with those of the LGM, implying that the Laurentide ice sheet might have been smaller than at the LGM.
- A small Laurentide ice sheet induces the accumulation of a thick perennial snow cover over the East Siberian continental shelf, more extended than when using the LGM Laurentide topography. This result is supported by recent evidence for the existence of a thick ice cap over the Beringia area during the Pleistocene glaciations (Jakobsson et al. 2010, Niessen et al. 2013). However, no ice cap developed over Beringia during the LGM. This fact is particularly important since, at the LGM, the Eurasian ice sheet was smaller than at ~140 kyrs BP. All together, these facts suggest that to grow an ice cap over the East Siberian shelf, both a small Laurentide and a large Eurasian ice sheet (extending far to the East) are necessary.

The two climate simulations that we carried out are useful to constrain the Northern Hemisphere Late Saalian ice-sheet topography. Given the lack of geological constraints, the southern extent of the Late Saalian Eurasian ice sheet reconstruction from Peyaud (2006) might be more questionable since it is highly sensitive to summer climate in our simulations. The two climate simulations B140\_Topo1 and B140\_Topo2 suggest that to stay in line with past sea-level reconstructions, ice-rafted debris reconstructions and Arctic ice caps, the Laurentide ice sheet has to be substantially smaller than during the LGM. In Topo2, we used a Laurentide ice-sheet reconstruction from Peltier (2004) of about 30 m SLE, i.e. corresponding to the deglaciation period at about 13 kyrs BP. It seems that, for the investigated MIS 6 period, this more restricted Laurentide ice-sheet topography is more realistic than the LGM one. It could be useful to perform a transient climate-ice-sheet simulation to grow a proper MIS 6 Laurentide ice sheet and understand what would be the ice elevation threshold over North America that would affect circulation just enough to allow for the build up of an ice cap over Beringia.

## 5.2 Vegetation distribution

In our climate simulations, the vegetation has been prescribed to a pre-industrial distribution and the areas that are ice-covered have been declared as the “glaciated” land type in the CESM land component. The impact of the simulated Late Saalian vegetation cover has been investigated in Colleoni et al. (2009a). They showed that due to the extremely cold climate induced by the Late Saalian ice-sheet topography, forests retreat southward, which leads to a regional cooling of about 10°C to 15°C, strengthening the stability of the southern margin of the Late Saalian Eurasian ice sheet. This corresponds to the snow-albedo-vegetation feedback (de Noblet et al. 1996, Crowley 1995). However, Colleoni et al. (2009a) used an AGCM with prescribed LGM sea-surface temperatures, that is temperatures not in agreement with the Late Saalian climate. To rectify this, Colleoni et al. (2010) simulated the SST for the Late Saalian glacial maximum using an ocean mixed-layer coupled to a simplified AGCM. The resulting simulated SSTs were by far too cold and unrealistic in the northern high latitudes. In fact, the sea-ice cover reached the Iberian peninsula during spring, whereas SST proxies suggest that the sea-ice cover was similar to that of the LGM, i.e. expanded until Iceland but let the North Atlantic ice-free during part of the winter and during summer. Nevertheless, Colleoni (2009) showed that prescribing those extreme Late Saalian SST leads to an additional drop in local temperature of about 8°C compared to when using prescribed LGM SST as in Colleoni et al. (2009a). As a consequence, the forest retreats further to the South compared to what was found by Colleoni et al. (2009a), and is substituted by tundra-type vegetation. In addition, a perennial snow cover accumulates all along the southern margin of the Late Saalian Eurasian ice sheet, which was not the case in Colleoni et al. (2009a).

The above findings suggest that if we compute the dynamical vegetation in our Late Saalian simulations, forests would retreat further south compared to the pre-industrial vegetation distribution. Those changes in vegetation cover would lead to an additional regional cooling along the southern and eastern margins of the Eurasian ice sheet. At odds with Colleoni et al. (2009a), our simulated sea-surface temperatures are very similar to LGM temperatures and are in line with the proxy data (Figure 3-3), which indicates that the location of polar front is properly captured by the CESM in the North Atlantic. In our simulations, the sea-ice edge in the North Atlantic remains off Iceland and does not expand southward (Figure 3-8). Therefore, using dynamic vegetation would not lead

to a drop in temperature as large as in Colleoni (2009) over central Russia and Eastern Siberia, i.e. of about 20°C, but to a drop of about 10°C, as simulated in Colleoni et al. (2009a). However, this does not imply that the simulated Eurasian ice sheet would expand further southward. In fact, the simulated perennial snow cover resulting from the southward retreat of the forests in Colleoni et al. (2009a) remains restricted to the marginal areas and does not expand further south.

### 5.3 Initialization of ice-sheet simulations and assumption of steady-state simulations

A continental-size ice sheet is characterized by a long-term memory of climate conditions, which affects the thermo-mechanical response on a long time scale due to the diffusion and the advection of heat from the ice sheet surface to the base, linked with mechanical deformation within the ice sheet itself. As a consequence, performing a realistic simulation of ice sheet evolution during a given period of time requires knowledge of both the past and the contemporaneous climate conditions. This fact underlines the need to properly spin-up the ice-sheet model to obtain a realistic representation of the vertical temperature distribution within the modeled ice sheet. To initialize the thermodynamical state of an ice sheet, two methods are commonly used, namely transient simulations driven by paleoclimate reconstructions of temperature and precipitation through time, or alternatively steady-state simulations forced by simulated climate conditions at a given time (Rogozhina et al. 2011, and references therein). The spin-up is usually performed over one or two glacial cycles, i.e. about 100 to 200 kyrs. This seems reasonable since the present-day ice temperature of the Greenland ice sheet is still affected by the climate conditions from the penultimate glacial cycle (Calov and Hutter 1996).

There are two ways of starting a spin-up simulation, either using a prescribed ice-sheet topography or start from an ice-free topography (relaxed from isostasy). Rogozhina et al. (2011) showed that using ice-covered topography for Greenland shortens the spin-up time required to bring temperatures and velocities to equilibrium. Moreover, they found that the thermodynamic state of an ice-free topography is strongly dependent on initial air temperatures. In particular, they showed that using glacial climate forcing is not favorable to the growth of Greenland from an ice-free topography since it affects substantially the thermodynamics of the whole ice body, which leads to an underestimate of the final Greenland ice volume compared with observations. Finally, they conclude that the use of steady-state simulation as the initialization technique to model present-day Greenland leads to an overall warmer thermodynamic state than when performing transient simulations.

In this project, we initialized our simulations starting from an ice-covered topography, i.e. using the Late Saalian Eurasian ice-related topography variables. The ice temperature at the beginning is set to 0°C and heat slowly diffuses from the surface, forced by surface air temperature from one of our two climate simulations as the boundary conditions. We then run those experiments for at least 200 kyrs. To understand what could have been the impact of initializing from an ice-free topography following Rogozhina et al. (2011), we carried out an experiment in which we used the present-day ice-free topography to spin-up the Late Saalian Eurasian ice sheet. Both experiments, i.e. starting from an ice sheet topography and from a ice-free topography reach equilibrium after about 70 kyrs (Figure 5-1) and the ice thickness distribution reached after spin-up is, in both cases, similar (Figure 5-2a and 5-2b). This indicates that after 70 kyrs of integration, our final ice topography is independent of the initial topography. Compared with the initial ice volume, the final simulated spin-up ice volume in both simulations is less by about 12 m SLE. This strengthens the conclusions of Rogozhina et al. (2011) who stated that steady-state spin-up using glacial climate forcing leads to an underestimate of the overall ice volume. In the experiment R3, we started from an ice-free topography, i.e. present-day but downscaling the climate forcing to present-day topography (at odds with R2). As displayed in Figure 5-2c, the Eurasian and Laurentide ice sheets did not grow. This is due to the downscaling of the simulated climate on the present-day grid of our ice-sheet model. In fact, the climate that we simulated was computed at ice sheets elevation (ice sheets were prescribed in both climate simulations). To start from an ice-free topography, this climate has to be downscaled to the ice-sheet grid elevation. Therefore, downscaled temperatures increase substantially, which inhibits the growth of both Eurasian and Laurentide ice sheets, except over high mountain ranges, such as the Cascades (Figure 5-2c). This kind of initialization is therefore unrealistic in the context of a glaciation starting from prescribed ice sheets since we are unable to regrow the original ice topography.

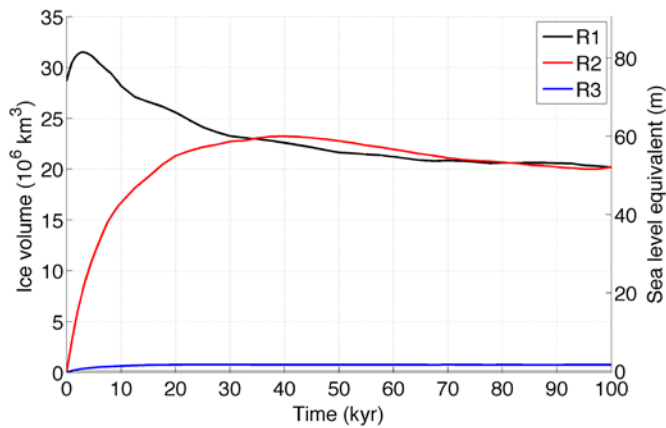


**Figure 5-1.** Eurasian ice volume after 100 kyrs of spin-up. R1 corresponds to spin-up initialized with prescribed Late Saalian ice sheet topography, R2 corresponds to spin-up initialized from present-day topography and R3 corresponds to spin-up initialized from present-day topography and allowing for temperature corrections during runtime using a lapse rate of 8°C/km and 6.5°C/km. In R1 and R2 on the contrary, we did not allow temperature corrections for elevation changes since we wanted to observe the impact of initial topography on the ice sheet geometry. Simulations were forced using B140\_Topo1 surface air temperature and total precipitation and run on the 40 km Northern Hemisphere grid.

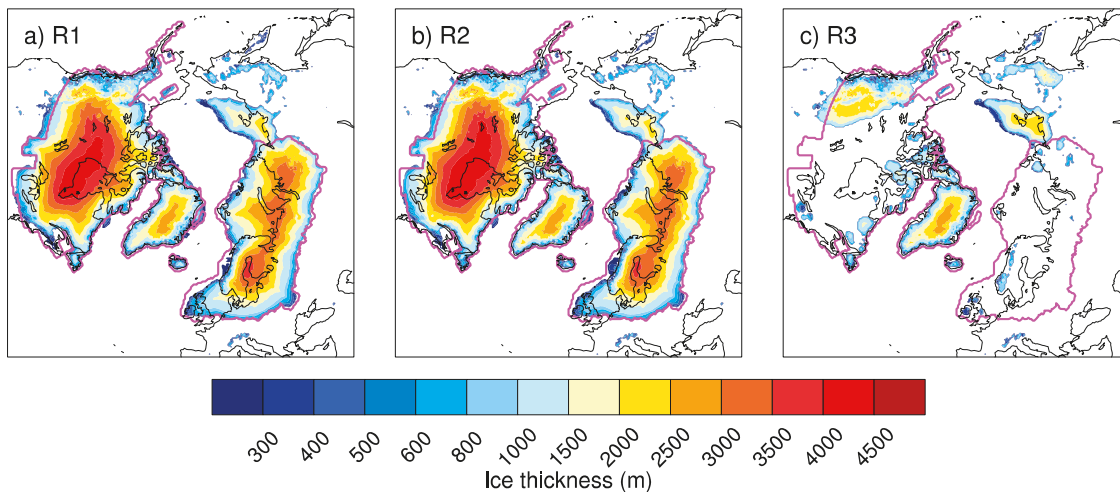


**Figure 5-2.** Final ice thickness distribution (meters) from the three reference runs displayed in Figure 5-1, obtained after 100 kyrs of integration. a. R1 corresponds to spin-up initialized with the prescribed Late Saalian ice sheet topography of Peyaud (2006), b. R2 corresponds to spin-up initialized from present-day topography and c. R3 corresponds to spin-up initialized from present-day topography and allowing for temperature corrections during runtime using a lapse rate of 8°C/km and 6.5°C/km.

In our project, our spin-up Late Saalian Eurasian ice sheet reaches a total ice volume of about 55 m SLE. This is 25% less than in the original reconstruction from Peyaud (2006). There is no direct evidence of the Late Saalian ice volume and the only two reconstructions that existed before the present study are the ones from Peyaud (2006) and Lambeck et al. (2006). The latter study corresponds to a simulated ice volume of about 60 m SLE, which is close to what we obtain in the present project. Lambeck et al. (2006) used a climate model and an ice-sheet model to reconstruct the Late-Saalian – Weichselian evolution of the Eurasian ice sheet. As a consequence, their method provide more robust results than the one by Peyaud (2006). The fact that our simulated Late Saalian Eurasian ice sheet presents a volume comparable to that of Lambeck et al. (2006) is a clear improvement with respect to the original ice topography by Peyaud (2006). Based on the study by Rogozhina et al. (2011), our spin-up simulations might in any case underestimate the final Late Saalian ice volume, since we start from glacial conditions that have very low precipitation rates. The fact that

we account for climate corrections during runtime further strengthens the lack of precipitation by decreasing it as topography increases. In nature, ice sheets do not reach equilibrium under a given climate state, as in our simulations, furthermore the ice sheets start growing under climate conditions that are not fully glacial, i.e. not such cold temperatures and larger precipitation rates. Therefore, during the first thousands of years, the ice-sheet growth is in general quicker than at the end, when climate has become cold and dry. The fact that we initialize our ice simulations using glacial climate conditions might lead to an underestimation of the ice volume of the Late Saalian Eurasian ice sheet, and the length of the simulations might not totally compensate for it. In fact, running a long simulation prescribing very low precipitation from the beginning might lead to a smaller ice volume than running it transiently for 100 kyrs but starting from interglacial wet climate conditions and finishing with glacial dry climate conditions. The only way of precisely assessing the potential underestimation is to perform a transient climate-ice-sheet simulation, to avoid the problems linked with this steady-state initialization.

## 5.4 Atmospheric lapse rates

Our ice-sheet simulations show that the lapse rate values most appropriate to the glaciation over Eurasia are  $5^{\circ}\text{C}/\text{km}$  for mean annual temperature correction and  $4^{\circ}\text{C}/\text{km}$  for summer temperature correction. Those values are in agreement with Abe-Ouchi et al. (2007) who performed a systematic regression between flat and ice topographies under glacial climate conditions. They concluded that lapse rates of about  $5^{\circ}\text{C}/\text{km}$  are the most appropriate when simulating past glaciations. This is also supported by Marshall et al. (2007) who found near-surface lapse rate values of about  $4.7^{\circ}\text{C}/\text{km}$ . However, it is interesting to note that using a standard set of lapse rate values of about  $8^{\circ}\text{C}/\text{km}$  and  $6.5^{\circ}\text{C}/\text{km}$ , the Late Saalian Eurasian ice sheet is not able to grow as large as Svendsen et al. (2004) suggest (Figure 5-3). In contrast, the Laurentide ice sheet appears to be less sensitive to the choice of the lapse rate values both in the case of Topo1 and Topo2. Note that with low lapse rate values, ice spreads over the whole Eastern Siberia in the Topo2 experiment because during summer, the correction performed based on elevation is small (not shown). Therefore, the impact of snow melting is reduced. On the contrary, high lapse rate values limit the growth of ice over East Siberia and Alaska both in the Topo1 and in Topo2 experiments.

The fact that our Late Saalian Eurasian ice sheet is sensitive to the choice of lapse rate values is because the southern margins reach latitudes down to the Black Sea. Therefore, the  $0^{\circ}\text{C}$  isotherm reaches the southern margins during the summer (Figure 4-7d and 4-7e). As previously explained, the diffusion of summer temperature-induced heat from the surface to the base leads to a large amount of meltwater at the base of the ice sheet. In fact, the temperature at the base in the experiments using large lapse rate values reaches the pressure melting point very quickly. As a consequence, most of the ice column is melting away and never grows again because of the temperature-elevation feedback. In general, the Eurasian ice sheet has been demonstrated to be more sensitive to temperature than the Laurentide (Bonelli et al. 2009, Beghin et al. 2014).

## 5.5 Surface mass balance

To simulate the surface mass balance of the Late Saalian Eurasian ice sheet, GRISLI uses the Positive Degree Day method (Section 4.1.7, Reeh 1991). The PDD method calculates ablation by means of a statistical method based on the reconstruction of the temperature annual cycle using mean annual and July air surface temperatures. Originally calibrated on Greenland present-day observations, it has been largely used in the ice-sheet community since this method is not demanding in terms of numerical resources and only requires air surface temperature as the input climate field. Recent studies focusing on the reconstruction of the long-term memory of Greenland pointed out that the PDD method overestimates the effect of warm temperatures and therefore is not optimal to simulate past and future interglacials (Bougamont et al. 2007, Robinson et al. 2012, for examples about Greenland ice sheet). To improve past and future ice-sheets simulations, surface energy balance models, accounting for a larger number of climate processes, and in particular the impact of insolation and albedo on the snowpack accumulating on the top to the ice sheets, were developed over the last decades. In a recent study, the comparison between the two methods shows that the PDD method is more sensitive to warm

climates than the surface energy balance model (Bougamont et al. 2007). In Bougamont et al. (2007), the main difference between the two methods is caused by the amount of meltwater produced during the simulation as well as the amount of refreezing occurring within the snowpack. This later feature is not accounted for in the PDD method and potentially represents an important limitation of ice-sheet modeling using the PDD method.

In defense of the PDD method, Charbit et al. (2013) explored the impact of the standard deviation of daily temperature in coupled climate-ice-sheet models. The authors explored the impact of the PDD parameters, such as  $C_{snow}$  and  $C_{ice}$  and the standard deviation of the daily temperature  $\sigma$ . They showed that using a dependence relationship between those two coefficients and temperature only has a minor impact on the ice volume and extent of the ice sheet over the last glacial cycle. Conversely, they showed that the temperature variability has a large impact on the surface mass balance of the ice sheets and especially during the glacial inception period, when the ice sheets are vulnerable to changes in regional climate. From the various PDD models tested, the one of Fausto et al. (2009), in which  $\sigma$  depends on altitude, gives the best representation of the LGM ice sheet geometry. Finally one of the most important points deals with the refreezing part of the PDD model which requires substantial improvements to better account for the mechanism acting within the snowpack, as in the surface energy balance model.

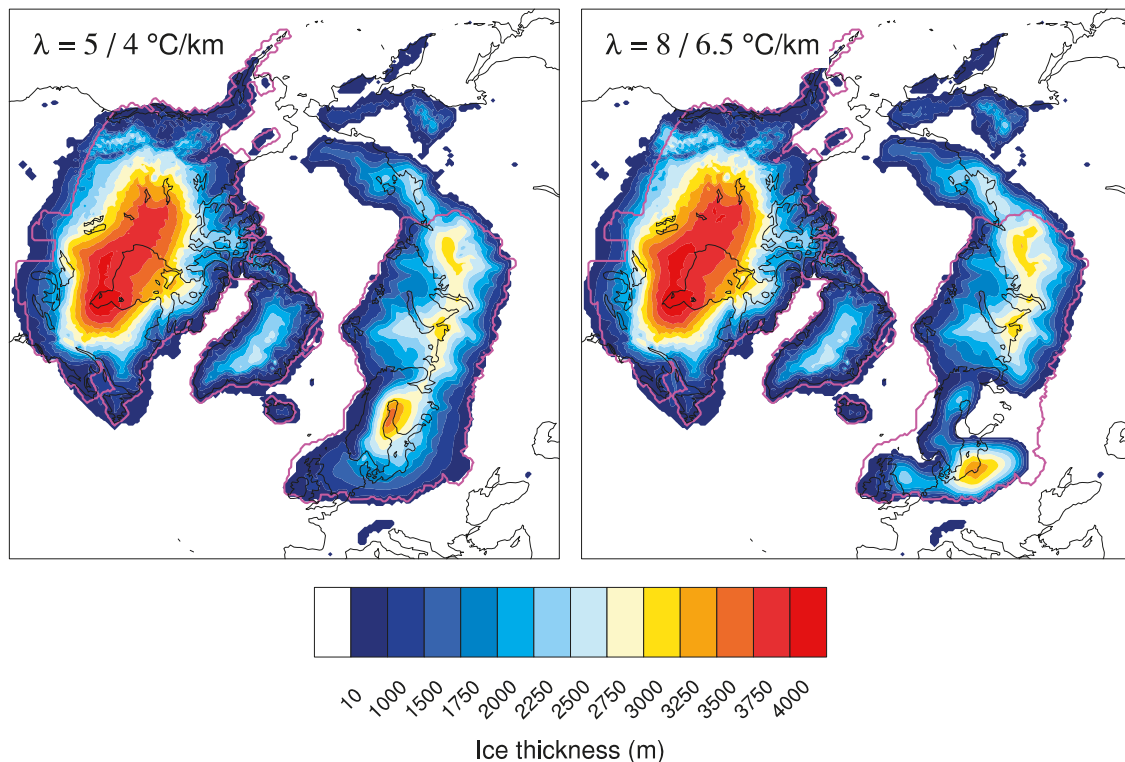


**Figure 5-3.** Impact of lapse rate ( $\lambda$ ) on the topography of the Northern Hemisphere ice sheets. Left frame: lapse rate values were set to  $5^\circ\text{C}$  for mean annual temperature correction and  $4^\circ\text{C}$  for July temperature correction, following Abe-Ouchi et al. (2007). Right frame: lapse rate value were set to  $8^\circ\text{C}$  and  $6.5^\circ\text{C}$  for mean annual and summer temperature, respectively. Simulated ice sheets are obtained after 450 kyr years of integration starting from prescribed ice sheet distribution from Topo1 (Figure 3-1a). Magenta contours correspond to Topo1 initial Late Saalian ice sheet distribution.

In our simulations, the PDD parameters, such as  $\sigma$  and  $C_{snow}$  and  $C_{ice}$  have been prescribed. But we did not test a parametrization relating the melting coefficients to temperature, or relating the standard deviation to elevation changes. Note that our simulations in general do not produce a large amount of ablation. Therefore, although it would be desirable to test different PDD models, the fact that we have focused on glacial climate simulations, using steady-state forcing, might also decrease the sensitivity of the Eurasian ice sheet to such an alternative representations. In contrast, the use of an energy balance model could increase the sensitivity by giving a better representation of the impact of insolation and albedo on the snowpack layer and therefore on the refreezing within the snowpack itself. However, the energy balance models are numerically more demanding than the PDD method and therefore, it requires a special attention and a careful study of the processes to be simulated before implementing this kind of scheme in GRISLI.

## 5.6 Isostasy

In GRISLI, the isostasy is calculated using an elastic lithosphere-relaxed asthenosphere model, which has been proven to give similar results to a self-gravitating Earth model (Le Meur and Huybrechts 1996). However, a recent contribution by van den Berg et al. (2008), focusing on the Eurasian ice sheet during the last glacial cycle, showed that when using a fully self-gravitating Earth model, the Eurasian ice sheet is sensitive to the choice of the characteristic relaxation time for the asthenosphere, affecting the accumulation of ice through the elevation-climate feedback. They also showed that a simple local flexural model leads to an underestimation of the ice-sheet volume for the LGM. However, van den Berg et al. (2008)'s study was performed using a transient climate forcing, which is associated with more sensitivity of the ice sheet during the accumulating phase (Rogozhina et al. 2011). In our project, on the contrary, we performed steady-state experiments, forced by steady-state climates. As shown in Figure 4-25 and in Figure 4-26, starting from an ice-free topography (no initial loading) does not result in more sensitivity than starting from prescribed ice sheet topography (already depressed and in isostatic equilibrium). This is due on one hand to the fact that we are forcing our simulations with a glacial climate, which limits ablation to the southern margins of the ice sheet exclusively. As a consequence, changing the characteristic time does not impact on the final simulated ice volume and ice thickness. Additionally, the integration time of our steady-state experiments largely compensates for the initial relaxation after only 30 kyrs (Figure 4-25).

Depending on the objectives of the ice-sheet simulations, using a full self-gravitating model only matters if the intent is to reconstruct the chronology of extent of the ice sheets, i.e in the case of transient simulations. For steady-state experiments, as shown by Le Meur and Huybrechts (1996), a regional flexural model is sufficient to provide well-justified results in terms of maximum bedrock depression.

## 6 Conclusions

In this study, we performed ice-sheet simulations with topography and climate boundary conditions representative for the Late Saalian glaciation. We investigated the impact of two different sets of modeled climate forcings, B140\_Topo1 and B140\_Topo2, on the ice-sheet geometry which differ in the prescribed extent and elevation of the North American ice sheet. The two climate forcings are very different, but the resulting effect on the Eurasian ice sheet is not very strong, leading to a smaller Eurasian ice sheet by 2 m SLE in the case of B140\_Topo2 forcing. This mass loss relative to the experiments with B140\_Topo1 forcing is particularly pronounced over the southern part of the ice sheet due to warmer mean annual and July air temperatures, which are accompanied by lower accumulation.

A large range of sensitivity experiments was conducted with the aim of investigating uncertainties in the ice-sheet reconstruction and providing an ensemble of ice-sheet geometries. In total, 140 experiments were conducted on both ice-sheet grids (Eu20 and NH40), using both climate forcings B140\_Topo1 and B140\_Topo2. However, some of the experiments conducted on the Eurasia 20 km grid show numerical instabilities and were not considered in the analysis. The five categories that we investigated are related to climate corrections (A), to the PDD scheme which is a semi-empirical method to determine ablation (B), to the determination of ice stream areas and parameters related to basal drag (C), to parameters defining the shape of ice shelves (D) and to solid-earth processes (E). The most sensitive categories are B and C, whereas the model is moderately sensitive to parameter changes from category A. The ice-sheet model is relatively insensitive to parameter changes from categories D and E (Figure 6-1).

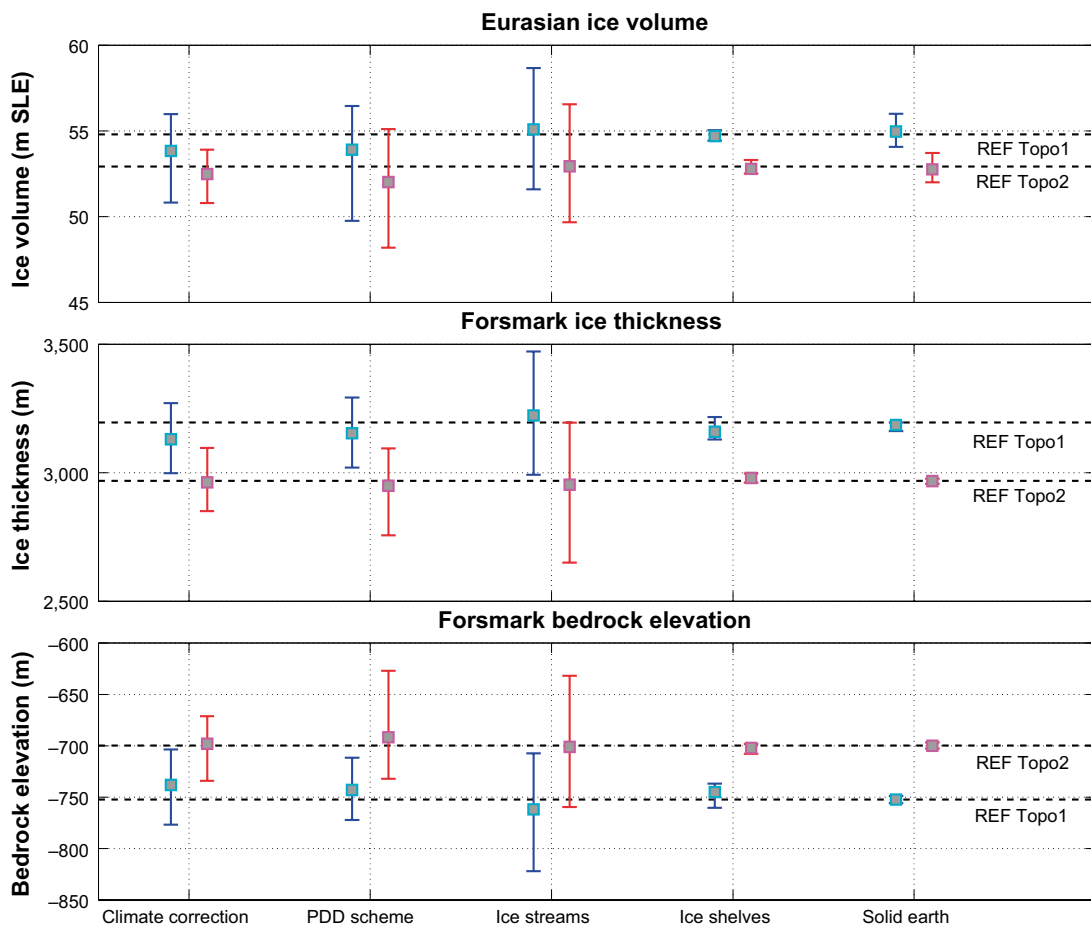


**Figure 6-1.** Ensemble mean Eurasian ice volume (in m SLE, top), ice thickness over Forsmark (middle) and bedrock elevation over Forsmark (bottom) for each of the five groups of sensitivity experiments using B140\_Topo1 (cyan squares) and B140\_Topo2 climate forcing (pink squares). The maximum and minimum of each group for Topo1 and Topo2 experiments is shown by blue and red bars, respectively. Corresponding values for the reference experiments Eu20 REF\_Top01 and Eu20 REF\_Top02 are indicated by black dashed lines.

Some of the experiments are clearly not realistic, and were only performed to investigate the sensitivity of the model, and not to reconstruct a realistic Late Saalian ice-sheet topography. Among these experiments is A1, which explores the effect of very low lapse rates, B8, using a particularly low amount of refreezing and D5 and D6, imposing too high oceanic basal melting rates relative to values found in literature and which are rather more likely to be representative of future climate-change scenarios.

- The univariate ice-sheet experiments reveal only a low sensitivity to moderate changes in lapse rates, as an increase (decrease) in temperature is compensated by an increase (decrease) in accumulation as well. However, extremely high lapse rates (experiment A3) lead to a disappearance of the Eurasian ice sheet. The model is relatively sensitive to changes in the accumulation rate (experiments A4-A11), and particularly imposing the snowfall from CESM instead of total precipitation (experiment A11) strongly reduces ice thickness at the Forsmark site by ~200 m relative to the reference experiment REF\_Topo1.
- Of high importance are PDD parameters: Particularly melting factors  $C_{snow}$  and  $C_{ice}$  and the standard deviation of the daily air temperature cycle  $\sigma$  have a large effect on the geometry of the ice sheet, and should be chosen with care.
- The treatment of fast-flowing areas is one of the advantages of GRISLI, as it allows for a more realistic simulation of ice streams compared with other ice-sheet models which do not include a specific treatment of these areas. The model reacts highly sensitively to the parameters that define the ice-stream area. Also, the impact of the basal drag parameter is very large. The “ice stream” experiments clearly mark the lower and upper bounds of all the univariate experiments that we performed. Given that these parameters are not well constrained by observations, this large range clearly enhances the uncertainty of our experiments.
- Our ice-sheet simulations reveal that the Eurasian ice sheet is not particularly sensitive to calving front thicknesses and basal melt rates below ice shelves in general. Furthermore, the Eurasian ice sheet does not react very sensitively to changes in geothermal heat flux, which can be explained by basal temperatures that are already at the pressure melting point over large parts of the ice sheet when using observed values.
- The characteristic time of the relaxing asthenosphere plays a minor role, since our ice-sheet simulations are branched from the reference simulations that already reached isostatic equilibrium.
- We performed 6 multi variate experiments for each ice-sheet grid in order to investigate the effect of parameter change combinations. In experiments F2 and F3, we investigated to which extent PDD parameters and basal dragging compensate each other. Results show that, similarly to the univariate experiments, the impact of basal drag is the strongest and is not fully compensated by changes in the PDD parameters. The maximum ice thickness over Forsmark obtained with those multivariate experiments reaches 3,405 m, leading to a bedrock depression of about 804 meters. Those values are in the range of what we obtained with the univariate experiments.

The lower bound of all the sensitivity experiments regarding ice thickness over Forsmark constitutes experiment C1, which tests the effect of lower sediment thickness thresholds and leads to a more extended area of fast flow. The overall Eurasian ice volume decreases by 3.2 m SLE, and ice thickness at the Forsmark site reduces by ~200 m compared with REF\_Topo1. The upper bound is represented by experiment C4, which imposes a larger basal drag coefficient resulting in a slow down of basal velocities. This experiment results in an increase in Eurasian ice volume by 4 m SLE, and of an ice thickness at the Forsmark area by ~280 m relative to REF\_Topo1. These results highlight the importance of basal processes on the overall ice-sheet dynamics.

## 7 Outlook from the project

From the analysis performed above, several aspects of the ice dynamics could be improved to better constrain the range of realistic ice thicknesses attributed to the Late Saalian glaciation. Most of the uncertainties in the results arise from three major issues: surface mass balance, basal hydrology and the type of experiments conducted, i.e. steady-state or transient.

### ***Improve and constrain surface mass balance***

The surface mass balance scheme embedded in GRISLI is the Positive Degree Day (PDD) semi-empirical method. This method is based on the calculation of available energy to melt snow and ice using mean annual and July surface air temperatures and mean annual precipitation. Based on the results obtained, we conclude that the ice sheet is quite sensitive to changes in the PDD physical parameters. However, all the experiments that we performed changing the values of those parameters lead to reasonable Eurasian ice-sheet topographies compared with the initial reconstruction and with Svendsen et al. (2004). However, the PDD scheme lacks a description of the impact of radiative forcing and albedo on the snowpack. Therefore, a more sophisticated scheme using surface energy balance that accounts for surface radiative processes as well as a detailed discretization of the snowpack over the ice could be implemented into GRISLI. However, as stressed by Charbit et al. (2013), such schemes lack strong constraints that could help refine better some of the processes occurring in the snowpack. Charbit et al. (2013) also suggest that the calibration of such energy balance models is done for the present-day ice sheets and such calibration may not be appropriate for past periods. After implementation of such an energy balance model into GRISLI, two main phases would be required: (1) it appears reasonable to focus first on the present-day Greenland ice sheet since most of the energy balance models that have been developed so far were tuned on this area. In addition, the Greenland ice sheet is representative of Northern Hemisphere processes, in contrast to Antarctica; and (2) a tuning would then have to be done for the LGM Eurasian ice sheet, as a glacial climate is generally much drier than the present-day climate over the high latitudes. This could have a substantial impact on the parameters values as shown by Charbit et al. (2013) for the PDD method.

### ***Investigate PDD formulations***

Our results demonstrate that for the Late Saalian Eurasian ice sheet, the downscaling parameters, i.e. lapse rate  $\lambda$  and precipitation factor  $\gamma$ , matter less than the PDD parameters, i.e. standard deviation of daily temperature  $\sigma$  and melting coefficients  $C_{\text{snow}}$  and  $C_{\text{ice}}$ . This has recently been highlighted by the work of Charbit et al. (2013) in which the best reconstructions of the LGM are obtained using a  $\sigma$  dependent on elevation changes and  $C_{\text{snow}}$  and  $C_{\text{ice}}$  expressed as a function of summer temperature (Tarasov and Peltier 2002). Those parametrisations could be tested in relation to the Late Saalian glaciation. However, the fact that we are performing steady-state experiments might cancel the benefit of such parametrisations because the integration time would compensate for the sensitivity. Nevertheless, those parametrisations are not demanding in terms of implementation within the PDD scheme of GRISLI and could easily be tested.

### ***Improve and constrain the basal hydrology***

Basal hydrology is the second most sensitive category from all our sensitivity simulations. The scheme that we used in GRISLI is based on Darcy's law and uses two thresholds, one related directly to hydrological parameters of the physical scheme, the second related to the thickness of sediments located at the base of the ice sheet. Unfortunately, no geological evidence for basal hydrology has been preserved from the Late Saalian period. Therefore, it could be relevant to focus on the Weichselian glaciation since much evidence for hydrology and ice-stream area has been retrieved from this glaciation. By tuning GRISLI to reproduce the Weichselian glaciation, parameter settings resulting in a reasonable simulation of the basal hydrology could be obtained. This would include analysis of the coupling between the model parameterisation and the simulated dynamics at the ice base. Depending on the results, the improvement of the description of basal processes in GRISLI could be important to achieve.

### ***Use a different ice-sheet model***

Our project has been entirely based on the results obtained using the GRISLI ice-sheet model. To perform a more comprehensive assessment of ice thickness, a more robust approach would be to consider the outputs from at least another ice-sheet model. Due to differences in models formulations, which in turn results from the choice of the processes implemented and from the lack of process understanding and observations, different ice-sheet models will give different results under the same boundary and forcing conditions. Therefore, in order to have an improved assessment of the maximum ice-sheet thickness for the late Saalian Eurasian ice sheet, comparison with another ice-sheet model would be beneficial. Specifically, it would be appropriate to use the SICOPOLIS ice-sheet model since this model is polythermal, in distinction to GRISLI, which might affect the thermodynamic behavior of the whole ice sheet.

### ***Use different climate models***

It should be noted that this project was conducted using climate forcing coming from a unique climate model. Different ice modeling studies report the discrepancies in ice geometry obtained using different climate forcing. This point is worth considering and the use of a different climate model could lead to a significant difference in the Late Saalian ice sheet geometries. However, it would very demanding in terms of numerical resources to perform an AOGCM simulation at roughly 1° horizontal resolution. Depending on how much CPU could be used for the simulations, it could take up to three months for each climate model to reach an equilibrium in the first layers of the ocean. Ideally, this should be investigated carefully to make a proper assessment, similarly to using a different ice-sheet model. Technically, unless the study focuses on a period that has been simulated by many other modeling groups, this is not doable within the next future.

### ***Perform multi-parameter simulation ensembles***

So far, in each of the sensitivity tests, changes were introduced only for one parameter. In addition, we only performed three multi-parameters sensitivity simulations. It would be possible to test numerous combinations of changes in physical parameters rather than considering only one at once. In a recent contribution, Applegate et al. (2012) generated a 100-member perturbed-physics ensemble of results with the SICOPOLIS ice-sheet model using the Latin hypercube ensemble method used in Stone et al. (2010). Stone et al. (2010) report that the Latin hypercube method provides a quasi-random sampling of the parameter space that is more even than that produced by Monte Carlo methods. The advantage of this methodology is that it is an efficient method to test the response of the ice sheet to many different combinations of parameters by ensuring sufficient coverage of the parameter space without having to test all possible model combinations, which would be extremely computationally expensive, and therefore not doable, especially with a non-parallelized code, as it is the case for GRISLI. The implementation of such an experiment is not immediately possible and requires substantial work, but is a robust statistical way to explore the sensitivity of an ice sheet to the climate and ice-sheet space parameters.

## References

SKB's (Svensk Kärnbränslehantering AB) publications can be found at [www.skb.se/publications](http://www.skb.se/publications).

- Abe-Ouchi A, Segawa T, Saito F, 2007.** Climatic conditions for modelling the Northern Hemisphere ice sheets throughout the ice age cycle. *Climate of the Past* 3, 423–438.
- Alvarez-Solas J, Montoya M, Ritz C, Ramstein G, Charbit S, Dumas C, Nisancioglu K, Dokken T, Ganopolski A, 2011.** Heinrich event 1: an example of dynamical ice-sheet reaction to oceanic changes. *Climate of the Past* 7, 1297–1306.
- Applegate P J, Kirchner N, Stone E J, Keller K, Greve R, 2012.** An assessment of key model parametric uncertainties in projections of Greenland Ice Sheet behavior. *The Cryosphere* 6, 589–606.
- Astakhov V, 2004.** Middle Pleistocene glaciations of the Russian North. *Quaternary Science Reviews* 23, 1229–1271.
- Astakhov V, 2008.** Geographical extremes in the glacial history of northern Eurasia: post-QUEEN considerations. *Polar Research* 27, 280–288.
- Beghin P, Charbit S, Dumas C, Kageyama M, Roche D M, Ritz C, 2014.** Interdependence of the growth of the Northern Hemisphere ice sheets during the last glaciation: the role of atmospheric circulation. *Climate of the Past* 10, 345–358.
- Berger A, 1978.** Long-term variations of daily insolation and Quaternary climatic changes. *Journal of the Atmospheric Sciences* 35, 2362–2367.
- Berger A, Loutre M F, 1991.** Insolation values for the climate of the last 10 millions years. *Quaternary Science Reviews* 10, 297–317.
- Bindschadler R A, Nowicki S, Abe-Ouchi A, Aschwanden A, Choi H, Fastook J, Granzow G, Greve R, Gutowski G, Herzfeld U, Jackson C, Johnson J, Kroulev C, Levermann A, Lipsomb W, Martin M A, Morlighem M, Parizek B R, Pollard D, Price S F, Ren D, Saito F, Sato T, Seddik H, Seroussi H, Takahashi K, Walker R, Wang W L, 2013.** Ice-sheet model sensitivities to environmental forcing and their use in projecting future sea level (the SeaRISE project). *Journal of Glaciology* 59, 126–128.
- Bintanja R, van de Wal R S W, 2008.** North American ice-sheet dynamics and the onset of 100,000-year glacial cycles. *Nature* 454, 869–872.
- Bintanja R, van de Wal R S W, Oerlemans J, 2005.** Modelled atmospheric temperatures and global sea levels over the past million years. *Nature* 437, 126–128.
- Bonelli S, Charbit S, Kageyama M, Woillez M-N, Ramstein G, Dumas C, Quiquet A, 2009.** Investigating the evolution of major Northern Hemisphere ice sheets during the last glacial-interglacial cycle. *Climate of the Past* 5, 329–345.
- Bougamont M, Bamber J L, Ridley J K, Gladstone R M, Greuell W, Hanna E, Payne A J, Rutt I, 2007.** Impact of model physics on estimating the surface mass balance of the Greenland ice sheet. *Geophysical Research Letters* 34, L17501.
- Braithwaite R J, 1995.** Positive degree-day factors for ablation on the Greenland ice sheet studied by energy-balance modelling. *Journal of Glaciology* 41, 153–160.
- Calov R, Hutter K, 1996.** The thermomechanical response of the Greenland ice sheet to various climate scenarios. *Climate Dynamics* 12, 243–260.
- Calov R, Greve R, Abe-Ouchi A, Bueler E, Huybrechts P, Johnson J V, Pattyn F, Pollard D, Ritz C, Saito F, Tarasov L, 2010.** Results from the Ice-Sheet Model Intercomparison Project Heinrich Event IntercOmparison (ISMIP HEINO). *Journal of Glaciology* 56, 197.
- Calvo E, Villanueva J, Gimalt J O, Boelaert A, Labeyrie L, 2001.** New insights into the glacial latitudinal temperature gradients in the North Atlantic. Results from  $U^{K}_{37}$  sea surface temperatures and terrigenous inputs. *Earth and Planetary Science Letters* 188, 509–519.

- Channell J E T, Hodell D A, Romero O, Hillaire-Marcel C, de Vernal A, Stoner J S, Mazaud A, Röhl U, 2012.** A 750- kyr detrital-layer stratigraphy for the North Atlantic (IODP Sites U1302–U1303, Orphan Knoll Labrador Sea). *Earth and Planetary Science Letters* 317, 218–230.
- Chapman M R, Shackleton N J, Duplessy J-C, 2000.** Sea surface temperature variability during the last glacial-interglacial cycle: assessing the magnitude and pattern of climate change in the North Atlantic. *Palaeogeography, Palaeoclimatology, Palaeoecology* 157, 1–25.
- Charbit S, Ritz C, Ramstein G, 2002.** Simulations of Northern Hemisphere ice-sheet retreat: sensitivity to physical mechanisms involved during the Last Deglaciation. *Quaternary Science Reviews* 21, 243–265.
- Charbit S, Dumas C, Kageyama M, Roche D M, Ritz C, 2013.** Influence of ablation-related processes in the build-up of simulated Northern Hemisphere ice sheets during the last glacial cycle. *The Cryosphere* 7, 681–698.
- Chen M-T, Chang Y-P, Chang C-C, Wang L-W, Wang C-H, Yu E-F, 2002.** Late Quaternary sea-surface temperature variations in the southeast Atlantic: a planktic foraminifer faunal record of the past 600 000 yr (IMAGES II MD962085). *Marine Geology* 180, 163–181.
- Chen M-T, Shiau L-J, Yu P-S, Chiu T-C, Chen Y-G, Wei K-Y, 2003.** 500,000-year records of carbonate, organic carbon, foraminiferal sea-surface temperature from the southeastern South China Sea (near Palawan Island). *Palaeogeography, Palaeoclimatology, Palaeoecology* 197, 113–131.
- Clark P U, Licciardi J M, MacAyeal D R, Jenson J W, 1996.** Numerical reconstruction of a soft-bedded Laurentide Ice Sheet during the last glacial maximum. *Geology* 24, 679–682.
- Colleoni F, 2009.** On the Late Saalian glaciation (160–140 ka): a climate modeling study. PhD thesis. Laboratoire de Glaciologie et de Géophysique de l'Environnement, Université Grenoble I.
- Colleoni F, Krinner G, Jakobsson M, 2009a.** Sensitivity of the Late Saalian (140 kyrs BP) and LGM (21 kyrs BP) Eurasian ice sheet surface mass balance to vegetation feedbacks. *Geophysical Research Letters* 36, L08704.
- Colleoni F, Krinner G, Jakobsson M, Peyaud V, Ritz C, 2009b.** Influence of regional factors on the surface mass balance of the large Eurasian ice sheet during the peak Saalian (140 kyrs BP). *Global and Planetary Change* 68, 132–148.
- Colleoni F, Liakka J, Krinner G, Jakobsson M, Masina S, Peyaud V, 2010.** The sensitivity of the Late Saalian (140 ka) and LGM (21 ka) Eurasian ice sheets to sea surface conditions. *Climate Dynamics* 37, 531–553.
- Crowley T J, 1995.** Ice age terrestrial carbon changes revisited. *Global Biogeochemical Cycles* 9, 377–389.
- Crucifix M, Loutre M-F, Lambeck K, Berger A, 2001.** Effect of isostatic rebound on modelled ice volume variations during the last 200 kyrs. *Earth and Planetary Science Letters* 184, 623–633.
- de Abreu L, Shackleton N J, Schönfeld J, Hall M, Chapman M, 2003.** Millennial-scale oceanic climate variability off the Western Iberian margin during the last two glacial periods. *Marine Geology* 196, 1–20.
- Dehnert A, Preusser F, Kramers J D, Akçar N, Kubik P W, Reber R, Schlüchter C, 2010.** A multi-dating approach applied to proglacial sediments attributed to the Most Extensive Glaciation of the Swiss Alps. *Boreas* 39, 620–632.
- de Noblet N I, Prentice I C, Jousseume S, Texier D, Botta A, Haxeltine A, 1996.** Possible role of atmosphere-biosphere interactions in triggering the last deglaciation. *Geophysical Research Letters* 23, 3191–3194.
- Durand G, Olivier Gagliardini O, Zwinger T, Le Meur E, Hindmarch R C A, 2009.** Full Stokes modeling of marine ice sheets: influence of the grid size. *Annals of Glaciology* 50, 109–114.
- Dyke A S, Andrews J T, Clark P U, England J H, Miller G H, Shaw J, Veillette J J, 2002.** The Laurentide and Innuitian ice sheets during the Last Glacial Maximum. *Quaternary Science Reviews* 21, 9–31.

- Ehlers J, Gibbard P L, 2007.** The extent and chronology of Cenozoic global glaciation. *Quaternary International* 164, 6–20.
- Fausto R S, Ahlström A P, Van As D, Bøggild C E, Johnsen S J, 2009.** A new present-day temperature parameterization for Greenland. *Journal of Glaciology* 55, 95–105.
- Fleming K, Lambeck K, 2004.** Constraints on the Greenland Ice Sheet since the Last Glacial Maximum from sea-level observations and glacial-rebound models. *Quaternary Science Reviews* 23, 1053–1077.
- Fritz S C, Baker P A, Lowenstein T K, Seltzer G O, Rigsby C A, Dwyer G S, Tapia P M, Arnold K A, Ku T-L, Luo S, 2004.** Hydrologic variation during the last 170,000 years in the southern hemisphere tropics of South America. *Quaternary Research* 61, 95–104.
- Gent P R, Danabasoglu G, Donner L J, Holland M M, Hunke E C, Jayne S R, Lawrence D M, Neale R B, Rasch P J, Vertenstein M, Worley P H, Yang Z-L, Zhang M, 2011.** The Community Climate System Model Version 4. *Journal of Climate* 24, 4973–4991.
- Goldstein R M, Engelhardt H, Kamb B, Frolich R M, 1993.** Satellite radar interferometry for monitoring ice sheet motion: application to an Antarctic ice stream. *Science* 262, 1525–1530.
- Goni M A, Hartz D M, Thunell R C, Tappa E, 2001.** Oceanographic considerations for the application of the alkenone-based paleotemperature  $U_{37}^{K'}$  index in the Gulf of California. *Geochimica et Cosmochimica Acta* 65, 545–557.
- Greve R, 2005.** Relation of measured basal temperatures and the spatial distribution of the geothermal heat flux for the Greenland ice sheet. *Annals of Glaciology* 42, 424–432.
- Greve R, Blatter H, 2009.** Dynamics of ice sheets and glaciers. Berlin: Springer.
- Haug G H, Ganopolski A, Sigman D M, Rosell-Mele A, Swann G E A, Tiedemann R, Jaccard S L, Bollmann J, Maslin M A, Leng M J, Eglinton G, 2005.** North Pacific seasonality and the glaciation of North America 2.7 million years ago. *Nature* 433, 821–825.
- Hellmer H H, Kauker F, Timmermann R, Determann J, Rae J, 2012.** Twenty-first-century warming of a large Antarctic ice-shelf cavity by a redirected coastal current. *Nature* 485, 225–228.
- Helmke J P, Bauch H A, Erlenkeuser H, 2003.** Development of glacial and interglacial conditions in the Nordic seas between 1.5 and 0.35 Ma. *Quaternary Science Reviews* 22, 1717–1728.
- Hippler D, Eisenhauer A, Nagler T F, 2006.** Tropical Atlantic SST history inferred from Ca isotope thermometry over the last 140 ka. *Geochimica et Cosmochimica Acta* 70, 90–100.
- Hughes T, Denton G H, Grosswald M G, 1977.** Was there a late-Würm Arctic ice sheet. *Nature* 266, 5603.
- Hutter K, 1983.** Theoretical glaciology: material science of ice and the mechanics of glaciers and ice sheets. Dordrecht: Reidel.
- Huybrechts P, de Wolde J, 1999.** The dynamic response of the Greenland and Antarctic ice sheets to multiple-century climatic warming. *Journal of Climate* 12, 2169–2188.
- Ivins E R, James T S, 2005.** Antarctic glacial isostatic adjustment: a new assessment. *Antarctic Science* 17, 541–553.
- Jakobsson M, Nilsson J, O'Regan M, Backman J, Löwemark L, Dowdeswell J A, Mayer L, Polyak L, Colleoni F, Anderson L G, Björk G, Darby D, Eriksson B, Hanslik D, Hell B, Marcussen C, Sellén E, Wallin Å, 2010.** An Arctic Ocean ice shelf during MIS 6 constrained by new geophysical and geological data. *Quaternary Science Reviews* 29, 3505–3517.
- Jansen J H F, Kuijpers A, Troelstra S R A, 1986.** A mid-Brunhes climatic event: long-term changes in global atmosphere and ocean circulation. *Science* 232, 619–622.
- Joughin I, Fahnestock M, MacAyeal D, Bamber J L, Gogineni P, 2001.** Observation and analysis of ice flow in the largest Greenland ice stream. *Journal of Geophysical Research* 106, 34021–34034.

- Jouzel J, Masson-Delmotte V, Cattani O, Dreyfus G, Falourd S, Hoffmann G, Minster B, Nouet J, Barnola J M, Chappellaz J, Fischer H, Gallet J C, Johnsen S, Leuenberger M, Loulergue L, Luethi D, Oerter H, Parrenin F, Raisbeck G, Raynaud D, Schilt A, Schwander J, Selmo E, Souchez R, Spahni R, Stauffer B, Steffensen J P, Stenni B, Stocker T F, Tison J L, Werner M, Wolff E W, 2007.** Orbital and millennial Antarctic climate variability over the past 800,000 years. *Science* 317, 793–797.
- Kageyama M, Valdes P J, 2000.** Impact of the North American ice-sheet orography on the Last Glacial Maximum eddies and snowfall. *Geophysical Research Letters* 27, 1515–1518.
- Kageyama M, Valdes P J, Ramstein G, Hewitt C, Wyputta U, 1999.** Northern Hemisphere storm tracks in present day and last glacial maximum climate simulations: a comparison of the European PMIP models. *Journal of Climate* 12, 742–760.
- Kageyama M, Braconnot P, Bopp L, Mariotti V, Roy T, Woillez M-N, Caubel A, Foujols M-A, Guilyardi E, Khodri M, Lloyd J, Lombard F, Marti O, 2013.** Mid-Holocene and last glacial maximum climate simulations with the IPSL model: part II: model-data comparisons. *Climate Dynamics* 40, 2469–2495.
- Kandiano E S, Bauch H A, Müller A, 2004.** Sea surface temperature variability in the North Atlantic during the last two glacial–interglacial cycles: comparison of faunal, oxygen isotopic, Mg/Ca-derived records. *Palaeogeography, Palaeoclimatology, Palaeoecology* 204, 145–164.
- Kirchner N, Hutter K, Jakobsson M, Gyllencreutz R, 2011.** Capabilities and limitations of numerical ice sheet models: a discussion for Earth-scientists and modelers. *Quaternary Science Reviews* 30, 3691–3704.
- Kirst G J, Schneider R R, Müller P J, von Storch I, Wefer G, 1999.** Late quaternary temperature variability in the Benguela Current system derived from alkenones. *Quaternary Research* 52, 92–103.
- Kleman J, Hättestrand C, 1999.** Frozen-bed Fennoscandian and Laurentide ice sheets during the Last Glacial Maximum. *Nature* 402, 63–66.
- Kleman J, Fastook J, Ebert K, Nilsson J, Caballero R, 2013.** Pre-LGM Northern Hemisphere paleo-ice sheet topography. *Climate of the Past*, 9, 2557–2587.
- Krinner G, Genthon C, 1999.** Altitude dependence of the ice sheet surface climate. *Geophysical Research Letters* 26, 2227–2230.
- Krinner G, Mangerud J, Jakobsson M, Crucifix M, Ritz C, Svendsen J, 2004.** Enhanced ice sheet growth in Eurasia owing to adjacent ice-dammed lakes. *Nature* 427, 429–432.
- Krinner G, Boucher O, Balanski Y, 2006.** Ice-free glacial northern Asia due to dust deposition on snow. *Climate Dynamics* 27, 773–777.
- Lambeck K, Purcell A, Funder S, Kjær K H, Larsen E, Möller P, 2006.** Constraints on the Late Saalian to early Middle Weichselian ice sheet of Eurasia from field data and rebound modelling. *Boreas* 35, 539–575.
- Laske G, Masters G, 1997.** A global digital map of sediment thickness. *Eos Transactions American Geophysical Union* 78, F483.
- Lea D W, Pak D K, Spero H J, 2000.** Climate impact of late quaternary equatorial Pacific sea surface temperature variations. *Science* 289, 1719–1724.
- Le Meur E, Huybrechts P, 1996.** A comparison of different ways of dealing with isostasy: examples from modeling the Antarctic ice sheet during the last glacial cycle. *Annals of Glaciology* 23, 309–317.
- Lisiecki L E, Raymo M E, 2005.** A Pliocene–Pleistocene stack of 57 globally distributed benthic  $\delta^{18}\text{O}$  records. *Paleoceanography* 20, PA1003.
- Lisiecki L E, Raymo M E, 2007.** Plio–Pleistocene climate evolution: trends and transitions in glacial cycle dynamics. *Quaternary Science Reviews* 26, 56–69.

- Loulergue L, Schilt A, Spahni R, Masson-Delmotte V, Blunier T, Lemieux B, Barnola J-M, Raynaud D, Stocker T F, Chappellaz J, 2008.** Orbital and millennial-scale features of atmospheric CH<sub>4</sub> over the past 800,000 years. *Nature* 453, 383–386.
- Lüthi D, Le Floch M, Bereiter B, Blunier T, Barnola J-M, Siegenthaler U, Raynaud D, Jouzel J, Fischer H, Kawamura K, Stocker T F, 2008.** High-resolution carbon dioxide concentration record 650,000–800,000 years before present. *Nature* 453, 379–382.
- MacAyeal D R, 1989.** Large-scale ice flow over a viscous basal sediment: theory and application to ice stream B, Antarctica. *Journal of Geophysical Research* 94, 4071–4087.
- Magand O, Frezzotti M, Pourchet M, Stenni B, Genoni L, Fily M, 2004.** Climate variability along latitudinal and longitudinal transects in East Antarctica. *Annals of Glaciology* 39, 351–358.
- Mahowald N, Kohfeld K, Hansson M, Balanski Y, Harrison S P, Prentice I C, Schulz M, Rodhe H, 1999.** Dusts sources and deposition during the last glacial maximum and current climate: a comparison of model results with paleodata from ice cores and marine sediments. *Journal of Geophysical Research* 104, 15895–15916.
- Marshall S J, James T S, Clarke G K C, 2002.** North American ice sheet reconstructions at the last glacial maximum. *Quaternary Science Reviews* 21, 175–192.
- Marshall S, Sharp M, Burgess D, Anslow F, 2007.** Near-surface-temperature lapse rates on the Prince of Wales Icefield, Ellesmere Island, Canada: implications for regional downscaling of temperature. *International Journal of Climatology* 27, 385–398.
- Martinson D G, Pisias N G, Hays J D, Imbrie J, Moore T C, Shackleton N J, 1987.** Age dating and the orbital theory of the ice ages: development of a high-resolution 0 to 300,000-year chronostratigraphy. *Quaternary Research* 27, 1–29.
- Mashiotta T A, Lea D W, Spero H J, 1999.** Glacial interglacial changes in Subantarctic sea surface temperature and δ<sup>18</sup>O-water using foraminiferal Mg. *Earth and Planetary Science Letters* 170, 417–432.
- Masson-Delmotte V, Stenni B, Pol K, Braconnot P, Cattani O, Falourd S, Kageyama M, Jouzel J, Landais A, Minster B, Barnola J M, Chappellaz J, Krinner G, Johnsen S, Röthlisberger R, Hansen J, Mikolajewicz U, Otto-Bliesner B, 2010.** EPICA Dome C record of glacial and interglacial intensities. *Quaternary Science Reviews* 29, 113–128.
- Niessen F, Hong J K, Hegewald A, Matthiessen J, Stein R, Kim H, Kim S, Jensen L, Jokat W, Nam S-I, Kang S-H, 2013.** Repeated Pleistocene glaciation of the East Siberian continental margin. *Nature Geoscience* 6, 842–846.
- Nürnberg D, Groeneveld J, 2006.** Pleistocene variability of the Subtropical Convergence at East Tasman Plateau: Evidence from planktonic foraminiferal Mg/Ca (ODP Site 1172A). *Geochemistry, Geophysics, Geosystems* 7. doi:10.1029/2005GC000984.
- Näslund J-O, Jansson P, Fastook J L, Johnson, J, Andersson L, 2005.** Detailed spatially distributed geothermal heat-flow data for modeling of basal temperatures and meltwater production beneath the Fennoscandian ice sheet. *Annals of Glaciology* 40, 95–101.
- Otto-Bliesner B L, Brady E C, Clauzet G, Tomas R, Levis S, Kothavala Z, 2006.** Last glacial maximum and Holocene climate in CCSM3. *Journal of Climate* 19, 2526–2544.
- Pahnke K, Sachs J P, 2006.** Sea surface temperatures of southern midlatitudes 0–160 kyr B.P. *Paleoceanography* 21, PA2003. doi:10.1029/2005PA001191.
- Pausata F S R, Li C, Wettstein J J, Kageyama M, Nisancioglu K H, 2011.** The key role of topography in altering North Atlantic atmospheric circulation during the last glacial period. *Climate of the Past* 7, 1089–1101.
- Pelejero C, Calvo E, Barrows T T, Logan G A, De Deckker P, 2006.** South Tasman Sea alkenone palaeothermometry over the last four glacial/interglacial cycles. *Marine Geology* 230, 73–86.
- Peltier W R, 1994.** Ice age paleotopography. *Science* 265, 195–201.
- Peltier W R, 2004.** Global glacial isostasy and the surface of the ice-age Earth: the ICE-5G (VM2) Model and GRACE. *Annual Reviews Earth and Planetary Sciences* 32, 111–149.

- Peltier W R, Andrews J T, 1976.** Glacial-Isostatic Adjustment—I. The Forward Problem. *Geophysical Journal of the Royal Astronomical Society* 46, 605–646.
- Petit J R, Jouzel J, Raynaud D, Barkov N I, Barnola J-M, Basile I, Bender M, Chapellaz J, Davis J, Delaygue G, Delmotte M, Kotlyakov V M, Legrand M, Lipenkov V Y, Lorius C, Pépin L, Ritz C, Saltzman E, Stievenard M, 2001.** Vostok ice core data for 420,000 years. IGBP PAGES/World Data Center for Paleoclimatology Data Contribution Series #2001-076. NOAA/NGDC Paleoclimatology Program, Boulder CO, USA.
- Peyaud V, 2006.** Role of the ice sheet dynamics in major climate changes. PhD thesis. Laboratoire de Glaciologie et de Géophysique de l'Environnement, Université Grenoble I.
- Peyaud V, Ritz C, Krinner G, 2007.** Modelling the Early Weichselian Eurasian Ice Sheets: role of ice shelves and influence of ice-dammed lakes. *Climate of the Past* 3, 375–386.
- Pfeffer W T, Meier M F, Illangasekare T H, 1991.** Retention of Greenland runoff by refreezing: implications for projected future sea level change. *Journal of Geophysical Research* 96, 22117–22124.
- Polyak L, Best K M, Crawford K A, Council E A, St-Onge G, 2013.** Quaternary history of sea ice in the western Arctic Ocean based on foraminifera. *Quaternary Science Reviews* 79, 145–156.
- Quiquet A, Punge H J, Ritz C, Fettweis X, Gallee H, Kageyama M, Krinner G, Salas y Méliá D, Sjolte J, 2012.** Sensitivity of a Greenland ice sheet model to atmospheric forcing fields. *The Cryosphere* 6, 999–1018.
- Rabineau M, Berne S, Olivet J-L, Aslanian D, Guillocheau F, Joseph P, 2006.** Paleo sea levels reconsidered from direct observation of paleoshoreline position during glacial maxima (for the last 500,000 yr). *Earth and Planetary Science Letters* 252, 119–137.
- Reeh N, 1991.** Parameterization of melt rate and surface temperature on the Greenland ice Sheet. *Polarforschung* 59, 113–128.
- Ritz C, Rommelaere V, Dumas C, 2001.** Modeling the evolution of Antarctic ice sheet over the last 420,000 years: Implications for altitude changes in the Vostok region. *Journal of Geophysical Research* 106, 31943–31964.
- Robinson A, Calov R, Ganopolski A, 2012.** Multistability and critical thresholds of the Greenland ice sheet. *Nature Climate Change* 2, 429–432.
- Rogozhina I, Martinec Z, Hagedoorn J M, Thomas M, Fleming K, 2011.** On the long-term memory of the Greenland Ice Sheet. *Journal of Geophysical Research* 116. doi: 10.1029/2010JF001787.
- Ruddiman W F, 2003.** Orbital insolation, ice volume, greenhouse gases. *Quaternary Science Reviews* 22, 1597–1629.
- Rutt I C, Hagdorn M, Hulton N R J, Payne A J, 2009.** The Glimmer community ice sheet model. *Journal of Geophysical Research* 114, F02004.
- Schaefer G, Rodger J S, Hayward B W, Kennett J P, Sabaa A T, Scott G H, 2005.** Planktic foraminiferal and sea surface temperature record during the last 1 Myr across the Subtropical Front Southwest Pacific. *Marine Micropaleontology* 54, 191–212.
- Schneider R, 1999.** Atlantic Alkenone sea-surface temperature records. In Abrantes, F, Mix, A (eds). *Reconstructing ocean history: a window into the future*. New York: Kluwer Academic/Plenum.
- Schneider R R, Müller P J, Ruhland G, 1995.** Late Quaternary surface circulation in the east equatorial South Atlantic: evidence from alkenone sea surface temperatures. *Paleoceanography* 10, 197–219.
- Schneider R R, Müller P J, Ruhland G, Meinecke G, Schmidt H, Wefer G, 1996.** Late Quaternary Surface temperatures and productivity in the east equatorial South Atlantic: response to changes in trade/monsoon wind forcing and surface water advection. In Wefer G, Berger W H, Siedler G, Webb D J (eds). *The South-Atlantic: present and past circulation*. Berlin: Springer.
- Shapiro N M, Ritzwoller M H, 2004.** Inferring surface heat flux distributions guided by a global seismic model: particular application to Antarctica. *Earth and Planetary Science Letters* 223, 213–224.

- Siddall M, Bard E, Rohling E J, Hemleben C, 2006.** Sea-level reversal during Termination II. *Geology* 34, 817–820.
- Spahni R, Chappellaz J, Stocker T F, Loulergue L, Hausammann G, Kawamura K, Flückiger J, Schwander J, Raynaud D, Masson-Delmotte V, Jouzel J, 2005.** Atmospheric methane and nitrous oxide of the late Pleistocene from Antarctic ice cores. *Science* 310, 1317–1321.
- Stone E J, Lunt D J, Rutt I C, Hanna E, 2010.** Investigating the sensitivity of numerical model simulations of the modern state of the Greenland ice-sheet and its future response to climate change. *Cryosphere*, 4, 397–417.
- Svendsen J I, Alexanderson H, Astakhov V I, Demidov I, Dowdeswell J A, Funder S, Gataulling V, Henriksen M, Hjort J, Houmark-Nielsen M, Hubberten H W, Ingólfsson Ó, Jakobsson M, Kjær K H, Larsen E, Lokrantz H, Lunkka J P, Lyså A, Mangerud J, Matiouchkov A, Murray A, Müller P J, Niessen F, Nikolskaya O, Polyak L, Saarnisto M, Siegert C, Siegert M J, Spielhagen R F, Ruedige S, 2004.** Late Quaternary ice sheet history of Northern Eurasia. *Quaternary Science Reviews* 23, 1229–1271.
- Tarasov L, Peltier W R, 1999.** Impact of thermomechanical ice sheet coupling on a model of the 100 kyr ice age cycle. *Journal of Geophysical Research* 104, 9517–9545.
- Tarasov L, Peltier W R, 2002.** Greenland glacial history and local geodynamic consequences. *Geophysical Journal International* 150, 198–229.
- Tisserand A, Malaizé B, Jullien E, Zaragosi S, Charlier K, Grousset F, 2009.** African monsoon enhancement during the penultimate glacial period (MIS 6.5 ~ 170 ka) and its atmospheric impact. *Paleoceanography* 24. doi: 10.1029/2008PA001630.
- Toucanne S, Zaragosi S, Bourillet J-F, Marieu V, Cremer M, Kageyama M, Van Vliet-Lanoë B, Eynaud F, Turon J-L, Gibbard P L, 2010.** The first estimation of Fleuve Manche palaeoriver discharge during the last deglaciation: evidence for Fennoscandian ice sheet meltwater flow in the English Channel ca 20–18 ka ago. *Earth and Planetary Science Letters* 290, 459–473.
- Turcotte D L, Schubert G, 2002.** *Geodynamics*. Cambridge: Cambridge University Press.
- Tushingham A M, Peltier W R, 1991.** ICE-3G: a new global model of late Pleistocene deglaciation based upon geophysical predictions of post-glacial relative sea level change. *Journal of Geophysical Research* 96, 4497–4523.
- Tzedakis P C, Raynaud D, McManus J F, Berger A, Brovkin V, Kiefer T, 2009.** Interglacial diversity. *Nature Geoscience* 2, 751–755.
- van den Berg J, van de Wal R S W, Milne G A, Oerlemans J, 2008.** Effect of isostasy on dynamical ice sheet modeling: A case study for Eurasia. *Journal of Geophysical Research* 113, B05412.
- Villanueva J, Flores J A, Grimalt J O A, 2002.** A detailed comparison of the  $U^{K}_{37}$  and coccolith records over the past 290 kyrs: implications to the alkenone paleotemperature method. *Organic Geochemistry* 33, 897–905.
- Vizcaíno M, Mikolajewicz U, Junglaus J, Schurgers G, 2010.** Climate modification by future ice sheet changes and consequences for ice sheet mass balance. *Climate Dynamics* 34, 301–324.
- Waelbroeck C, Labeyrie L, Michel E, Duplessy J C, McManus J F, Lambeck K, Balbon E, Labracherie M, 2002.** Sea-level and deep water temperature changes derived from benthic foraminifera isotopic records. *Quaternary Science Reviews* 21, 295–305.
- Weertman J, 1957.** On the sliding of glaciers. *Journal of Glaciology* 3, 33–38.
- Wei G, Deng W, Liu Y, Li X, 2007.** High-resolution sea surface temperature records derived from foraminiferal Mg/Ca ratios during the last 260 ka in the northern South China Sea. *Palaeogeography, Palaeoclimatology, Palaeoecology* 250, 126–138.

## Compilation of SST proxies

**Table A1-1. SST reconstructions from marine records for both LGM (21 kyrs BP) and Late Saalian glacial maximum (140 kyrs BP): [1] Calvo et al. (2001), [2] Schneider et al. (1995), [3] Schneider et al. (1996), [4] Schneider (1999), [5] Pelejero et al. (2006), [6] Kirst et al. (1999), [7] Villanueva et al. (2002), [8] Pahnke and Sachs (2006), [9] Mashiotta et al. (1999), [10] Lea et al. (2000), [11] Nürnberg and Groeneveld (2006), [12] Wei et al. (2007), [13] Hippler et al. (2006), [14] de Abreu et al. (2003), [15] Kandiano et al. (2004), [16] Chapman et al. (2000), [17] Chen et al. (2003) [18] Schaefer et al. (2005), [19] Chen et al. (2002). Data are classified according to annual values (Annual), summer values (Summer) and winter values (Winter). SST reconstructions were obtained using different methods: alkenone (Alk.), Mg/Ca ratio, planktonic foraminifera, modern analogues (mod. ana.).**

Ocean	SST (°C, 21 kyrs BP)	SST (°C, 140 kyrs BP)	Season	Method	References
Atlantic	12.5	13.8	Annual	Alk.	[1]
Atlantic	21.5	21.5	"	Alk.	[2]
Atlantic	18.0	18.0	"	Alk.	[4]
Atlantic	9.8	11.5	"	Alk.	[5]
Atlantic	10.2	9.2	"	Alk.	[5]
Atlantic	16.5	17.0	"	Alk.	[2]
Atlantic	23.0	24.0	"	Alk.	[3]
Atlantic	14.5	14.25	"	Alk.	[6]
Atlantic	8.8	14.0	"	Alk.	[7]
Atlantic	13.0	16.0	"	Alk.	[8]
Pacific	22.5	22.5	"	Mg/Ca	[10]
Pacific	26.0	26.0	"	Mg/Ca	[10]
Pacific	19.0	19.0	"	Mg/Ca	[11]
Pacific	22.0	21.25	"	Mg/Ca	[12]
Pacific	21.0	22.0	"	44 Ca/40 Ca	[13]
Pacific	9.8	9.0	"	Alk.	[8]
Southern Ocean	6.6	7.0	"	Mg/Ca	[9]
Atlantic	5.0	8.0	Summer	foram	[14]
Atlantic	3.5	3.0	"	Mg/Ca	[15]
Atlantic	11.75	12.5	"	mod. ana.	[16]
Pacific	27.4	28	"	plank. trans.	[17]
Pacific	12.5	11	"	mod. ana.	[18]
Pacific	4.0	3.5	"	mod. ana.	[18]
Pacific	23.0	23.0	Winter	plank. trans.	[17]
Pacific	9.0	8.0	"	mod. ana.	[18]
Atlantic	11.0	13.0	"	plank. trans.	[19]
Atlantic	0.0	0.0	"	Mg/Ca	[15]

## Notation

Table A2-1. Notation used in this report.

Symbol	Description	Unit
<b>Geometric and physical variables</b>		
$S(x,y,t)$	Surface elevation	m
$S_0(x,y)$	Initial surface elevation	m
SL	Sea level	m
$B(x,y,t)$	Bedrock elevation	m
$B_0(x,y)$	Initial bedrock elevation	m
$H(x,y,t)$	Ice thickness: $S-B$	m
$H_0(x,y)$	Initial ice thickness	m
$p(x,y,z,t)$	Hydrostatic pressure	Pa
$T(x,y,z,t)$	Ice temperature	°C
$T_b(x,y,z,t)$	Basal ice temperature	°C
$T_{pmp}(x,y,z,t)$	Ice temperature relative to the pressure melting point	°C
$u(x,y,z,t)$	Ice velocity	m/yr
$u_B(x,y,z,t)$	Sliding velocity at the base of the ice	m/yr
<b>Mass balance and climate</b>		
$Abl(x,y,t)$		m/yr
$Acc(x,y,t)$		m/yr
$C_{ice}$	Melting factor of ice	mm/d/°C
$C_{snow}$	Melting factor of snow	mm/d/°C
$P(x,y,t)$	Precipitation	m/yr
PDD	Number of positive degree days	
$SMB(x,y,t)$	Surface mass balance	m/yr
$T_{Ann}(x,y,t)$	Mean annual surface air temperature	°C
$T_{Jul}(x,y,t)$	Mean July surface air temperature	°C
$T_d(x,y,t)$	Daily surface air temperature	°C
F	Melting rate at the base of the ice sheet	m/yr
$b_{melt}$	Melting rate at the base of the ice shelf	m/yr
csi	Percentage of ice that refreezes	%
$\lambda_{Ann}$	Lapse rate for annual mean air temperature	°C/km
$\lambda_{July}$	Lapse rate for July air temperature	°C/km
$\gamma$	Precipitation correction factor	°C <sup>-1</sup>
$\sigma$	Standard deviation of the daily air temperature	°C

**Table A2-2. Notation used in this report.**

Symbol	Description	Unit
<b>Thermal properties</b>		
$Q_i$	Deformational heat	$W m^{-2}$
$c$	Heat capacity of ice	$J mol^{-1} kg^{-1}$
$k$	Thermal conductivity of ice	$W ^\circ C^{-1} m^{-1}$
<b>Ice deformation</b>		
$B_{AT}$	Coefficient of the Glen flow law	Pa
$E_f$	Enhancement factor of the flow law	$J mol^{-1}$
$\tau$	Stress tensor	Pa
$\tau'$	Deviatoric stress tensor	Pa
$\dot{\epsilon}'$	Strain rate	$s^{-1}$
$n$	Exponent in the Glen flow law	–
$\bar{\eta}$	Vertically integrated viscosity of the ice	Pa/yr
<b>Sliding and basal drag</b>		
$c_f$	Basal drag coefficient	–
$N$	Effective pressure at the base of the ice	Pa
$T_b$	Basal drag	Pa
<b>Basal hydrology</b>		
$K$	Hydraulic conductivity	m/s
$V_e$	Sub-glacial flow velocity	m/yr
$P_w$	Sub-glacial water pressure	Pa
$h_{sed}^*$	Critical sediment thickness	m
$h_w^*$	Critical hydraulic head	m
$N^*$	Critical effective pressure	Pa
<b>Physical constants</b>		
$\rho$	Density of ice	$910 kg m^{-3}$
$\rho_w$	Density of seawater	$1,028 kg m^{-3}$
$\rho_{fw}$	Density of freshwater	$1,000 kg m^{-3}$
$g$	Gravitational acceleration	$9.81 ms^{-2}$
$R$	Ideal gas constant	$8.3145 J mol^{-1} ^\circ C^{-1}$
<b>Solid earth</b>		
$T_r$	Characteristic relaxation time	yrs

Sensitivity experiments using B140\_Topo2 climate forcing

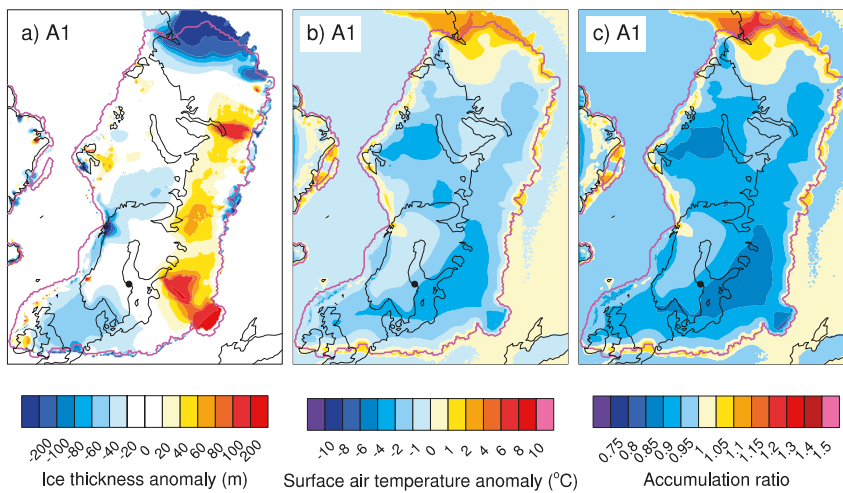


**Figure A3-1.** Impact of lapse rates: Difference in ice thickness (a), mean annual surface air temperature (b) and ratio of accumulation of experiment A1 relative to the reference experiment REF\_Topo2 at the end of the simulation (experiment A1 divided by reference experiment). The magenta line corresponds to the Late Saalian reconstruction from Peyaud (2006).

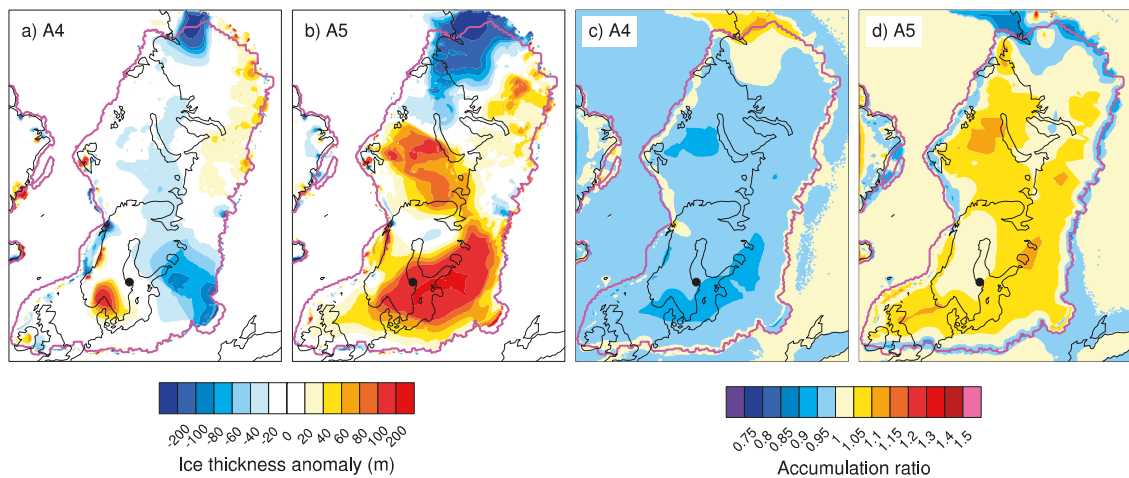


**Figure A3-2.** Impact of precipitation factor  $\gamma$ : Difference in ice thickness (left) and accumulation (right) between the reference experiment REF\_Topo2 and experiments A4 (a, c) and A5 (b, d) at the end of the simulation (sensitivity experiments minus reference experiment). The magenta line corresponds to the Late Saalian reconstruction from Peyaud (2006).

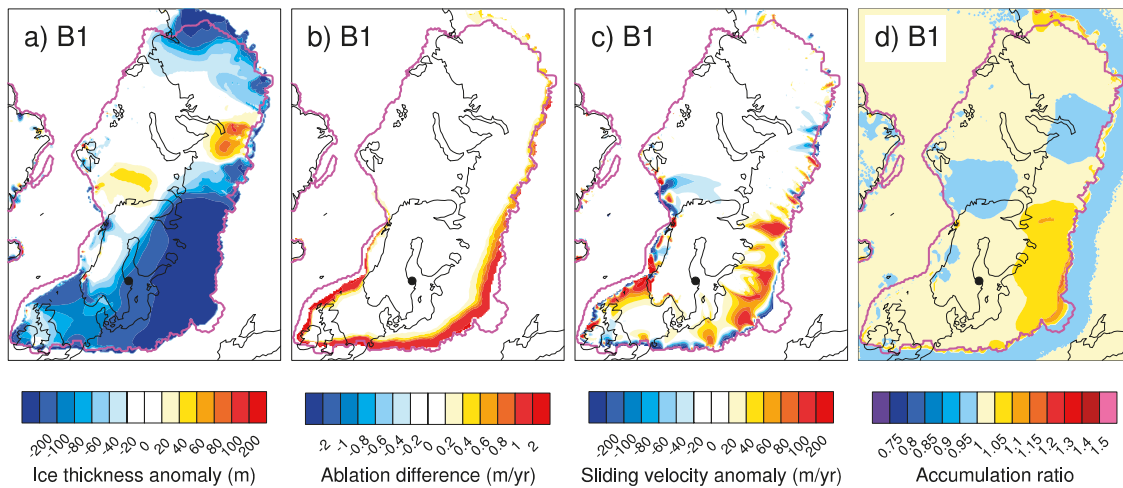


**Figure A3-3.** Impact of  $C_{snow}$  and  $C_{ice}$ : Difference in ice thickness (a), ablation (b), sliding velocity (c) and ratio of accumulation of experiment B1 relative to the reference experiment REF\_Topo2 at the end of the simulation (experiment B1 minus (divided by) reference experiment). The magenta line corresponds to the Late Saalian reconstruction from Peyaud (2006).

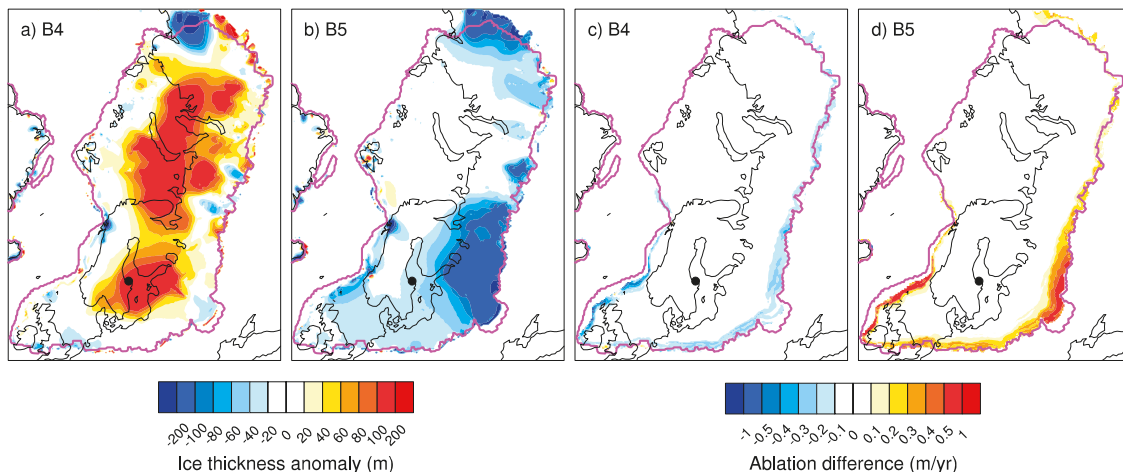


**Figure A3-4.** Impact of daily temperature standard deviation  $\sigma$ : Difference in ice thickness (left) and ablation (right) between the reference experiment REF\_Topo2 and experiments B4 (a, c) and B5 (b, d) at the end of the simulation (sensitivity experiments minus reference experiment). The magenta line corresponds to the Late Saalian reconstruction from Peyaud (2006).

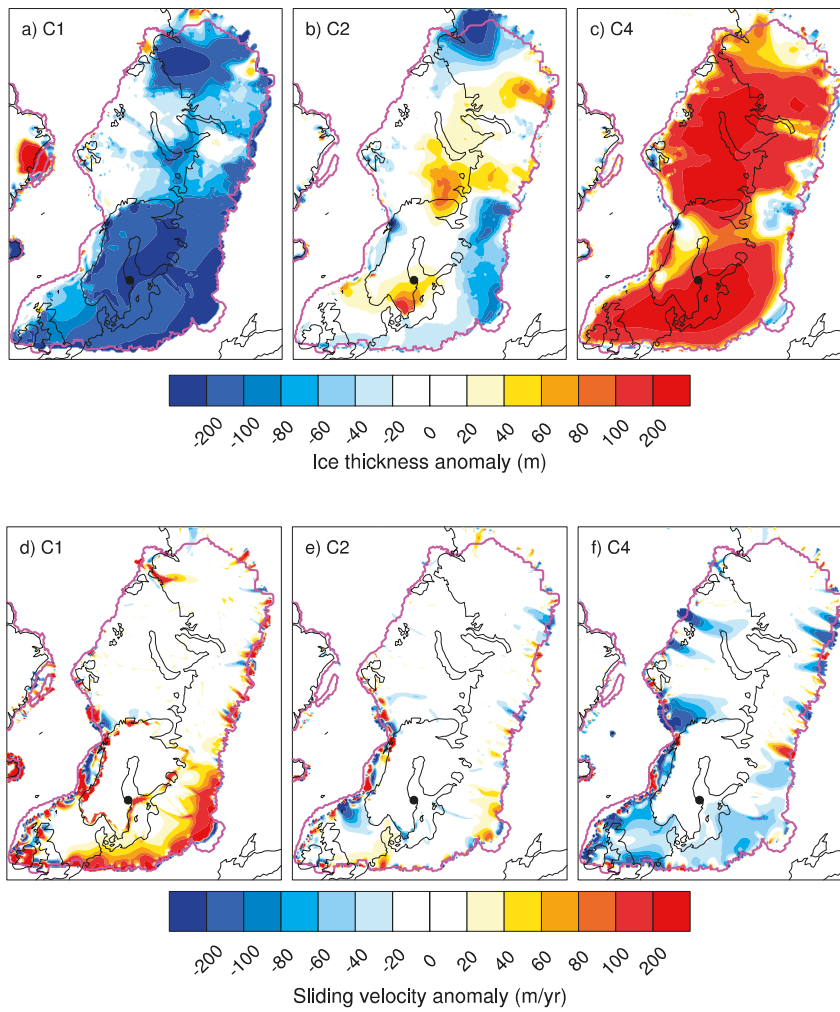


**Figure A3-5.** Impact of sediment thickness: Difference in ice thickness (left) and sliding velocity (right) between the reference experiment REF\_Topo2 and experiments C1 (a, c) and C4 (b, d) at the end of the simulation (sensitivity experiments minus reference experiment). The magenta line corresponds to the Late Saalian reconstruction from Peyaud (2006).

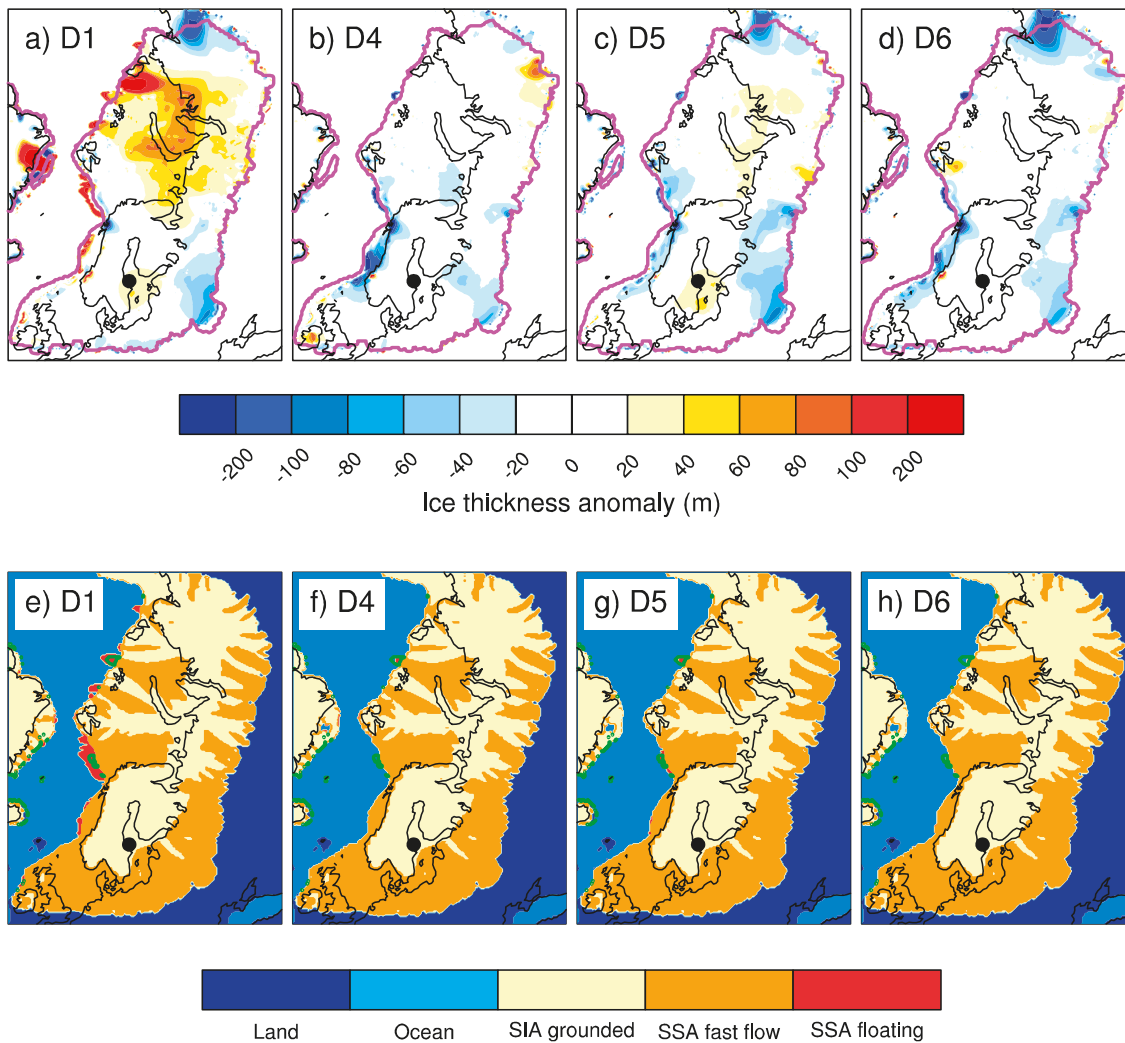


**Figure A3-6.** Impact of calving and ocean heat fluxes. Upper panel: Difference in ice thickness between experiments D1 (a), D4 (b), D5 (c) and D6 (d) and the reference experiment REF\_Topo2 at the end of the simulation (sensitivity experiments minus reference experiment). The black dot indicates the Forsmark site, and the magenta line indicates the extent of the reconstructed Late Saalian ice sheet from Peyaud (2006). Lower panel: Map of the different regions considered in GRISLI in experiments D1 (e), D4 (f), D5 (g) and D6 (h) at the end of the simulation: Land not covered by ice sheets (blue), ocean (light blue), grounded ice sheet area where the SIA applies (beige), fast-flowing ice sheet area where the SSA applies (orange) and ice shelves where the SSA applies (red). The green line indicates the ice shelf area of the reference experiment REF\_Topo2.

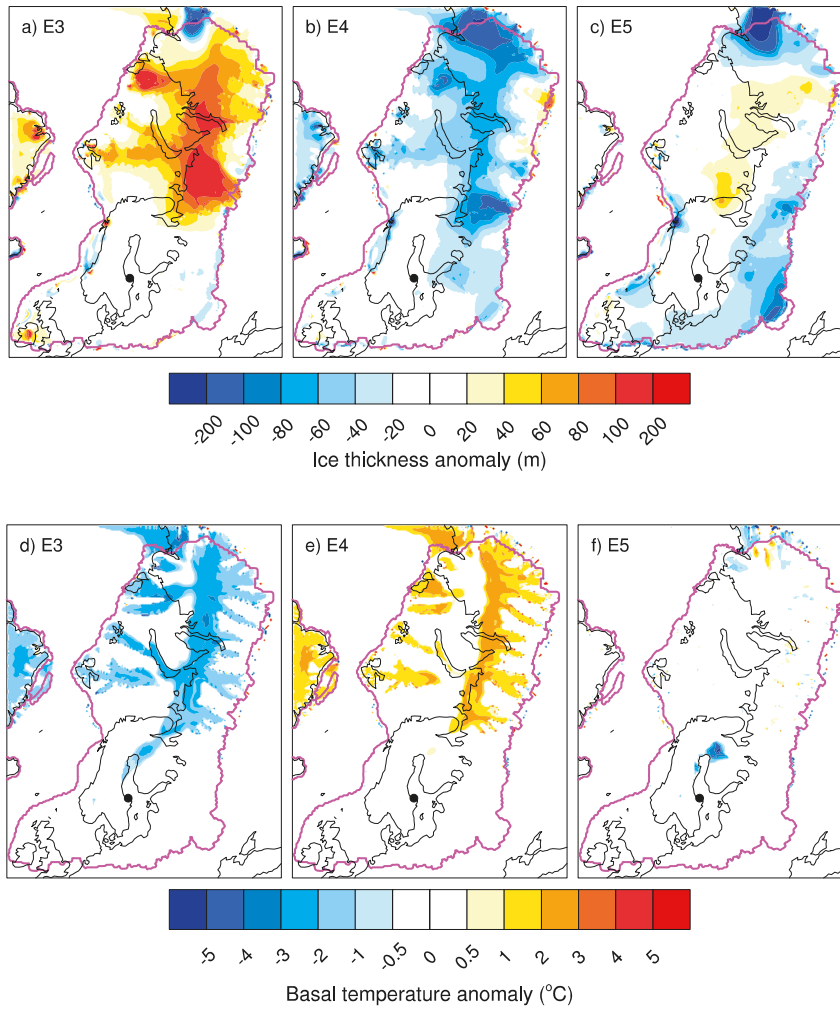


**Figure A3-7.** Impact of GHF: Difference in ice thickness (top) and basal temperature relative to the pressure melting point  $T_b$  (bottom) between the reference experiment REF\_Topo2 and experiments E3 (a, d), E4 (b, e) and E5 (c, f) at the end of the simulation (sensitivity experiments minus reference experiment). Note that  $T_b$  is only computed for negative temperatures.

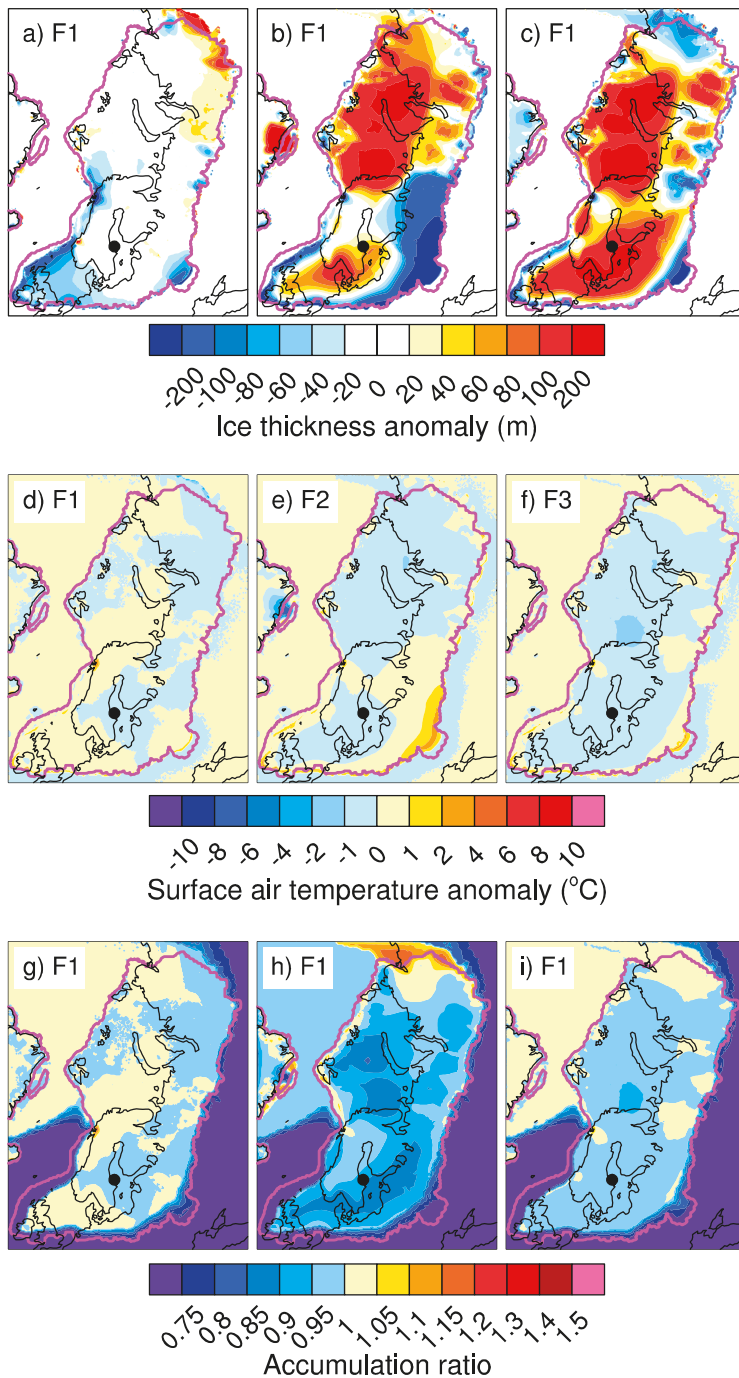


**Figure A3-8.** Impact of multi-parameter combinations: Difference in ice thickness (a, b, c), annual mean temperature (d, e, f) and accumulation (g, h, i) between experiments F1 (left panel), F2 (middle panel) and F3 (right panel) and the reference experiment REF\_Topo2 at the end of the simulation (sensitivity experiments minus (or divided by) reference experiment).

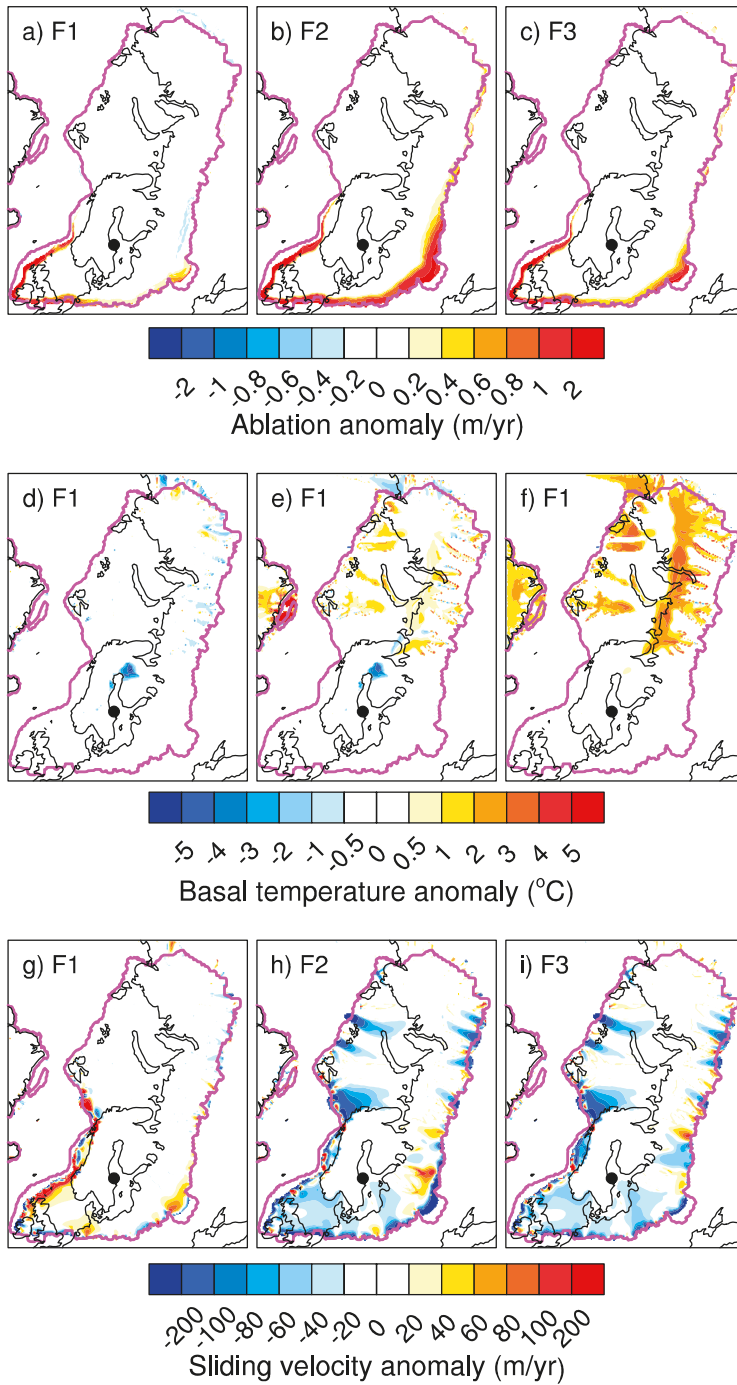


**Figure A3-9.** Impact of multi-parameter combinations: Difference in ablation (a, b, c), basal temperature relative to the pressure melting point (d, e, f) and sliding velocity (g, h, i) between experiments F1 (left panel), F2 (middle panel) and F3 (right panel) and the reference experiment REF\_Topo2 at the end of the simulation (sensitivity experiments minus (divided by) reference experiment).

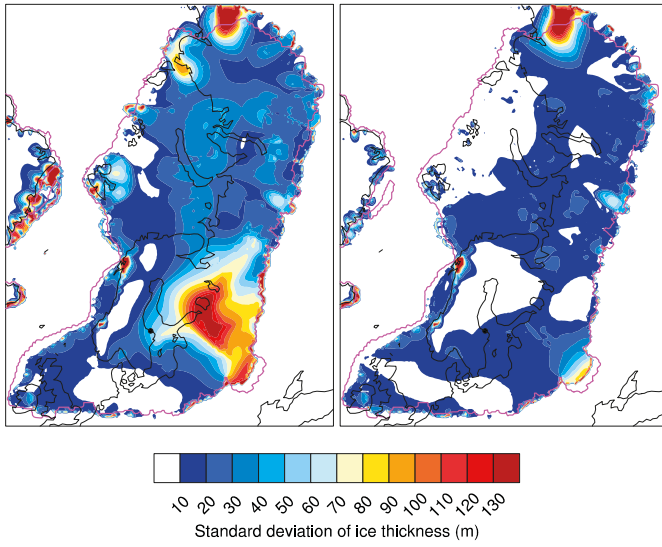


**Figure A3-10.** Standard deviation of ice thickness (m) of the reference experiments REF\_Topo1 (left) and REF\_Topo2 (right) calculated over the last 50 kyrs of the simulations.